Advances in the CVD growth of Graphene for electronics applications

by

Mario Hofmann

Dipl. Ing. Technische Physik, Technische Universität Ilmenau (2006)

Submitted to the Department of Electrical Engineering and Computer Science

in partial fulfillment of the requirements for the degree of

Doctor of Philosophy

at the Massachusetts Institute of Technology

February 2012

Author.....

Department of Electrical Engineering and Computer Science,

October 23, 2011

Certified by.....

Jing Kong

Professor of Electrical Engineering and Computer Science

Thesis Supervisor

Certified by.....

Mildred S. Dresselhaus

Institute Professor of Electrical Engineering and Physics

Thesis Supervisor

Certified by.....

Michael S. Strano

Professor of Chemical Engineering

Thesis Supervisor

Accepted by.....

Leslie A. Kolodziejski

Chairman, Department Committee on Graduate Theses

Advances in the CVD growth of Graphene for electronics applications

by

Mario Hofmann

Submitted to the Department of Electrical Engineering and Computer Science

in partial fulfillment of the requirements for the degree of

Doctor of Philosophy

ABSTRACT

Graphene, a monoatomic sheet of graphite, has recently received significant attention because of its potential impact in a wide variety of research areas.
This thesis presents progress on improving the quality of graphene for electronics applications. An analysis tool was developed that provides a fast and scalable way to reveal the defectiveness of CVD grown graphene. This approach relies on a graphene passivated etching process that was found to be sensitive to structural defects in the graphene film. A strong correlation between the density of structural defects and the electron mobility emphasizes their importance for high quality graphene devices. The dimensions of graphene defects were found to be nanometer-sized and it was demonstrated that the defects exhibit novel fluid dynamical properties.
The graphene synthesis process was investigated using the described analysis tool and the kinetics of graphene formation was revealed. The influence of promoters on the growth process was described and analyzed.
The new insight into the growth process was applied to a novel approach to directly synthesize graphene patterns by catalyst passivation. Several advantages of this method over existing fabrication schemes were described and a number of applications based on these improvements were shown.

Acknowledgements

I want to thank my advisors, Professor Mildred S. Dresselhaus and Professor Jing Kong, for offering me the opportunity to do research in their groups, for their support and for being role models in many more fields than science.

I am very grateful for the chance to interact with many amazing people during my stay in MIT and Boston:

- Lab mates, who taught me not only skills but excitement for research.
- Friends, who made Boston less gray and Wednesdays more exciting.
- Collaborators, whose effort improved my work and understanding.
- Supporters, who helped navigate the challenges of student life.
- Visitors, who shared their culture and broadened my view
- Students, who taught me while I trained them.
- Hosts, who opened new worlds to me.

Meiner Familie sei gedankt für ihre Unterstützung.

Finally, I want to thank you for your interest in this work.

Table of Contents

List of Figures

1. Introduction

1.1 History and future of graphene

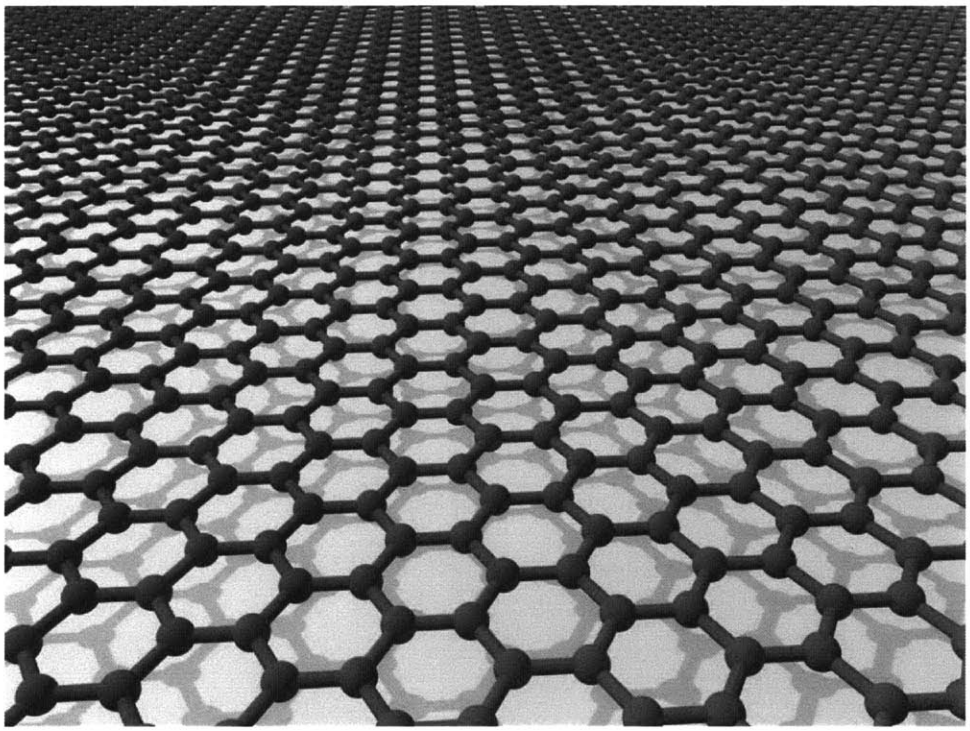

Figure 1 Depiction of graphene

Graphene has recently captured the attention of the public and the imagination of researchers. The compelling story of its discovery is repeated in scientific journals and newspapers alike: Graphene, a truly two dimensional material was thought to be thermodynamically unstable until its fortuitous discovery by Geim and Novoselov in 2004[1].

However, already its name points to the more complex history of graphene: The ending "–ene" has been used by chemists to indicate aromatic hydrocarbons that form fused shapes of benzene-like rings. Similar to "Naphtalene", "Graphene" is composed of the descriptor for its host material –graphite- and the "-ene" to indicate its chemical structure.

Several conclusions can be drawn from graphene's etymology:

- Like graphite it consists of a planar structure of sp^2-hybridized bonds in a honeycomb lattice.
- It represents an infinite size polycyclic hydrocarbon and consists of only one layer.
- Its origin can be traced back to chemists.

Indeed, suspensions of isolated, chemically functionalized graphene have been produced for ~170 years[2-4]. Modified versions of the synthesis method developed by those early chemists are still the basis of current production schemes. Bochm et al. succeeded in isolation of a graphene sheet and estimated its thickness to be monoatomic[5].

The timeline in Figure 2 raises the question why so much time passed between the initial discovery and the onset of general interest and why the many independent discoveries of graphene did not bring about a raised interest.

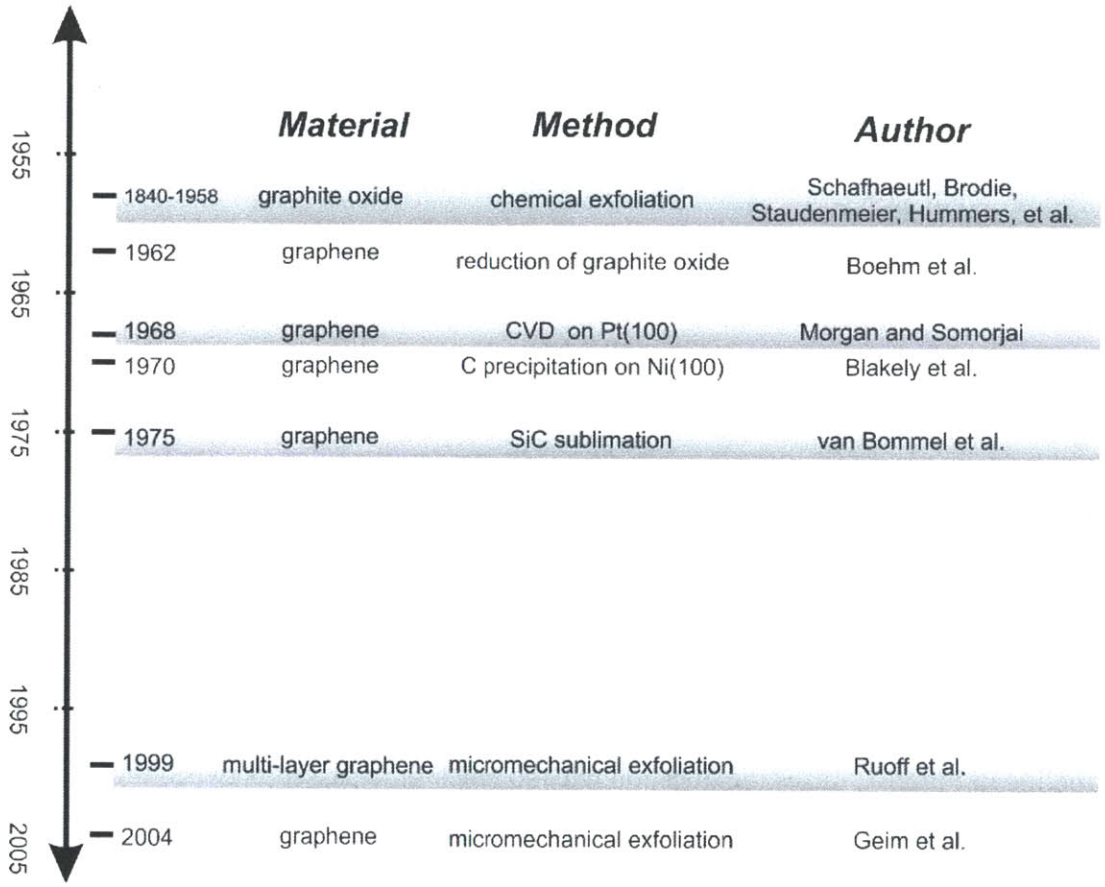

Figure 2 Timeline of discoveries made in relation to graphene [1-9]

It can be hypothesized that intermediate steps were required to signify its importance in order to dedicate more effort to graphene research. Two such steps occurred in the long period between 1975 and 1999 when graphene research was somewhat dormant.

The discovery of fullerenes, large carbon molecules[10], was made possible by breakthroughs in analysis techniques, such as STM and AFM[11], ushered in the era of nanoscience: It was found that tuning the size of materials could change their properties significantly and molecular manufacturing processes were envisioned that could design a functional material from the bottom up[12]. It turned out, however, that the goals were very ambitious and fundamental problems could not be overcome. For example, contacting a

single molecule through wires has proven challenging. Despite the failure to deliver on many of the promises of molecular electronics, researchers gained insight into the relation of structure and properties and the promise of sp^2 carbon.

Sumio Iijima's (re)discovery of carbon nanotubes [13] –cylindrical, graphitic structures- was the second necessary step as it provided a viable commercial vision for nanomaterials. Due to quantum confinement effects, carbon nanotubes could behave like metals or semi-conductors which invited the vision of all carbon electronics: The same material could be used to produce transistors and interconnecting wires on a very small scale and revolutionize microelectronics. As shown in Figure 3 the amount of funding by the National science foundation was significantly higher for research on carbon nanotubes than for fullerenes which indicates its assumed importance.

The selectiveness to synthesize nanotubes with a specified geometry is still an open issue. Furthermore, producing nanotubes in sufficient density, length and alignment remains an elusive goal and hinders its commercialization.

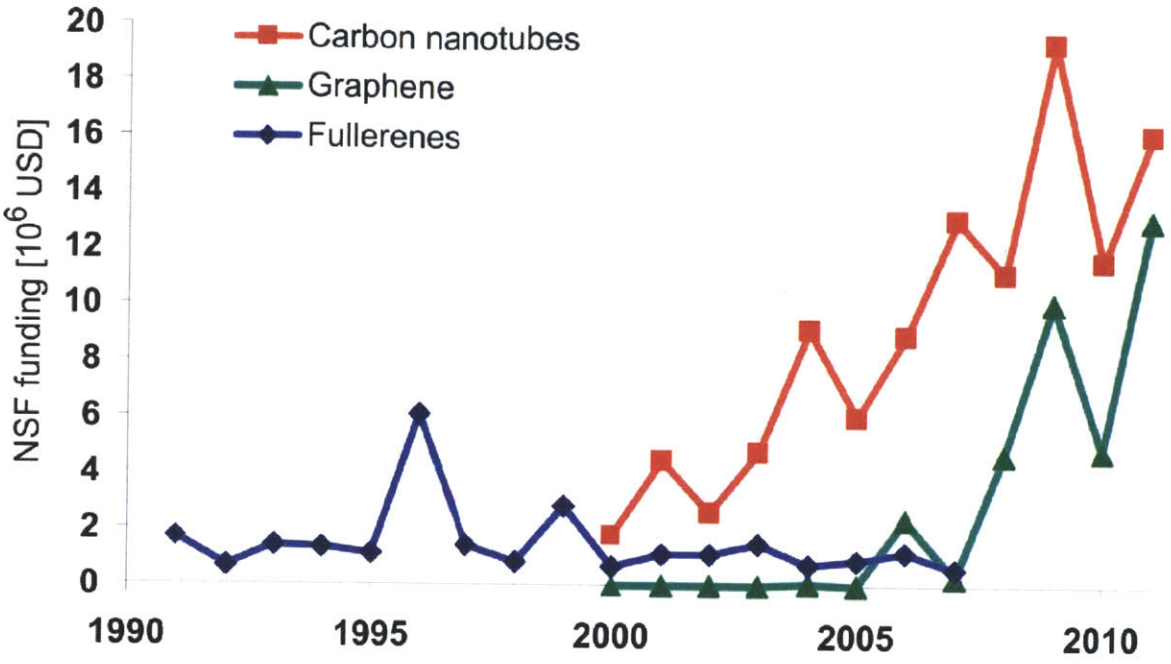

Figure 3 NSF funding for carbon materials vs. time

There was hope by researchers that graphene could overcome some of these problems since it was inherently easier to use than nanotubes. Because of its planar structure it would conform to a target substrate and could then be used like a regular wafer. Thus, the (re)discovery of graphene in 2004 came at the best time:

A lot of knowledge had been gained by the community by studying nanotubes in both analysis and handling.

Interesting properties, i.e. an unusual fractional quantum hall effect were theoretically predicted for graphene.

More detailed research of carbon nanotube properties was obstructed by the inability to fabricate high quality samples.

The optimism to make graphene into a commercially significant nanomaterial can be inferred from Figure 3, where the annual amount of NSF funding for the different carbon forms is plotted over time. It can be seen that funding of fullerene research is far eclipsed by the amounts invested into carbon nanotube and graphene research. Funding of graphene research has quickly increased to amounts similar to nanotube research.

Based on the lessons learned from the research of nanotubes, several related problems have to be solved for graphene to become a commercial success.

- Large scale synthesis of high quality graphene has to be achieved in a reproducible fashion to satisfy demands from industry.
- A reliable tool for the analysis of the graphene quality has to be found and made accessible to harmonize growth results from different groups. This would allow investigating reliability and optimization of growth results.
- An enabling application of graphene has to be found that cannot be realized by more mature materials and warrants the investment into graphene research.

This thesis will present work that tries to advance each of the three described fields of research.

1.2 Outline

Chapter 2 will introduce a novel analysis technique for the metrology of graphene. We demonstrate that the use of graphene passivated etch testing is a facile, scalable method to reveal and quantify imperfections in the graphene sheet. The sensitivity of the analysis technique to intentionally induced latticed defects compares favorably to the sensitivity of Raman spectroscopy. A strong correlation between the measured graphene defectiveness and the maximum carrier mobility emphasizes the importance of the technique for growth optimization. Due to its simplicity and widespread availability, we anticipate that this method will find wide application in the characterization of graphene and other 2D materials.

In chapter 3 the observed structural defects in chemical vapor deposition grown graphene are investigated. The location of openings in the graphene film are revealed by the graphene passivated etch test. Through size selective passivation of the openings by atomic layer deposition their diameter could be determined. An extremely fast mass transport through these nanometer-sized holes is observed with permeation speeds in the order of meters per second. Defects are found to be caused by nanoparticles that either decorate graphene domain boundaries or initiate graphene growth. Pretreatment of the Cu substrate is shown to reduce the particle density which results in higher quality graphene.

Graphene passivated etch testing is applied in chapter 4 to understanding the growth kinetics of graphene by chemical vapor deposition. The graphene growth rate is found to be determined by the dehydrogenation of methane. As the graphene coverage on the copper substrate increases this decomposition process is hindered which results in a

decrease in growth rate over growth time. This catalyst deactivation process represents a fundamental limit for graphene growth by surface reactions. The use of Nickel and Molybdenum promoters is shown to increase the carbon radical concentration and improve growth rate and graphene surface coverage. This study opens new routes for the control of graphene growth for future applications.

The application of the previous findings leads to a novel way of patterning graphene described in chapter 5. By selective passivation of the catalyst, graphene growth could be restricted to certain areas. High resolution and high quality of the grown graphene are achieved by using an aluminum oxide passivation layer. Several approaches for depositing the patterned passivation layer are demonstrated that could enable a variety of graphene based applications. Finally, the deposition of prepatterned graphene onto non-planar substrates is shown and the ability to generate high resolution graphene patterns on complex surfaces opens up novel application areas for electronic devices.

Conclusions and an outlook are presented in chapter 6.

1.3 Fundamentals

The following part is intended to introduce several fundamental tools of graphene research that will be necessary for the understanding of the following chapters.

. A short summary of the synthesis methods are presented with special emphasis on Chemical vapor deposition (CVD). Then, the process for transferring graphene will be explained. Finally, several analysis techniques that are used throughout this thesis are described.

1.3.1 Synthesis of graphene

Chemical exfoliation of graphite has been a viable technique to produce graphene for nearly 170 years. This approach is currently receiving significant commercial attention since it is expected to produce large graphene quantities at low prices. An oxidation step during production results in covalent bonds on the graphene surface. These defects can increase the solubility of the material and it has its own set of interesting applications. This thesis, however, will focus on the synthesis of graphene suitable for electronics applications and thus will not detail this synthesis method.

The transformation of SiC was a first approach to obtain graphene thin films, developed by van Bommel et al.[8]. The graphene sheets formed by sublimation of Si-atoms and the accumulation of a carbon rich face. The compatibility of the process with standard processes in the semiconductor industry explain the commercial interest in this synthesis method. The high cost of the substrate, however, prevented broad use of the method.

The contribution by Andrei Geim and Konstantin Novoselov can be described as the pinnacle of efforts to produce graphene from graphite by mechanical means: The research group by Prof. Ruoff[9] had previously attempted to exfoliate one layer of graphene by sheering it off from a stack of graphite. The lacking control over the thickness of the produced layers raised the question of the general feasibility of this approach. The important contribution of Andrei Geim and Konstantin Novoselov was to provide a method to easily identify the thickness of the produced graphene. The identification technique is based on an interference effect of graphene on a multilayered substrate. A 300nm Silicon dioxide layer could thus make mono-atomic differences in the thickness of graphene visible. With the increased speed of the analysis process less efficient ways to

exfoliate graphene could be tried. Consequently, an extremely simple procedure, involving a transparent adhesive and graphite flakes (see Figure 4 (a)) succeeded in producing graphene. The immense success of the method with the scientific community is not only based on the availability of materials and ease of use, but also on the high quality of the obtained samples. No post-treatment is necessary to observe quantum mechanical properties and to date no other graphene synthesis can compete with the transport properties of exfoliated graphene.

Figure 4 Required material to produce graphene

Chemical vapor deposition (CVD) is a well established procedure to produce carbon materials, such as diamond and carbon nanotubes. The synthesis of graphene through exposure of transition metals to carbon containing precursors has been established since 1968[6] but received little attention outside the surface physics community because of the

complexity of the necessary equipment and the limited interest in the material. The experiments on CVD were revisited when interest in graphene increased.

CVD systems for laboratory research usually consist of a clam-shell furnace that heats a fused silica tube which is connected to a gas inlet and an exhaust or pump (see Figure 5). Graphene is synthesized on a substrate that is positioned in the heated zone by decomposition of a carbon containing precursor, such as methane, ethanol or benzene. Other gasses, i.e. hydrogen, are added to control the decomposition reaction or affect the substrate morphology.

Several materials have been tested for their ability to catalyze graphene growth. Most of them are transition metals and parallels to the growth process of carbon nanotubes can be drawn. Similar to nanotubes, graphene can also be grown on dielectric substrates, i.e. sapphire, albeit higher temperatures are necessary[14].

This thesis will focus on the synthesis of graphene on Cu substrate following work by Li et al.[15] since the self limiting growth process observed on Cu results in a robust synthesis of single layer graphene.

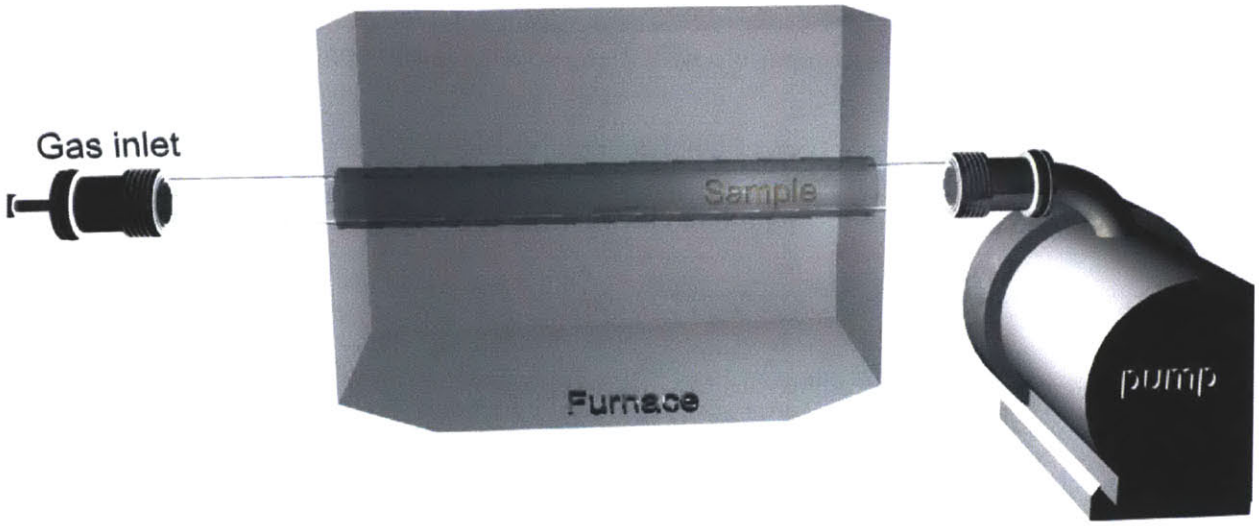

Figure 5 Schematic of the CVD setup used for graphene growth

Graphene was synthesized as previously reported[16] using copper as the catalyst material. Briefly, under low pressure (400mTorr) a piece of copper foil (Alfa 13382) was annealed in a gas flow of 10 standard cubic centimeters (sccm) hydrogen at 1000°C for 30 minutes before 20sccm methane gas was introduced to initiate the graphene growth. To control the graphene growth rate, 50sccm of hydrogen flow was used during the growth period. After the synthesis process was completed the material was cooled down under 5sccm hydrogen to prevent oxidation and to minimize hydrogenation reactions of the graphene.

1.3.2 Graphene Transfer

One issue of the described synthesis of graphene by CVD is the presence of the Cu growth substrate. Since it is metallically conducting, Cu will short out electronic devices fabricated on the grown graphene. Effort is being directed to circumventing this problem by directly growing on insulating substrates. The absence of catalytically active material,

however, means that higher energy barriers have to be overcome and the necessary growth temperature is incompatible with many substrates and applications.

Until the issue of energy efficient graphene synthesis on dielectric substrates can be overcome, a transfer step is required to move the graphene from the growth substrate to a target substrate[17].

The transfer process used here has the following steps:

- Immobilization of the Cu-foil on a PET substrate by taping of the edges
- Spin-coating of 9% Polymethylmethacrylate (PMMA)in Anisole solvent at 2500rpm on the graphene covered Cu substrate
- Hard baking of the sample at 120°C for 10 minutes
- Removal of the plastic backing
- Removal of Cu-foil by exposure to Transene CE100 copper etchant
- transfer of the floating PMMA/graphene membrane into water
- Positioning of the membrane onto a target substrate
- Removal of the PMMA supporting layer by annealing in Ar/H_2 forming gas.

1.3.3 Atomic layer deposition

Atomic layer deposition (ALD) is a process that can deposit high quality thin films. Due to the self-limiting nature of the deposition process, monolayer thickness resolution can be achieved.

The deposition process consists of the sequential exposure of a sample to two materials First, a precursor is introduced that physisorbs onto the surface. The subsequent exposure to a reactant changes the chemical makeup of the precursor thus forming a stable compound. The exposure cycle can than be repeated to add subsequent layers of material onto the grown ones.

In the presented work trimethylaluminum (TMA, $Al_2(CH_3)_6$) was used as the precursor and water as the reactant. In this system TMA reacts with surface hydroxyl groups under methane formation. This reaction proceeds until the surface hydroxyl groups are passivated and because TMA does not react with itself it is self limiting. In a second cycle water is introduced that reacts with the TMA to form Aluminum oxide with hydroxyl groups under methane production. These hydroxyl groups form the foundation for subsequent cycles[18].

To achieve deposition of monolayer films purging under inert gasses and elevated temperatures are used to remove excess precursor.

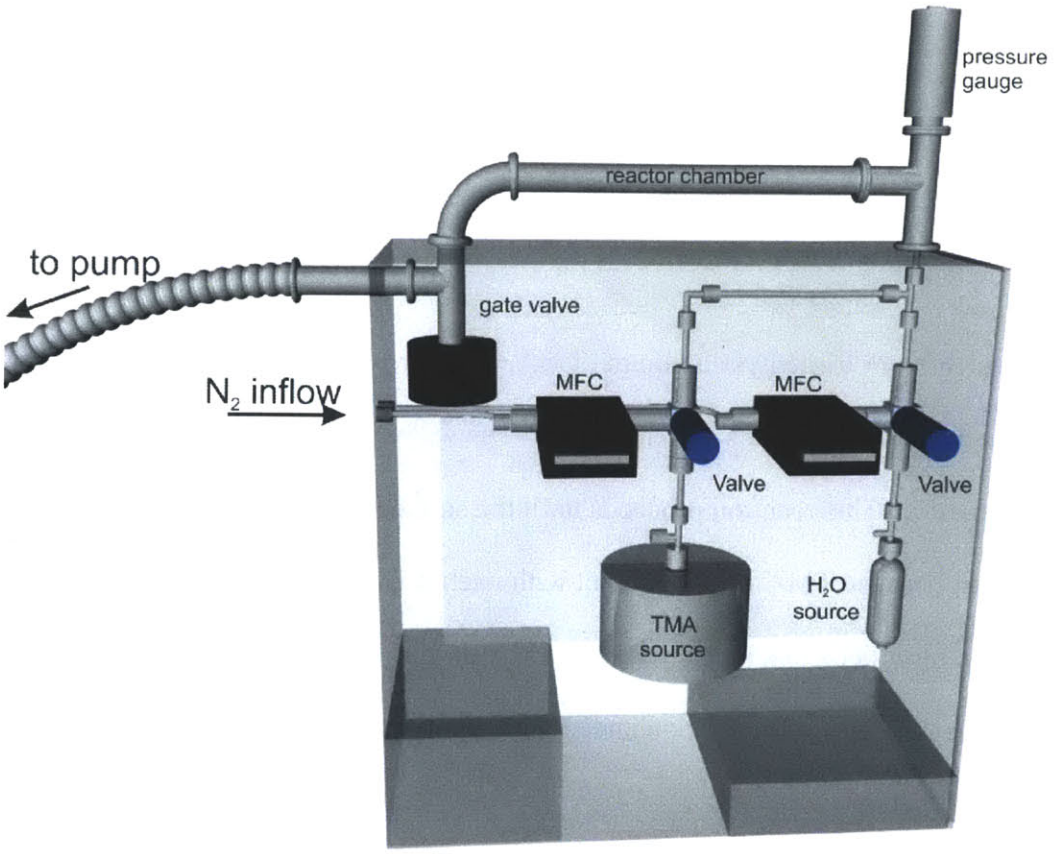

Figure 6 Schematic of homebuilt ALD system in the nmelab

A homebuilt ALD system is available in the nanomaterials and –electronics group of Prof. Kong (as shown in Figure 6). Both, precursor and reactant were dosed by Swagelok high speed ALD valves (6LVV-ALD3G333P-CV) in 15ms pulses. The system was held at 125°C at a base pressure of 900mTorr and purged for 45s with dry Nitrogen between cycles. The deposited film thickness was confirmed by AFM measurements on blank Si/SiO_2 samples. The deposited thickness per reaction cycle was calculated to be 0.14nm/cycle which is close to literature values [19].

1.3.4 Analysis techniques

As mentioned previously, the increased interest in graphene coincided with a breakthrough in its metrology. The following part reviews several tools that were used in this work to elucidate different aspects of graphene properties.

Optical microscopy

The ability to identify mono-atomic variations in thickness of graphene by optical microscopy can be considered one of the most important factors for the success of the mechanical exfoliation method described above.

Through simple optical observation the thickness of obtained graphene flakes could be inferred from their contrast on the sample as seen in Figure 7.

An experienced experimentalist could quickly analyze dozens of flakes within a matter of seconds which permitted locating one micron-sized graphene flake on a centimeter large substrate. The lacking identification ability had made previous attempts to producing graphene prohibitively slow and tedious.

Geim et al.[1] found that even single layer graphene –as well as other materials- could be distinguished by their contrast on a 300nm Silicon oxide layer grown on a Silicon wafer.

The underlying principle of contrast enhancement through multi-beam interference on a dielectric stack was a well known tool to measure the flatness of samples but the strong absorption of a monolayer of graphene results in a large contrast enhancement [20] and has to be considered a fortuitous coincidence.

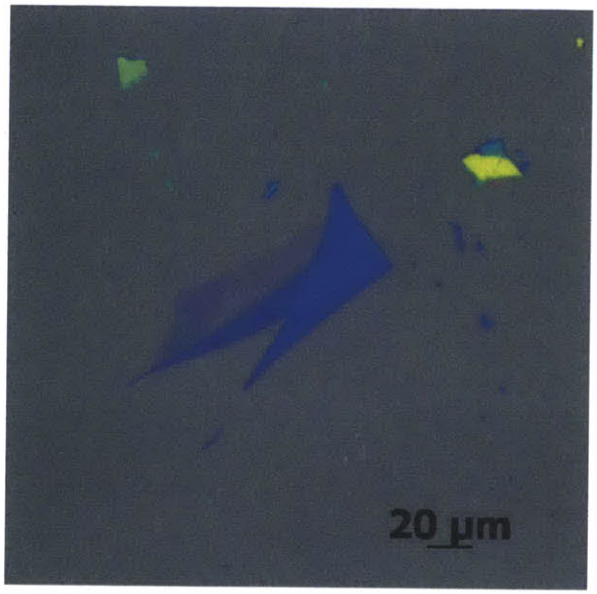

Figure 7 Optical micrograph of graphene and various thickness multilayer graphene

Atomic force microscopy (AFM)

The operating principle of scanning probe microscopes is based on the voltage induced extension of a piezoelectric material[11]. This allows the scanner head to be positioned by fractions of a nanometer. This unprecedented accuracy in positioning has to be combined with a sensitive feedback scheme. In an AFM a microscopic cantilever is interacting with the sample and its deflection is amplified by a reflected laser beam. The motion of the AFM head is then controlled to minimize the deflection. The necessary travel of the AFM head will thus follow the contour of the sample and return topography information of the sample. Figure 8 shows a resulting image and height differences can be related to variations in the number of occurring graphene layers.

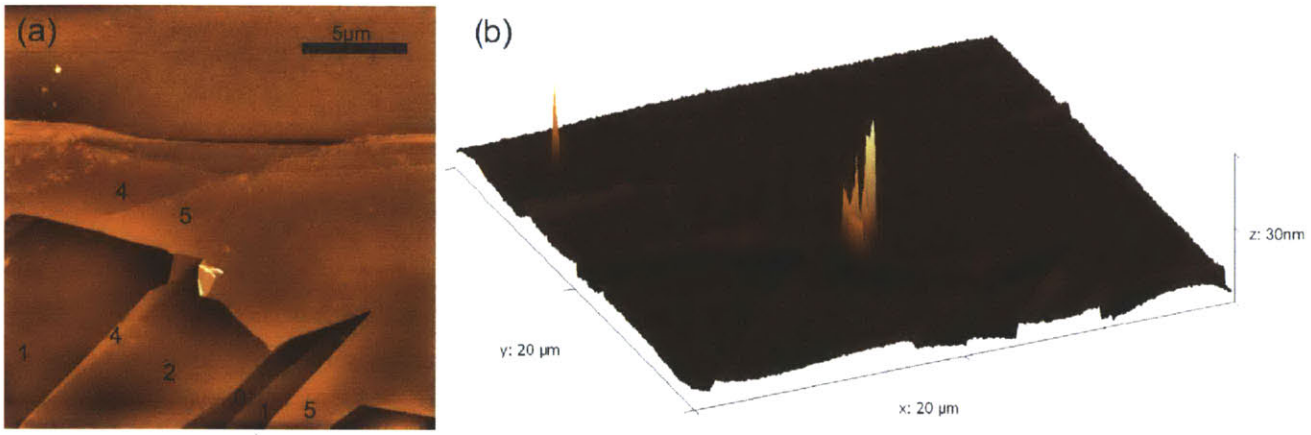

Figure 8 AFM images of graphene (a) false color representation with estimate of number of layers (b) 3D representation of same image

An estimation of the number of layers can be obtained when considering an interlayer spacing of ~0.33nm and a gap between substrate and graphene of ~0.7nm, due to the interaction with the substrate and adsorbed water[21]. Thus, mono-atomic differences in height can be reliably distinguished through the use of AFM.

Furthermore, changes in the morphology of a sample can be studied by AFM and in the following chapters the occurrence of etch pits is analyzed.

Raman Spectroscopy

Carbon research is one of the most fruitful areas for Raman spectroscopy. As seen in Figure 9, the relative importance of this field to all research on Raman spectroscopy is steadily increasing since the discovery of fullerenes[22].

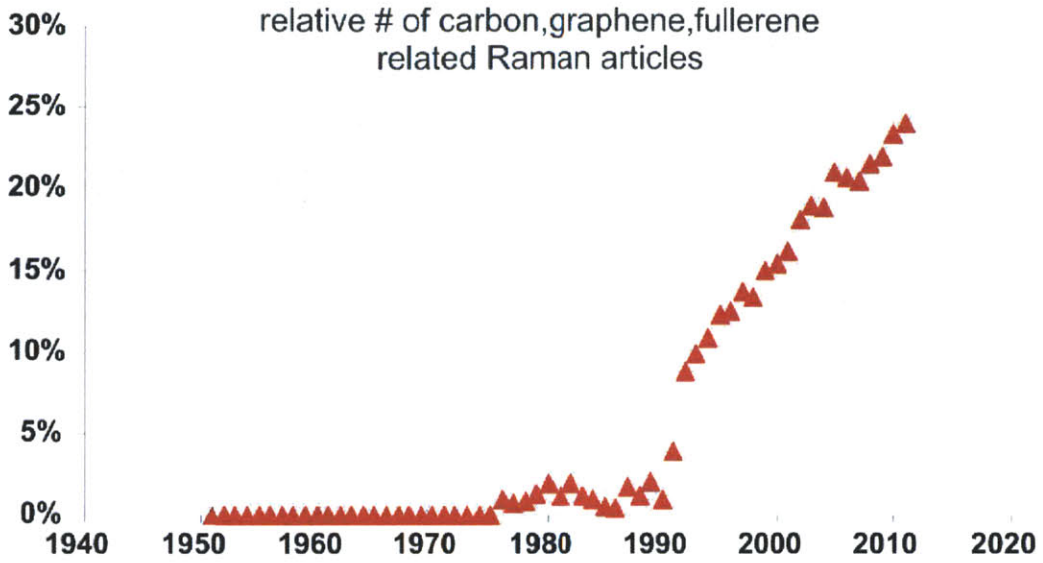

Figure 9 Publications for carbon related Raman spectroscopy normalized by total number of all Raman related publications

The reason for this behavior is the immense wealth of knowledge that can be gained by the Raman spectroscopic analysis of carbon systems. In Raman spectroscopy the inelastic scattering of light most commonly by creation or annihilation of a phonon is analyzed.

In a typical graphene spectrum (i.e. Figure 10) several characteristic Raman features can be observed[23]. Momentum conservation limits the number of possible phonons that can be excited through light because photons have a negligible momentum.

The G-band around 1600cm^{-1} is related to in-plane optical phonons with zero momentum and can be directly excited through optical phonons.

Other Raman modes require a higher order process to satisfy momentum conservation. The G'-band for example is related to a second order process involving the scattering with two optical K-point phonons. Usually such a second order process is much weaker than first order processes but the resonance of the scattered states with the graphene band structure enhances the intensity of this feature to be comparable or even higher to the G-

band peak. Since this enhancement effect is closely related to the band structure of graphene, a large G'-band intensity can be considered a fingerprint of graphene. Furthermore, the width of the G'-band is sensitively dependent on changes to the graphene band structure and the perturbation of adding a second interacting layer can thus be detected.

An important feature for the metrology of graphene samples is the D-band around 1350cm^{-1}. It involves the same optical K-point phonon as the G'-band but instead of requiring a second phonon to scatter back to the origin, an inelastic scattering process with a defect satisfies momentum conservation. Thus, the analysis of the D-band intensity has been widely used as a quantification of the defectiveness of a graphene sample.

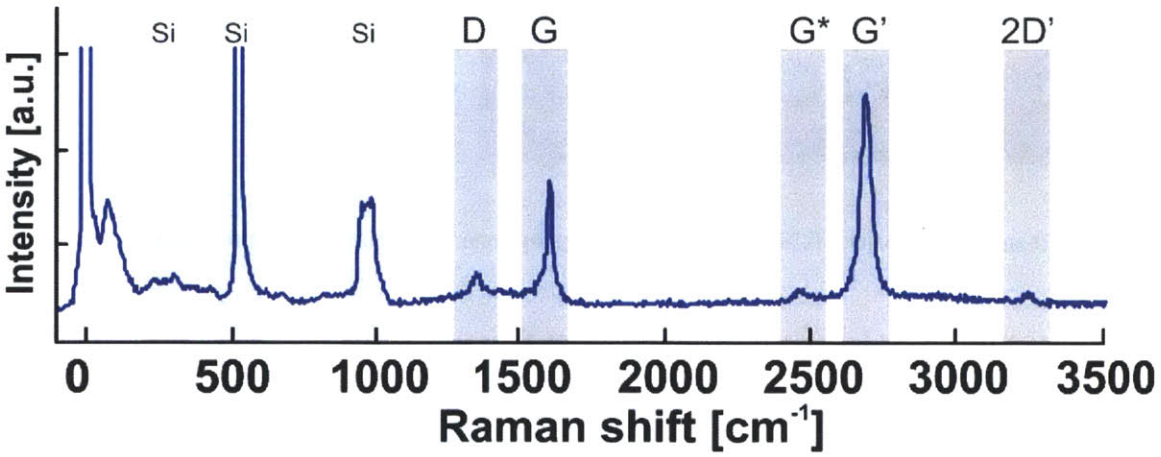

Figure 10 Representative Raman spectrum of Graphene and indication of common features

The evaluation of graphene samples solely based on the D/G ratio, however, could be misleading, since details of the phonon-defect scattering process are not well understood. The idea that the D/G ratio is only dependent on defect density would not hold true when comparing samples with different kinds of defects. For example defects terminating in

armchair edges have a small Raman scattering cross section compared to zigzag terminated defects. Furthermore, resonance effects between defects are expected to affect the collective D-band intensity [D band Raman intensity calculation in armchair edged graphene nanoribbons].

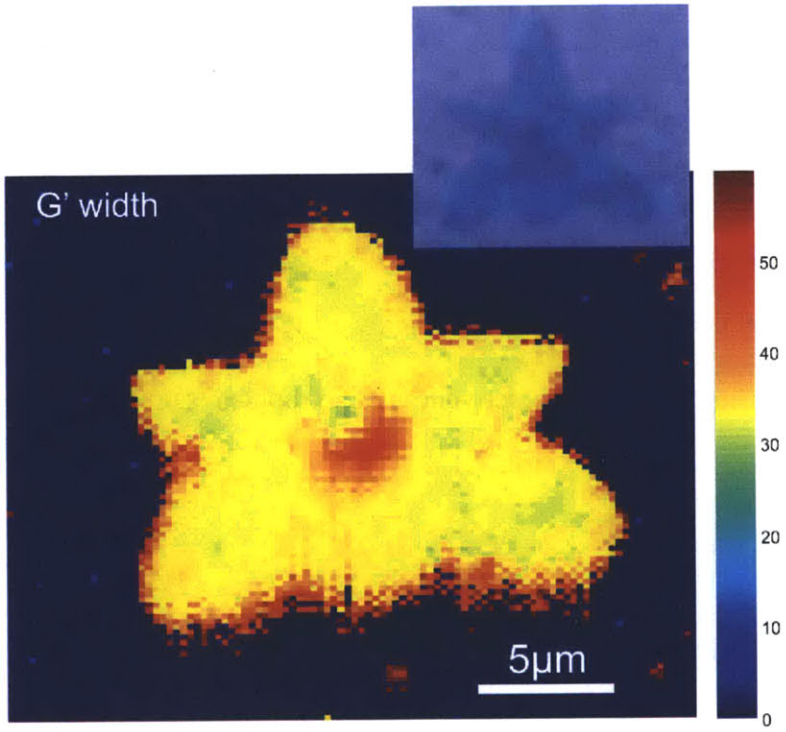

Figure 11 Raman map of the G'-band FWHM of a graphene flake, (inset) optical image of the same flake

A Raman map can be generated by taking Raman spectra as a function of spatial position. Thus, the variation of a parameter across a sample can be visualized. An example of these capabilities can be seen in Figure 11 where the full width at half maximum of the G'-band peak is analyzed across a graphene flake. It can be seen that this feature is relatively homogenous across the flake except in the center, where the width increases from ~32cm^{-1} to ~49cm^{-1}. This area correlates with a darker region in the optical image of the flake (see inset of Figure 11). The larger optical contrast suggests that the center region in

the observed flake consists of bi-layer graphene. The Raman map supports this hypothesis since it is known that interacting bi-layers exhibit a larger G'-band width[24].

2. A facile tool for the characterization of CVD grown graphene

2.1 Necessity for a new analysis tool

As mentioned in the previous chapter, one common challenge for obtaining high quality samples for many applications is minimizing the density of defect sites in the obtained graphene films. We here focus on the analysis of structural defects in the continuous graphene film because it includes a wide variety of defects, such as lattice defects, incompletely grown graphene, etc. Furthermore these structural defects can degrade the performance of graphene in many respects. For example, Bunch et al.[25] found that the presence of a $1\,nm^2$ opening in a graphene membrane would cause gas effusion that would drain a graphene sealed microchamber of $1\,\mu m^3$ within one second. Chen et al.[26] determined that lattice defects, such as carbon atom vacancies, would deteriorate the electrical transport in a graphene device significantly. Ruiz-Vargaz et al.[27] reported a decrease in the mechanical strength of graphene caused by defects at the grain boundaries.

Considerable effort is currently being invested to control the density of structural defects by optimization of the CVD synthesis process since it is widely believed that this process step is introducing structural defects. One challenge is to confirm this assumption since other process steps are necessary to prepare the graphene for analysis: To analyze graphene by high resolution transmission electron microscopy, for example, the material has to be transferred to grids or membranes[28]. The quality of Raman spectroscopy suffers under a low achievable signal-to-noise ratio when done on metallic substrates.

Thus, a transfer step is normally necessary before the analysis can proceed. This transfer step itself can introduce defects through tearing, exposure to acids, residues, etc[29]. Thus, a high resolution analysis technique is needed that does not rely on a transfer step.

Another issue is the comparison of results obtained by different synthesis protocols and by different groups. The restricted availability of current metrology instruments that can analyze openings in the grown graphene sheet and the complexity of the necessary measurements limit their practical applicability. Thus, there is a need for a broadly available and scalable metrology tool.

A final requirement for a broadly appealing graphene analysis technique would be speed and ease of use of the process. Currently, scanning probe techniques as well as scanning spectroscopy techniques are relatively slow and can only give feedback about the quality of small graphene regions.

2.2 Concept of graphene passivated etching

We will here introduce an analysis technique that can overcome these issues and has the potential to become a useful graphene metrology tool. The method uses materials and tools that are widely available and is compatible with a multitude of imaging techniques. It can furthermore be applied directly to as-grown samples without the need for a transfer step. The sensitivity of the described technique can be tuned finely to visualize openings in the graphene film originating from incomplete growth as well as lattice defects by graphene passivated copper etching. A correlation was found between structural defects and the maximum mobility of graphene devices which emphasizes the usefulness of the described analysis technique.

The analysis technique relies on the analysis of the etching behavior of graphene passivated copper substrate when exposed to copper etchant.

Graphene was synthesized on copper foil as detailed earlier and a small piece of the sample was then affixed to a glass slide with double sided tape to simplify handling. A drop of commercial copper etchant (Transene APS-100) was deposited onto the graphene sample with a pipette (This ammonium persulfate-based etchant was chosen over $FeCl_3$ based etchants because this etchant did not leave residues on the sample). After waiting for 10 seconds, the drop of etchant was removed by thorough rinsing with deionized water and subsequent blow-drying with compressed nitrogen.

The basic concept of the proposed analysis tool is described in Figure 12(a): Regions on the copper substrate covered by graphene are protected from being corroded whereas regions without a graphene layer are readily attacked by the copper etchant.

2.3 Experimental results

This concept is validated by the comparison of the left and the right area of Figure 12(b). In the top area of the image a graphene layer deposited by chemical vapor deposition protected the Cu substrate while in the lower area the graphene was partially peeled off using a Scotch tape. Both sides were exposed to copper etchant following the described procedure but a significant difference in morphology can be seen. Simple visual inspection reveals a larger roughness of the copper substrate on the lower side. This indicates that graphene effectively passivated the upper area as suggested by Chen et al.[30]

This ability to easily confirm the presence of graphene after growth already represents a significant advantage over existing analysis techniques. With commonly used analysis tools such as optical microscopy or Atomic Force Microscopy (AFM) answering this fundamental question requires the transfer of the graphene from the growth substrate to a different target substrate – a process that is both time consuming and might compromise

the results since the graphene film can get damaged or contaminated in the transfer process. The process is both easy and time effective and takes between 1-5minutes.

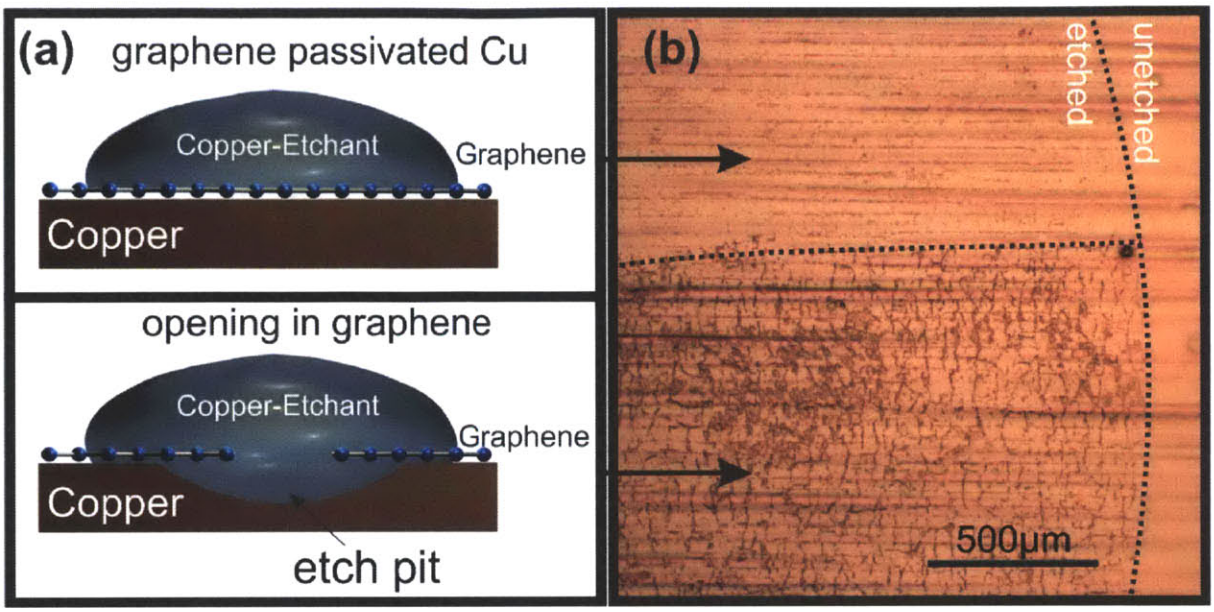

Figure 12 Schematic of the graphene passivated etching process: In the case of complete graphene coverage (upper panel) no etching occurs but openings in the graphene film result in etch pits in the copper substrate (lower panel). (b) Optical micrograph of copper surface after 10s etching with complete (top) and partial (bottom) graphene passivation layer

The power of the described analysis technique lies in the ability to visualize structural defects in the graphene film through analysis of the etch patterns in the Cu substrate. Since the graphene is expected to protect the Cu substrate, no etching should occur on the graphene passivated Cu substrate.

There could be different reasons for the observed etching. For example the graphene could be destroyed by the Cu etchant and these openings could be permeated to generate etch pits. This hypothesis can be discounted because the ammonium persulfate based copper etchant is only a mild oxidant and is not expected to attack the carbon-carbon bonds in the graphene sheet. In single walled carbon nanotubes this etchant was shown to

introduce defects in the nanotube wall only upon several hours of exposure and agitation[31] and the observed SWNT cutting proceeded by enlarging existing defects[32]. The resistance of graphene to ammonium persulfate was also confirmed by etch tests on graphite where no etching was observed even after prolonged exposure (30 hours). Thus, graphene is expected to protect the underlying copper from oxidizers (as demonstrated by Chen et al.[30]). This is the reason for routinely destroying the graphene on the back of the catalyst foil before transfer to ensure fast etching of the copper substrate.[16]

Another reason could be the permeation of copper etchant through existing structural defects in the graphene film (as indicated in Figure 12(b)). These structural defects could originate from several different scenarios:

- Incomplete graphene growth results in only partial coverage of the substrate starting from nucleation points that form flakes as observed by Li et al.(Li, Magnuson et al. 2010)
- Particles on the catalyst surface represent obstacles that cannot be covered by graphene and when removed leave exposed copper substrate.
- Lattice defects present openings in the continuous graphene film that could be permeated by the etchant.

We subsequently demonstrate the ability to identify those different structural defects by the described analysis technique and study its sensitivity.

2.4 Quantification of graphene defectiveness

Figure 13 shows a comparison of the morphology of different samples after exposure to copper etchant. Figure 13(a,d) represents a copper substrate that had only been annealed

and no graphene growth was initiated. Thus, the copper substrate was not passivated with graphene and uniform etching occurred across the sample, apart from some impurities. The morphology in Figure 13(b,e) was obtained after 10 minute exposure to a low partial pressure of methane (3sccm). As reported by Li et al.[33] these conditions do not result in a continuous film of graphene. Instead, only individual flakes of graphene grow. The effect of those flakes protecting certain areas of copper substrate from the etchant can be distinguished both in the optical micrographs (Figure 13(b)) and in the atomic force microscope images (Figure 13(e)). Finally, the completely grown graphene film will protect the copper as seen in Figure 13(c,f). The holes represent defects in this continuous graphene film that are permeated by copper etchant. These defects are caused by impurities in the copper foil and lattice defects, as described below.

To quantify these observations we define a parameter θ that is proportional to the surface coverage of graphene. The parameter is determined as the ratio of unetched copper substrate to total area. The parameter is obtained by analyzing the projected area of the etch pits identified in AFM images and normalizing the projected area to the overall AFM image size. As expected, θ of unprotected copper substrate is low (1%), increases to 30% for incomplete graphene growth and reaches 95% for completely grown graphene. It has to be noted that θ corresponds to the graphene coverage only for vanishing etching time since under-etching of the graphene can occur. Thus, care has to be taken in the comparison of θ obtained by other methods (i.e. through the analysis of scanning electron micrographs) with the described technique since the graphene coverage is underestimated by this technique. The under-etching, however, presents the opportunity of varying the sensitivity of the analysis technique. For low exposures to etchant –either through short

etching times or low etchant concentrations- large openings, caused for example by incomplete growth, can be discerned. High etchant exposures, on the other hand, will result in the amplification of small openings such as lattice defects. Thus, at longer etching times defects can be made visible that are normally not discernible in SEM or even AFM images. Through this behavior, the analysis of atomic imperfections through broadly available imaging tools, such as optical microscopes, can be envisioned.

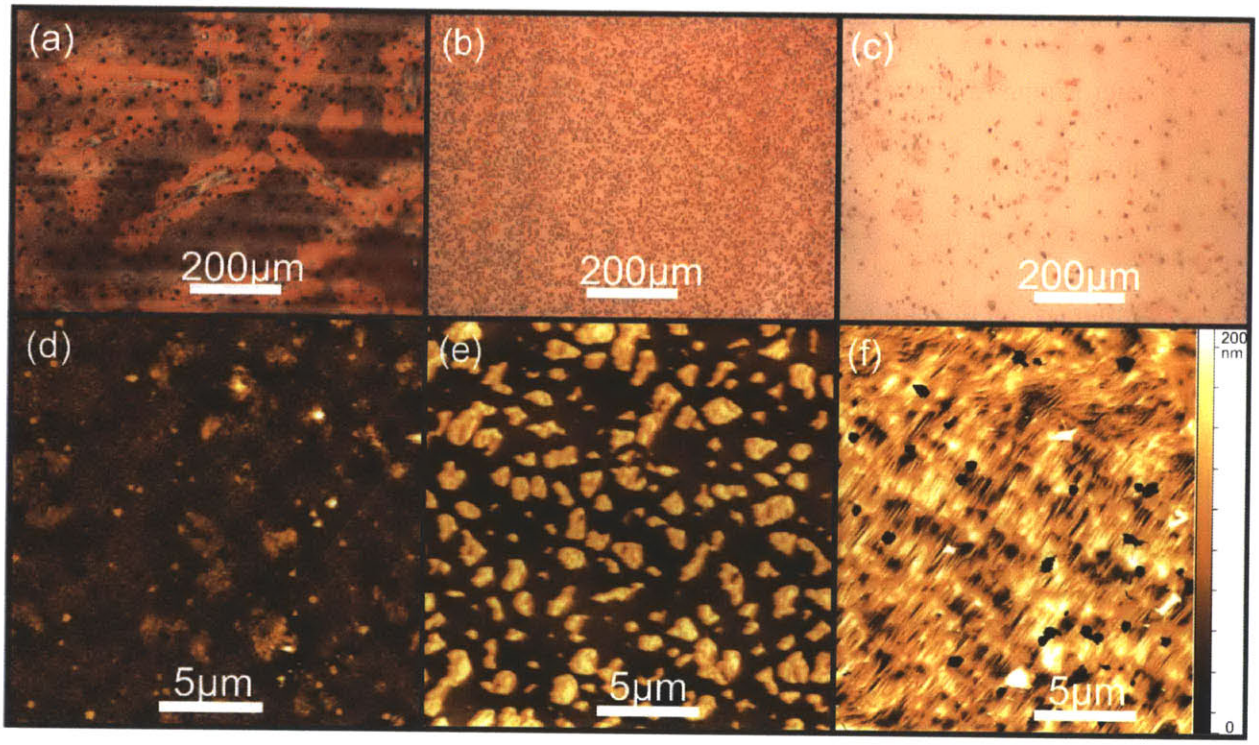

Figure 13 Morphology after 10s etching for 3 different growth conditions by optical microscope (a-c) and AFM(d-f) images: (a,d) no graphene growth (θ=1%) (b,e) incomplete graphene film (θ=30%), (c,f) complete graphene film with a low density of openings (θ=95%)

2.5 Information about the substrate

The etching patterns can furthermore reveal the crystallographic orientation of the copper substrate. Figure 14 shows a graphene passivated copper sample with a large density of etch pits of triangular shape. This observation is illustrated by investigation of a single

etch pit in Figure 14(c). The anisotropic etching behavior was already observed in 1962 [34] and subsequently attributed to the preferential etching of the Cu (100) crystallographic planes [35].

The parallel alignment of the etch pit boundaries over large areas is supported by the occurrence of distinct symmetric lines in the spatial Fourier transform (Figure 14(d)) of a 50x50um area. This 2D FFT pattern indicates the high number of similar spatial frequencies occurring corresponding to parallel edges with the same slope. The observed large scale crystallographic orientation indicates the large single crystalline domains in the copper foil. The SEM image in Figure 14(e) shows that transitions between single crystal domains can be identified by the difference in orientation of the etch pits.

The occurrence of faceted etch pits was reported to be sensitively dependent on the etchant or the copper quality[34,36]. We have only observed faceting during the initial studies and hypothesize that the batch-to-batch variation of the purchased Cu foil or the aging of the etchant could be responsible for the subsequent random shapes of the etch pits.

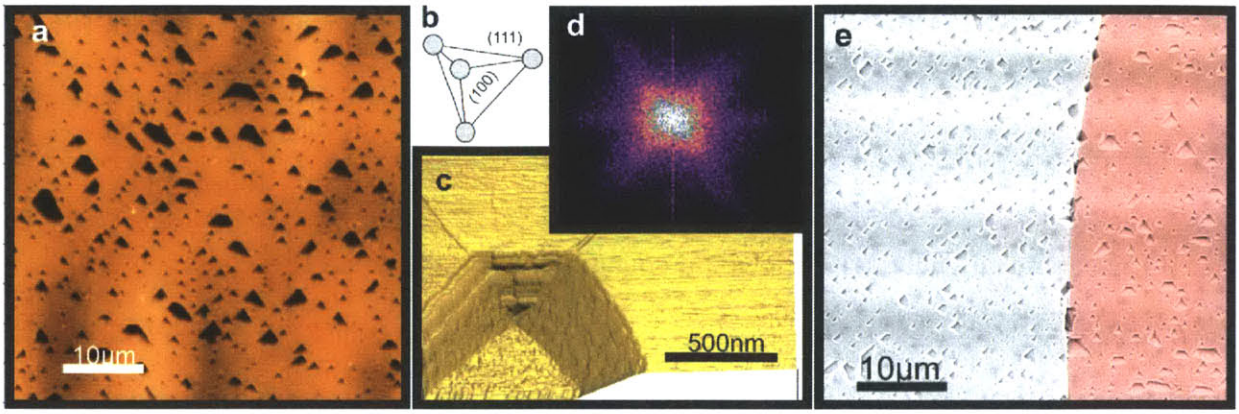

Figure 14 (a) AFM image of aligned etch pits, (b) orientation of crystallographic planes (c) 3D representation of AFM close-up of one etch pit, (d) 2D Fourier transform of (a), (e) SEM image of two areas with different shaped etch pits

2.6 Comparison to Raman spectroscopy

To test the sensitivity of the new analysis tool, samples with a variety of defect densities are necessary. This variation in defects was achieved by intentionally introducing more defects in an as-grown sample and analyzing the variation in the etch pit morphology. Ozone generated by UV-illumination has been shown to create lattice defects[37] by oxidizing carbon atoms. The changes in graphene quality after exposure of graphene to UV-ozone in a UVO-cleaner (Jelight Company) were measured by analyzing θ for various UV-ozone exposure times t_{UV} after 10s of copper etching and by Raman spectroscopy of a similar graphene sample transferred onto silicon substrates with 300nm SiO_2.

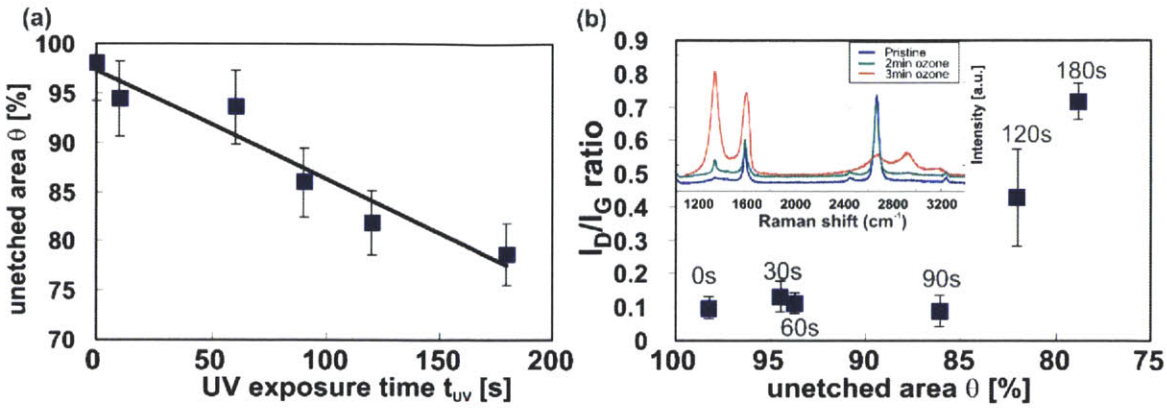

Figure 15 (a) Unetched area θ as a function of UV-ozone exposure, (b) comparison of Raman I_D/I_G ratio and θ, (inset) representative Raman spectra at various exposures

Figure 15(a) shows that θ decreases for longer exposures to ozone. This agrees with the prediction that more lattice defects are generated that allow permeation of copper etchant and thus a higher density of etch pits are formed. A more detailed analysis of the plot of with exposure time t_{UV} reveals information about the defect density introduced by ozone. At low ozone exposures the lattice defects are individually and randomly distributed across the samples and thus each defect results in one hole in the graphene film. In the high defect density regime, on the other hand, the addition of another defect would only enlarge existing holes. Because of the described under-etching, several individual holes will have a larger effect on the etched area than one large hole. Thus the transition between the low and high defect density region would result in a decrease of the slope of $\theta(t_{UV})$. From the linear decrease in $\theta(t_{UV})$ it is inferred that all measurements are performed in the low defect density regime.

The inset of Figure 15(b) shows representative Raman spectra of the same graphene sample, transferred to an Si/SiO_2 wafer, for different t_{UV} . A strong variation of the D-band region around 1300cm^{-1} can be observed. This feature originates from a K-point

phonon and since elastic scattering with a defect is necessary to maintain momentum conservation, the D-band intensity is a widely accepted way of quantifying the defect density of nanotubes and graphene[22]. Additionally, the second-order Raman features of the G' and G+D exhibit large variations upon increased defect concentration as shown by Alzina et al.[38].

The defect density, as quantified by the peak intensity ratio of the D-band to the G-band feature (I_D/I_G), was correlated with θ at different exposure times t_{UV} in Figure 15(b).

It can be seen in Figure 15(b) that the I_D/I_G ratio does not change within the first 90 seconds of UV ozone exposure, while θ measured by etching changes monotonically. This indicates a limited sensitivity of the Raman I_D/I_G ratio to defects generated by ozone. This observation can be explained by the fact that the Raman signal of the D-band is proportional to the sum of the Raman signal coming from all of the defects within the laser spot and was found to be determined by $\frac{I_D}{I_G} = \frac{n_D(cm^{-2})}{7.3\times10^9 \cdot E_L^{\ 4}}$ (where E_L=2.33eV is the excitation energy in our experiments)[39]. Thus the minimum observable defect density as determined by the intensity contrast between the G-band and D-band is determined by noise, electronic amplification and background signal and cannot be smaller than 1 defect/$(1um)^2$. This detection limit could be insufficient for certain applications since it is shown subsequently that the electric properties of graphene devices might be sensitive to variations below this limit.

The analysis of etch patterns, on the other hand, has no such limitation to the minimum defect density. There is furthermore no theoretical limit for the minimum defect size. Single atomic defects could be considered the limiting case and we expect that even those

defects would be visualized by the etching procedure. Previous studies on the cutting of single-walled nanotubes have shown that the use ammonium persulfate etchant will exploit lattice defects and initiate an oxidation process starting at these lattice defect points. Thus, for high enough etchant exposure lattice defects would be widened and permeation of etchant through the film would amplify the defects. Experiments with higher quality graphene have to reveal if this ultimate sensitivity can be reached, since the current graphene is exhibiting too many larger openings that normally overwhelm the response from lattice defects.

Aside from its demonstrated high sensitivity, the graphene passivated etch analysis tool is selective only to openings in the graphene film and not to other kinds of imperfections such as PMMA residue or amorphous carbon, which, for example, would also contribute to the Raman D-band intensity [40].

2.7 Effect of defects on electrical transport

Finally, the impact of structural imperfections on the application of graphene is investigated. The electrical transport characteristics of ~60 graphene samples grown at different growth parameters were correlated with their defectiveness as quantified by θ. For this experiment, the sheet resistance and carrier mobility were extracted over an $8x8mm^2$ graphene area from 4 probe measurements in van-der-Pauw geometry. As expected, there is a wide variation of mobilities and sheet resistances that are thought to be caused by growth induced differences in the quality of the graphene films, i.e. through a different density of charged impurities[26].

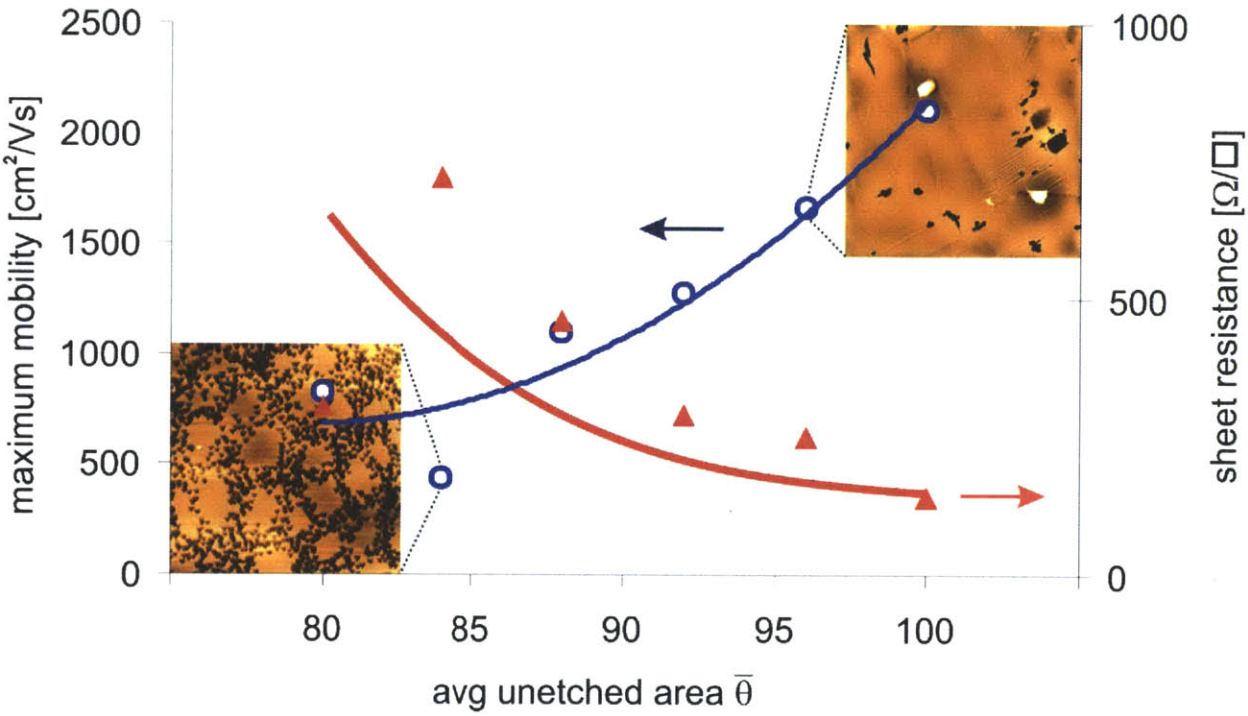

Figure 16 (a) Maximum mobility and corresponding sheet resistance for devices within an interval of graphene coverage. The insets show representative AFM images after 5s etch of graphene devices corresponding to the low and high mobility cases (scale 20x20μm²)

Figure 16 plots the highest mobilities obtained from samples that exhibit an average θ within a certain range. The range of θ was chosen to be 4% which is the average error of the measured θ within a sample caused by inhomogeneity across the macroscopic graphene film.

A clear trend can be seen for mobility and the corresponding sheet resistance of samples as a function of average θ.

The increase in mobility with increasing θ leads us to the following explanation: Graphene mobility is determined by different factors, for example charged impurity scattering and electron-electron interaction caused by high doping and structural defects[26].

According to Mathiesen's rule the process with the shortest scattering time or lowest mobility limits the overall mobility of the device. In the case of high mobility devices, charged impurity scattering and electron-electron interaction are low enough that scattering on lattice defects and openings determines the limit of the carrier mobility.

The increase in sheet resistance for decreasing θ can be explained by the less efficient transport of carriers in the presence of structural defects through scattering and confirms the previous explanation for decreased carrier mobility.

The finding that the maximum achievable mobility is determined by the presence of structural defects emphasizes the need for optimization of graphene growth and proves the value of the described analysis technique.

2.8 Challenges of the analysis technique

The described analysis technique can be destructive under certain circumstances: It was found that graphene would tear around the etch pits during a subsequent transfer process as shown in Figure 17(a). There are three situations when the tearing could occur:

- The graphene could be weakened through introduction of defects during the copper etching process. This option can be ruled out because of the proven resistance of graphene to the etchant. Furthermore Figure 17(b) demonstrates that the Raman spectra obtained from graphene transferred from unetched and etched Cu substrates are indistinguishable.
- The graphene could tear during the drying process when capillary forces due to the evaporating liquid could pull the graphene membrane into the etch pit.
- Tearing could occur during the application of PMMA during the transfer process.

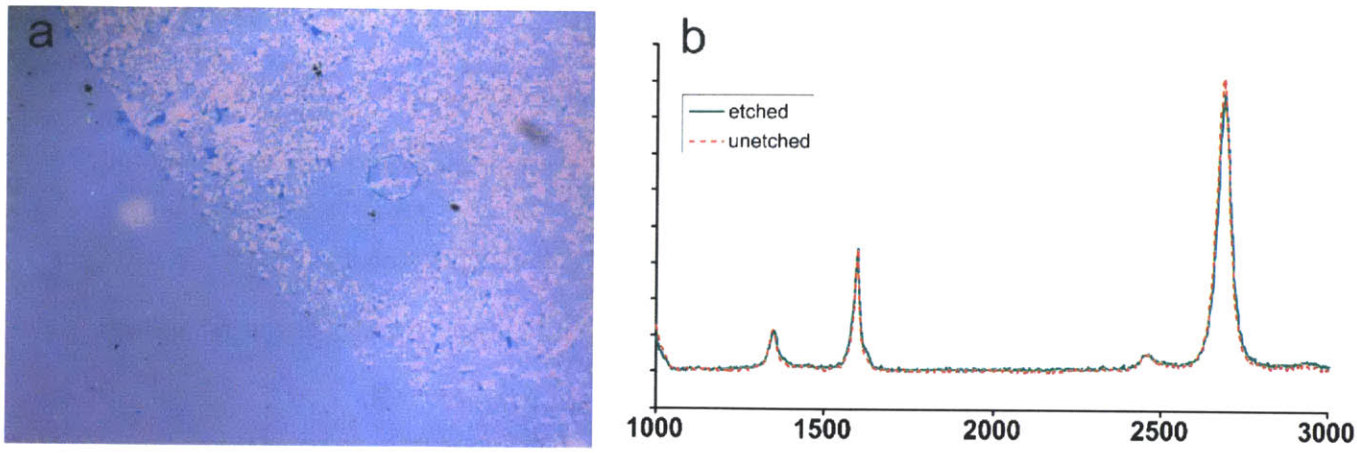

Figure 17 (a) Optical micrograph of graphene transferred from the etched and unetched parts of a copper substrate, (b) Raman spectra of etched and unetched graphene areas showing identical results

Defect-free graphene, on the other hand, would not exhibit underetching and the subsequent transfer process would not result in tears. Thus, the analysis technique is only destructive in the case of defective graphene, a material that would not warrant transfer anyways.

2.9 Summary

The process of graphene passivated copper etching described here could provide a simple metrology tool for the optimization of graphene synthesis. It can be routinely used to assess graphene surface coverage and continuity which makes this well suited for in-line quality control in industrial scale graphene fabrication processes.

In addition to its anticipated wide application in future graphene synthesis optimization, the described tool lends itself to the analysis of other CVD synthesized thin film materials, such as Boron Nitride[41] or BCN[42], which, due to their insulating character, limited light absorption, etc., cannot be easily investigated with traditional metrology tools.

Finally, the availability of the necessary materials and the flexibility of using many different imaging techniques make the graphene passivated etching approach well suited for comparing the results from different research groups and will be hopefully added to the metrology tool kit.

3. Study of structural defects in CVD grown graphene

3.1 Observation of graphene defects

In the previous chapter it was found that structural defects in the graphene grown by chemical vapor deposition occur at a surprisingly high density even for graphene sheets assumed to be continuous. Because of the limited sensitivity of other analysis techniques these defects have not been analyzed before and this chapter will be devoted to an investigation of their source and properties. Through understanding of their origin, a successful minimization of structural defects was accomplished.

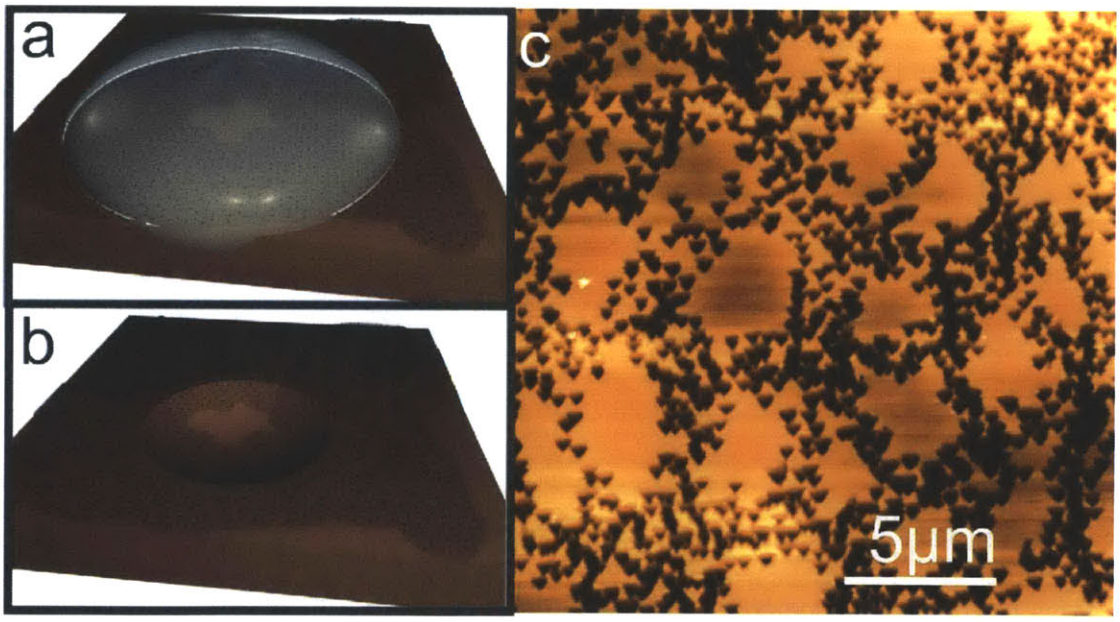

Figure 18 (a,b) Schematic of the analysis technique: (a) copper etchant is applied to a graphene sheet (b) holes in the graphene are permeated by copper etchant and generate etch pits in the Cu substrate, (c) AFM height image of graphene passivated Cu after a 10s etch

Figure 18 (a) and (b) summarizes the concept of graphene passivated Cu etching: A continuous graphene sheet would act as a barrier between the copper substrate and the

etchant. Holes in the graphene sheet, on the other hand, can be permeated by copper etchant (Figure 18(a)) which attacks the underlying copper substrate (Figure 18(b)). Thus, the analysis of the occurring etch pits in the copper (i.e. Figure 18(c)) can reveal aspects of the defectiveness of the graphene film.

Information on the resulting morphology can be obtained by many different imaging techniques (optical micrographs, SEM, etc.) and we focus on atomic force microscopy (AFM) here because of its sensitivity and its convenience of the analysis of etch pits.

3.2 Measurement of graphene defect size

The observation of the size of the occurring pits in Figure 18(c) is surprising since graphene films are assumed to be continuous[43] when grown under conditions that are normally used. The inability to recognize these defects with other analysis techniques raises the question about their dimensions. Attempts to directly measure this property reveal shortcomings of available analysis tools. The investigation of suspended graphene films by Transmission Electron Microscopy (TEM) does not reveal the predicted openings in the graphene[44]. This could be due to a limited field of view, since high resolution TEM studies can only be done on small areas, one at a time. Our studies suggest that the average defect density is less than 1 hole per μm^2, which would mean several images had to be taken to reveal one defect. Furthermore, openings in the graphene film result in dangling bonds that could lead to the formation of adsorbate clusters that are normally ignored during TEM analysis[45].

To overcome these challenges, we developed an indirect approach to measure the graphene hole size distribution based on atomic layer deposition (ALD). It was previously found by Wang et al.[46] that the deposition of atomic layers of aluminum oxide

would preferentially occur at defects in the graphene lattice. Thus, aluminum oxide is expected to form clusters preferentially at the openings in graphene and will start covering larger portions of the opening through subsequent ALD cycles. Since the aluminum oxide will etch at a significantly slower rate than copper, the cluster starts presenting an etching barrier when it reaches the size of the graphene orifice. Thus, the dimension of the openings in the graphene can be inferred from the etching behavior of a sample as the thickness of the deposited ALD film is increased.

When comparing the sample morphologies in Figure 19(a-c) a decrease in etch pit density with increasing ALD film thickness can be seen. This confirms that ALD deposited alumina will cover structural defects and passivate them, thus preventing the etching of the Cu substrate.

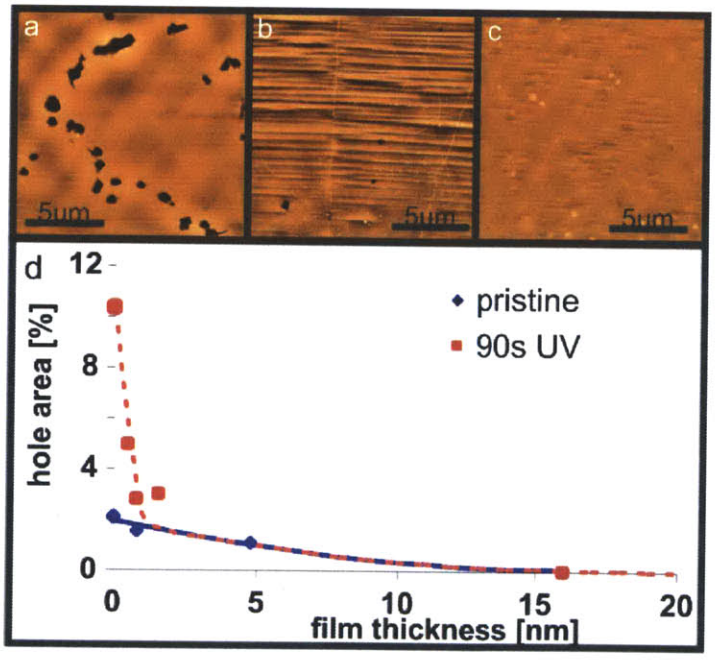

Figure 19 (a-c) Representative AFM height image of etched graphene (a) without, (b) with a 5nm ALD film, and (c) with a 16nm ALD film, (d)Relative copper hole area vs. deposited ALD film thickness for pristine and UV-ozone treated graphene films

When modeling the size of openings in the graphene film as following a Gaussian distribution of width δ, centered around d_0, the number of holes N(d) that are covered at a given ALD film thickness d are determined by the integral relation

$$N(d) = \int_0^d n_0 \exp\left(-\frac{(d-d_0)^2}{(C\delta)^2}\right) = n_0 erf\left(\frac{d-d_0}{C\delta}\right)$$

Here C is a geometrical factor that characterizes the overlap between the graphene hole and the growing Al_2O_3 cluster. Assuming that the cluster grows out symmetrically from one isolated dangling edge defect, then C=2.

The decrease in the number of permeable holes according to this model is calculated and the agreement of the fit with the experimental data in Figure 19(d) suggests that a Gaussian diameter distribution of openings is a valid assumption.

3.3 Generation of lattice defects

To further confirm the capability to measure the size of structural defects, a second experiment was performed: Exposure of graphene to ozone produced by the decomposition of oxygen under ultraviolet light is known to generate lattice defects[37]. When carefully comparing the morphology of a UV ozone exposed sample before and after etching (as seen in Figure 20), there are holes that correlate with the previous position of a particle, which will be explained subsequently. Additionally, there are etch pits that did not originate from a particle. These holes only occur for ozone damaged graphene and indicate the effectiveness of ozone to generate defects in graphene.

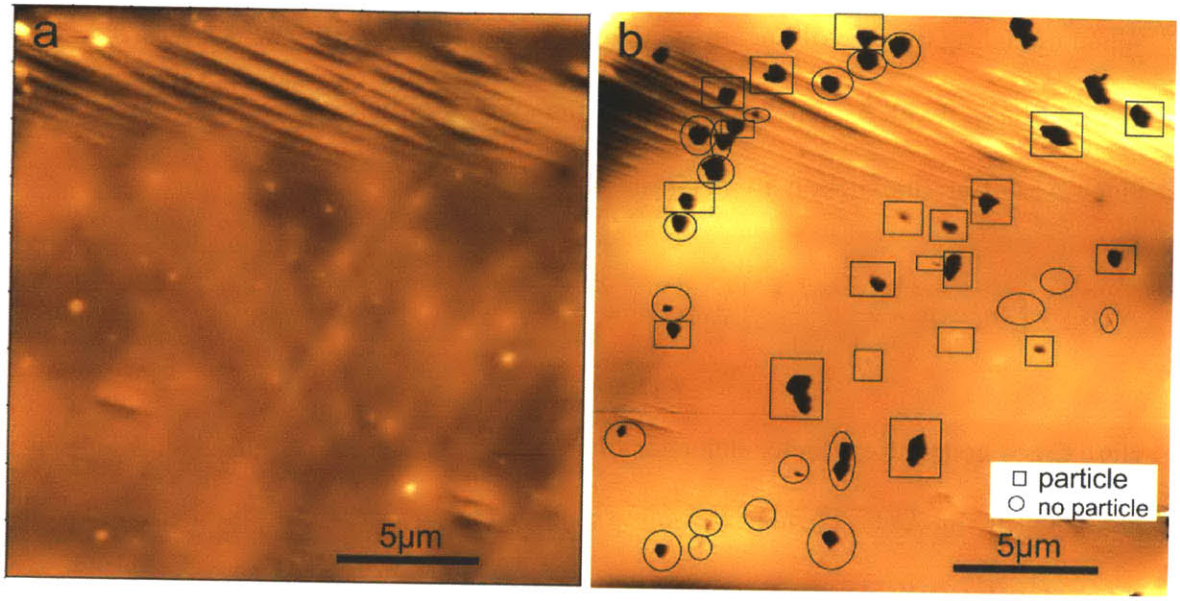

Figure 20 AFM images after 45s exposure to UV ozone before (a) and after (b) 10s etching. Squares indicate holes correlated with the position of a particle, circles are holes without a discernible particle

After 90s exposure of a similar graphene sample to UV ozone, more defects than for the control sample are observed as indicated by the higher concentration of holes in Figure 19(d). The fitting of the ozone exposed sample suggests that small defects are generated and covered by ALD which agrees with the hypothesis that lattice defects are generated.

From the fitting, the product Cδ can be extracted and under the assumption that C=2, the hole size of structural defects in graphene can be analyzed. Openings of 1.6nm for pristine graphene and 0.45nm for ozone generated holes were observed. These nanometer sized openings in the graphene offer the opportunity to investigate the nanofluidic behavior of graphene and explore their potential applications.

3.4 Fluid dynamic behavior of structural defects

Figure 21 shows the evolution of the sample morphology during etching. The same position on a sample was imaged before etching and in 5 second intervals during etching.

A linear increase of the dimensions of the etch pits (depth and diameter) with etch time (t_{etch}) can be observed.

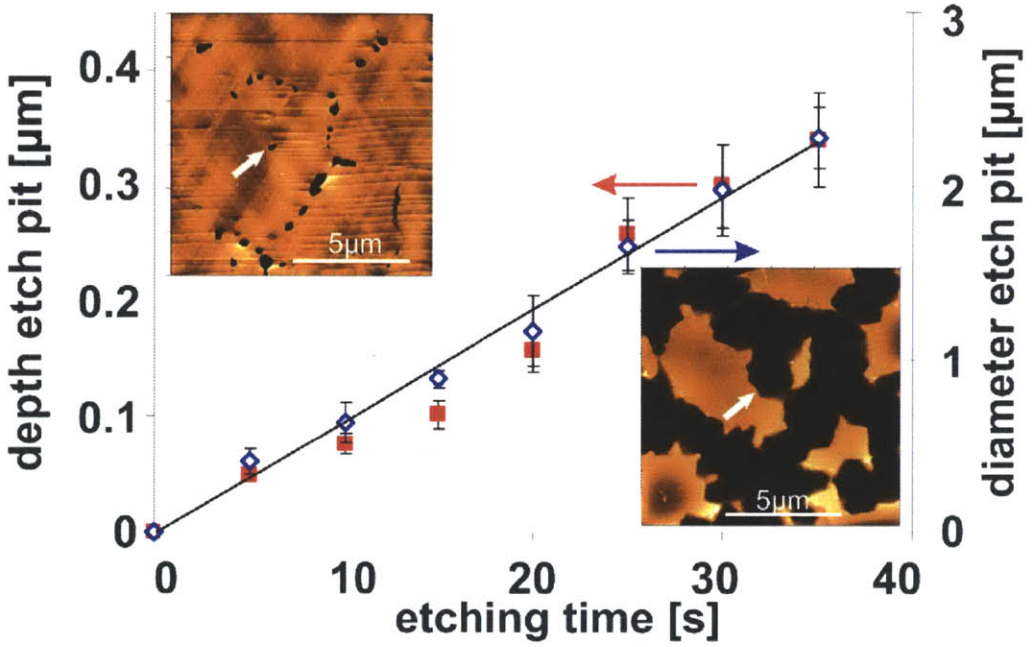

Figure 21 Dimensions (depth and diameter) of one etch pit vs. etching time with linear fitting. (Insets) Morphology of the same graphene sample after 5s (top left) and 35s (bottom left) of etching with indication of the measured etch pit (arrow)

This result is surprising considering that the graphene orifice should represent a barrier for the two processes necessary to etch the copper. First, the copper etchant has to permeate through the orifice to initiate etching. During the etching process, exchange of reactants through the hole is required to sustain the copper removal. The etching rate could be limited by either of these two steps and their behaviors with etching time t_{etch} have to be elucidated. If the etching is diffusion limited, there should be a direct proportionality between the etch time and the etched volume for small holes as predicted by Kuiken[47], and thus the etch pit diameter and depth should scale with $t_{etch}^{1/3}$. Assuming

that permeation of the etchant into an empty volume was the rate limiting step, a proportionality of etch pit dimensions with $t_{etch}^{1/3}$ would be expected as well.

A constant etch rate, as observed in Figure 21, is expected only for reactant exchange through openings that are much larger than the resulting etch pit. A simple explanation for the occurrence of a constant etch rate would be that large area tearing of graphene happens during the etching process and subsequently big openings occur by the removal of the graphene film during rinsing after each etch step. This stepwise increase in hole size, however, should result in a variation of the etch rate. For example, the etch rate of the first step should be noticeably smaller than later ones since the initial opening would have been much smaller as the tearing and removal of graphene would have only occurred after the first etch and rinse step. The absence of such a behavior is a first, strong indication that graphene tearing is not the origin of the large etch rate.

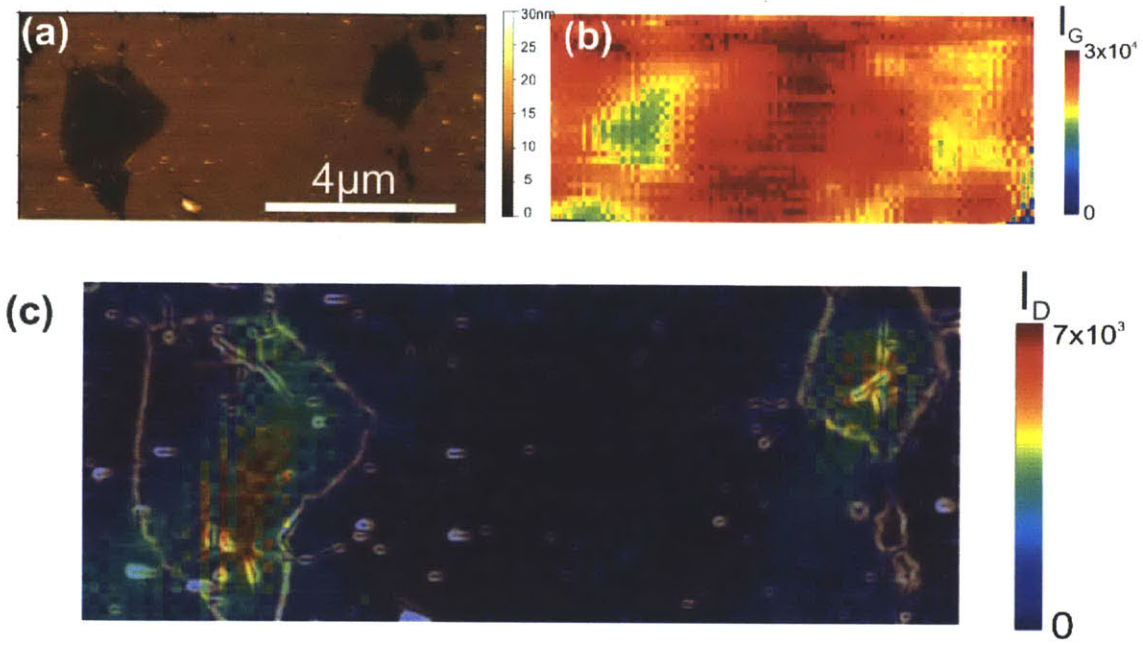

Figure 22 (a) AFM height image of graphene passivated SiO_2 after 30s buffered oxide etchant, (b) Spatial Raman map of the G-band intensity, indicating the presence of graphene throughout the sample, (c) overlay of etch pit boundaries obtained by AFM (bright lines) and Raman D-band map (colored areas)

To further confirm the presence of graphene within the etch hole, Raman spectroscopy was employed. Since the Raman response of graphene on a conductive copper substrate is weak, conditions similar to the graphene undergoing a passivated copper etch were simulated on a Si/SiO_2 substrate. The sample was subjected to a buffered HF oxide etch that damaged the SiO_2 without affecting the graphene, and the results are shown in Figure 22. Etch pits similar to the copper case occur in Figure 22(a) and show that the approach of graphene passivated etching can be extended to different substrates. The Raman map in Figure 22(b) shows the presence of graphene (indicated by a non-vanishing intensity of the Raman G-band) throughout the sample and within the etch pit. Finally, a correlation between the defect induced D-band and the etching morphology is demonstrated in Figure 22(c): The graphene areas with high D-band peak intensity coincide with the

position of the etch pits in the silicon, thus supporting the concept of structural defects as the origin of etch pits.

The measured increase in etch pit depth on graphene passivated Cu was compared to the etch rate of bare copper. For this experiment, annealed Cu foil was partially covered with tape and then exposed to Cu-etchant. After removal of the tape, the step size between the protected and the unprotected side was measured using AFM. The etching rates extracted from Figure 23 are similar for bare and graphene passivated Cu which suggests that the transport of etchant through the opening in the graphene membrane is not limiting the etching process.

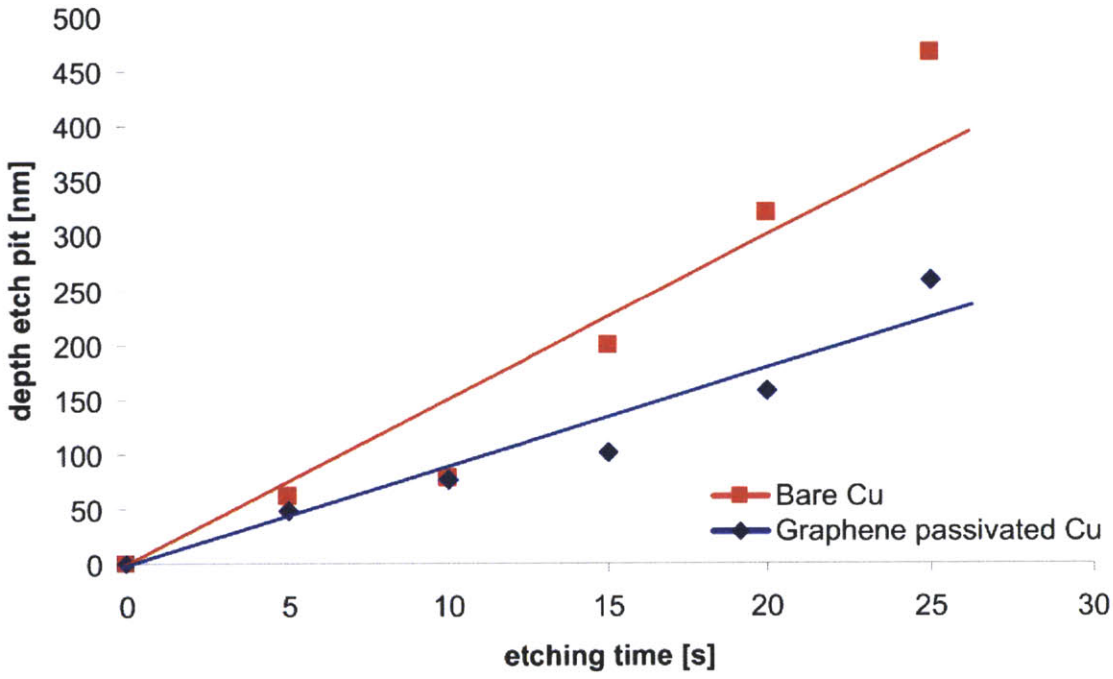

Figure 23 Comparison of etch rates of bare copper substrate and etch pit depth of graphene passivated copper substrate

Evidence for the fast transport of etchant occurring along the graphene is given by an observed anisotropic etching of the substrate. From the different ordinate scales in Figure 21 it can be seen that, although the etching behavior with time is similar, the etch rate in the lateral direction is ~3x larger than perpendicular to the graphene membrane. This larger etch rate along the graphene plane was previously observed in the fabrication of graphene devices and attributed to capillary action[48]. This explanation is furthermore supported by the observation shown in Figure 24: The shape of the etch pit occurring after 10s etching seem to follow wrinkles in the graphene that could be identified before etching. These wrinkles are expected to be composed of folded graphene and the close proximity of two graphene layers seems to increase the mobility of the etchant along the wrinkle.

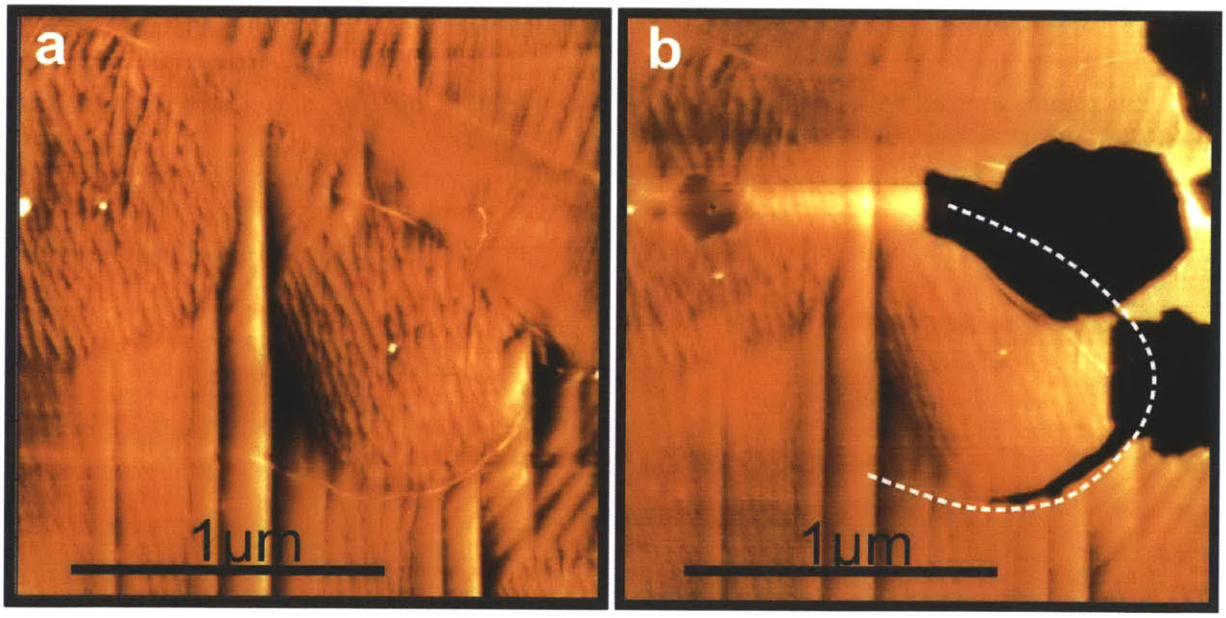

Figure 24 AFM image of region before (a) and after 10s etching(b), lines indicate location of wrinkles before etching

To estimate the etchant permeation speed through the graphene film, the fluid flow required to fill an etch pit through an orifice within a certain time can be calculated. The filling time could be inferred from a decrease in the etching rate for large enough etch pits when the fluid transport is limiting the etching rate rather than the etching reaction. In our experiments, however, no such decrease in etching rate was observed, suggesting that the time it takes to fill even large holes is very small.

In a separate experiment in collaboration with Prof. Hsieh (National Chung-Cheng University, Taiwan) the formation of etch pits in graphene passivated Cu foil was monitored in an optical microscope during an $FeCl_3$ etch. This allowed the analysis of the evolution of one etch pit in time with unprecedented accuracy as shown in Figure 25. It can be seen that the growth of the etch pit slows down and eventually halts (as fitted by an $1-\exp(-t/\tau)$ functional). This behavior indicates that the etching process is not kinetically limited by permeation through the graphene, but only slows down when the etchant is exhausted upon saturation with Cu. Thus, even for long exposure times and large etch pits, the permeation of molecules through the graphene is not limiting the etching process.

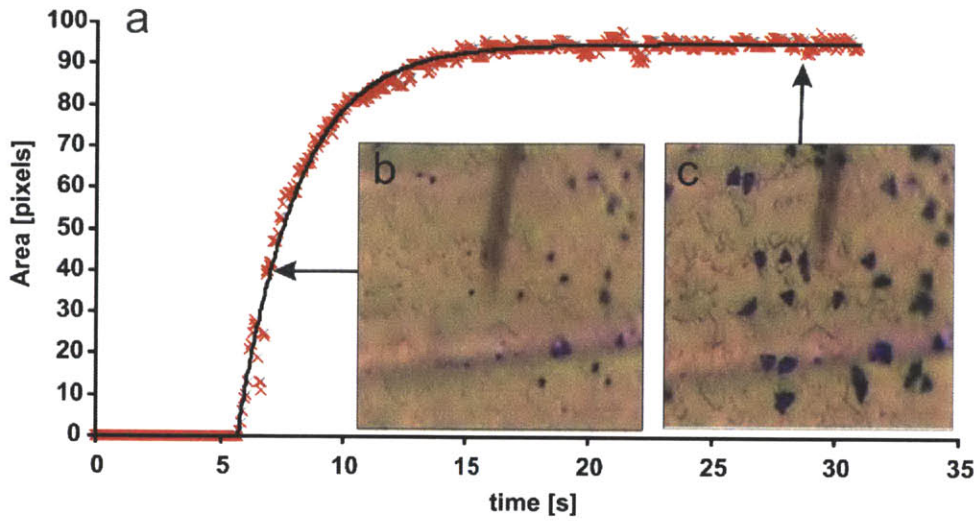

Figure 25 (a) Evolution of the area of one etch pit and fit, (b,c) two representative pictures and an indication of the time each image was acquired.

Instead of determining the exchange rate of molecules through the graphene opening during the etching process, we attempt to estimate the speed at which etchant permeates into an empty hole that is covered by the graphene membrane. An order of magnitude estimate can be attempted by analyzing the flow of etchant into an empty pit of 2.2x0.3μm (as obtained after 35s etching). The filling time was estimated to be less than 0.3s since etching still occurred for this exposure time. Assuming an orifice diameter of 1.6nm, the etchant permeation speed through graphene has to be larger than 2.4m/s to fill the etch pit within the given time.

More work is necessary to extract an experimental value for the filling time and to compare it with the theoretically calculated permeation speed of 20m/s by Suk et al.[49].

The small size of the holes in the graphene film combined with the measured large etch rate emphasize the intriguing fluid dynamical properties of graphene and will hopefully stimulate more work in the science and applications of graphene based nanofluidics.

3.5 Origin of defects

In the second part of this chapter the origin of the investigated structural defects in graphene is studied. When analyzing the position of many etch pits with respect to each other (i.e. in Figure 18(b) or the insets of Figure 21) it can be seen that the etch pits occurring in the copper substrate are not randomly arranged. Two types of formations are found after etching: The etch pits are either arranged in lines that form loops or individual etch pits are located within these loops (see Figure 21). These formations are investigated in more detail in Figure 26.

Figure 26(a) shows the graphene passivated copper sample before etching and here several particles can be seen on the surface. When comparing the location of these particles with the sample morphology after etching, a clear correlation can be found between the particle locations and the etch pits formed (Figure 26c)). The origin of these particles can be deduced from their arrangement on the graphene as described below.

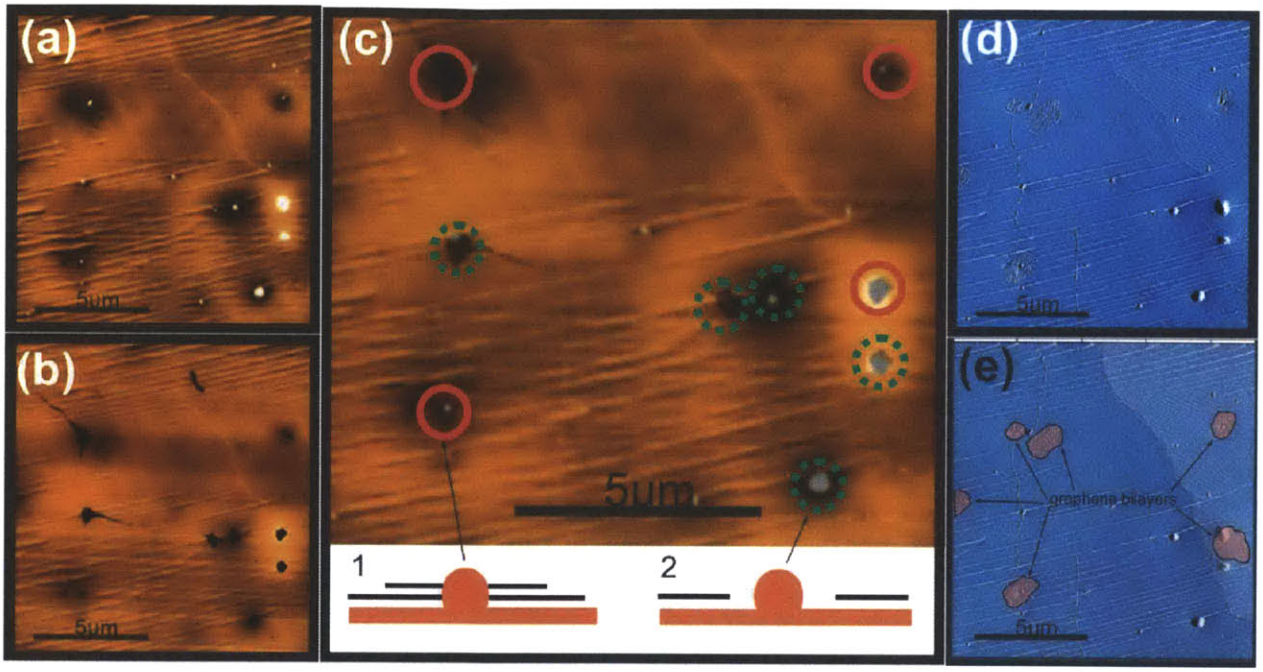

Figure 26 AFM height images of the same location on a graphene passivated copper sample (a) before etching, (b) after 10s etching, (c) overlay of both images with an indication of proposed type of defect, (inset) types of defects resulting in etch pits: (1) nucleation region and (2) surface imperfection, (d) AFM amplitude image of the same area as (a-c) before etching, (e) depiction of different textured regions in (d) with indication of the presence of bilayer regions.

As found previously[28], there is a group of particles that seem to form closed loops on the boundary of a graphene grain. Because of the particle height (~25nm), graphene is not able to cover their surface. Additionally the particles seem to adhere well to the substrate and they are not lifted up by the growing graphene. Thus graphene can only grow around those particles, and after etching they consequently leave behind a hole in the graphene film.

Since graphene is known to exert a force along the growth front[50], these impurities (as depicted in illustration 2 of Figure 26(c)) could be pushed in front of the growing graphene until the graphene growth stops. This model can therefore explain the arrangement of the particles found at the graphene boundaries.

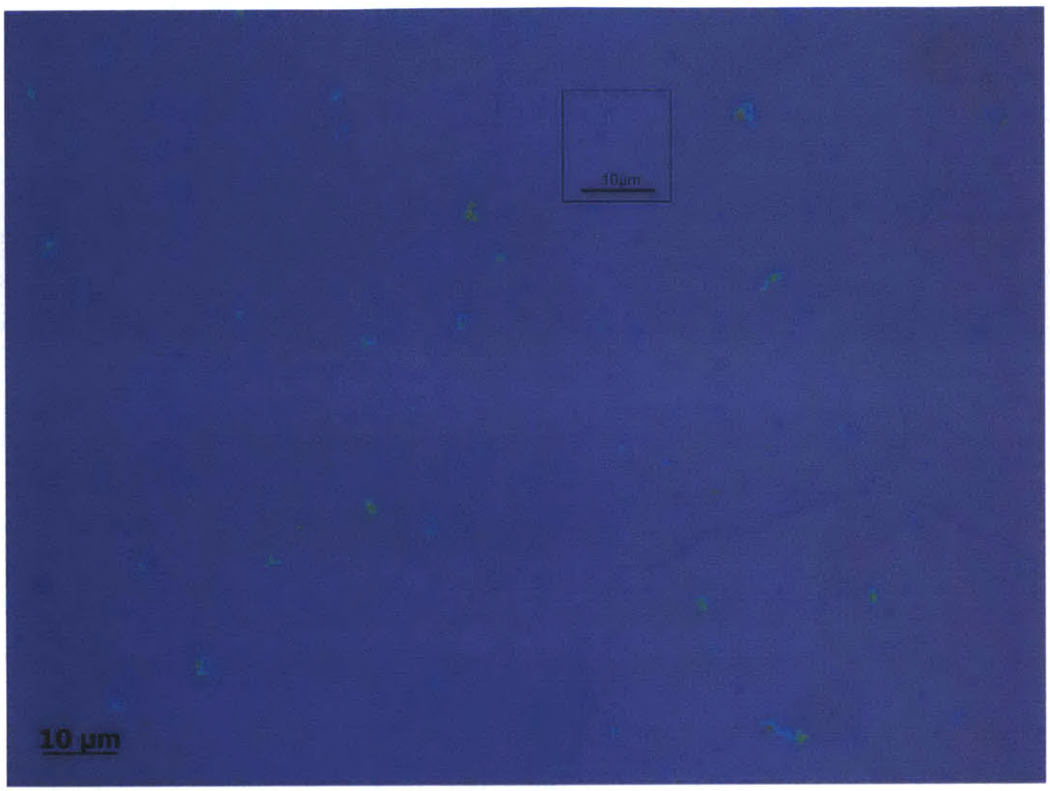

Figure 27 (a) Optical microscope image of a graphene sample identical to the one in Figure 26 after transfer to Si/SiO_2. Bi-layer graphene occurs as darker islands on the continuous graphene sheet. (AFM scan size of Figure 26 is indicated as rectangular box)

A second group of nanoparticles usually occurs individually and within a grain boundary. When comparing the height and amplitude information of the same AFM image (Figure 26 (a) and (d)), it can be seen that there is a group of particles that is accompanied by island shaped variations in the copper texture (highlighted in Figure 26 (e)). These regions were identified as bilayer regions by correlating their size and density with optical micrographs of graphene after transfer onto Si/SiO_2 substrates (Figure 27). Graphene bilayer regions were previously observed by Li et al.[15] under similar growth conditions.

The differences in the texture of the copper for bilayer and monolayer graphene, as observed in Figure 26 (d) can be explained by analysis of the growth process. Variations in the thickness of graphene are expected to have an influence on the restructuring of the substrate during graphene growth since the copper atoms experience different friction coefficients when interacting with single and bilayer graphene[51].

A nanoparticle can be found in the center of each assigned bilayer graphene region which suggests that the particle could be a nucleation site for graphene growth, as reported by Huang et al.[28]. This hypothesis is supported by calculations[52] that show that the nucleation of graphene on the edges of clusters provides a lower energy pathway than nucleation on a flat crystal facet and this nucleation process was observed experimentally for both nanotubes[53] and graphene[50].

As indicated in Figure 26(c) the particles within the bilayer regions (designated by red circles) are attacked during etching (which furthermore indicates that these particles are not composed of carbon) and the etching process leaves behind openings in the underlying graphene layer that result in etch pits in the copper substrate. This shows that the continuous single layer graphene sheet did not encapsulate the particle. From this morphology we infer that graphene layers originate from the side of the observed cluster instead of completely enveloping it (see illustration 1 in Figure 26(c)). The lower energetic barrier to nucleating a graphene sheet from a nanoparticle hints to the significance of these imperfections for graphene growth.

These findings emphasize the importance of minimizing the density of particles on the Cu substrate when trying to grow continuous graphene films.

3.6 Minimization of graphene defectiveness

There are three possible sources of the observed clusters on the Cu substrate after growth

- Surface imperfections on the copper foil that could be originating from production, contamination or handling.
- Dust particles could accumulate on the Cu substrate as a result of exposure to the atmosphere as hypothesized by Vlassiouk et al.[54]
- Heterogeneous particles stemming from impurities that precipitate out of the copper foil through surface segregation[55] during the high temperature treatment.

To determine the source of particles, the defectiveness of graphene grown on different Cu substrates was analyzed. The effect of electropolishing on low purity copper foil (99.8% Cu) was tested by comparing the occurrence of etch pits after growth. (To minimize the effect of variations from growth to growth, all samples were grown at once.)

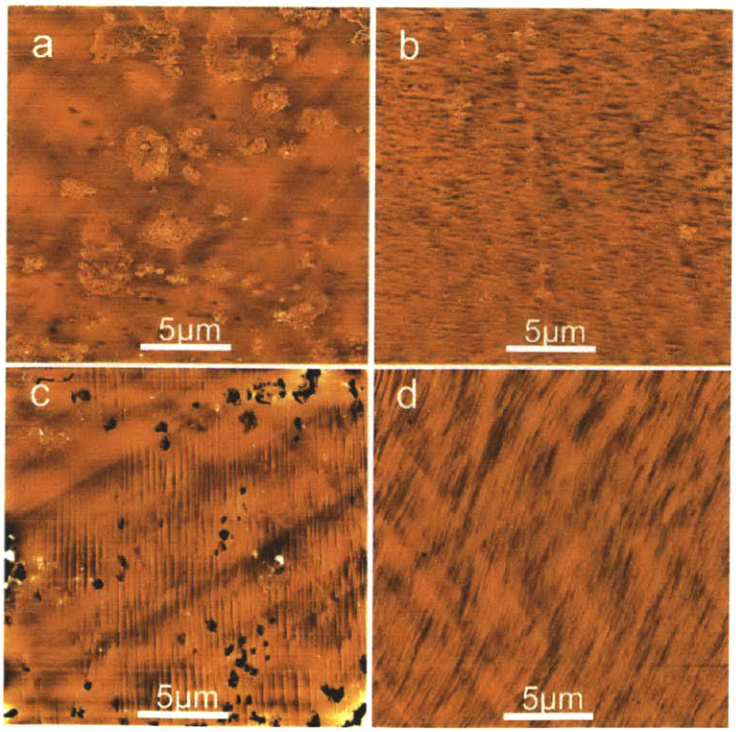

Figure 28 (a) AFM images of sample morphology before (a-b) and after etching (c-d) for pristine copper foil(a,c) and electropolished copper foil (b,d) .

Electropolishing the Cu foil at 2V for 30 minutes resulted in a much lower particle density as can be inferred from the comparison of Figure 28(a) and (b).

The density of structural defects was revealed by 10s etching. It can be seen that for the electropolished sample in Figure 28(d) the defect density is virtually zero which allows several important conclusions to be drawn.

- The normally observed defect density is not determined by dust particles on the Cu foil since the density of these particles would have not been affected by Cu pretreatment.
- Precipitates from the bulk do not seem to limit the quality of the graphene since electropolishing only removes the top layer and would not affect the chemical composition of the bulk material.
- Surface imperfections are the main source of defects in low purity Cu foil and their removal can result in high quality graphene growth as recently confirmed for atmospheric pressure CVD by Han et al.[56].
- Vacuum annealing for 30minutes at 1000°C alone is not sufficient to remove these surface imperfections.

4. The effect of promoters on the growth kinetics of CVD graphene

The previous chapters have focused on analyzing the source and density of a type of structural defects that can be observed in graphene grown by chemical vapor deposition: These defects, however, are only a part of the problem that CVD synthesized graphene is facing. Another source of defects could be incompletely grown graphene, which has the potential to have a more significant impact on the properties of graphene.

Overcoming this issue requires a better understanding of the graphene growth process. A second benefit of a detailed knowledge of the growth process is the potential to reduce the growth temperature, increase the growth rate, etc. which is of interest for the commercialization of CVD grown graphene.

This chapter aims at providing quantitative information about the graphene growth process. The use of promoters is demonstrated as a potential route to improving the quality of graphene and the effect of promoters on the graphene growth kinetics is analyzed.

4.1 Application of graphene passivated etching to growth studies

As described in the previous chapters, the graphene passivated etching procedure was found to be useful to visualize the gaps between neighboring graphene domains as seen in Figure 29(b). Additionally, we have previously demonstrated the high sensitivity of the characterization technique and found that vacancies between merged grains -which are invisible to other metrology tools- can be identified (Figure 29(c))).

To quantify the changes in morphology of the etched graphene we denote the relative unetched area of copper substrate as θ. This parameter represents a lower boundary for the graphene surface coverage. θ is not a constant but increases with etching time through under-etching of copper in the vicinity of graphene openings. By adjusting the extent of under-etching, the sensitivity to very small defects can be tuned. Figure 29(c) shows the graphene coverage under optimized conditions and the holes observed were found to be caused by particles located on the copper substrate. The presence of those particles would contribute to the openings in the graphene film, leading to a smaller value of θ. Thus, θ is identical to the graphene surface coverage only for vanishing etching time and in the absence of surface impurities. Changes to θ under identical experimental conditions, however, are expected to reflect changes to the graphene coverage which makes θ a suitable parameter for the study described here.

4.2 Catalyst deactivation during graphene growth

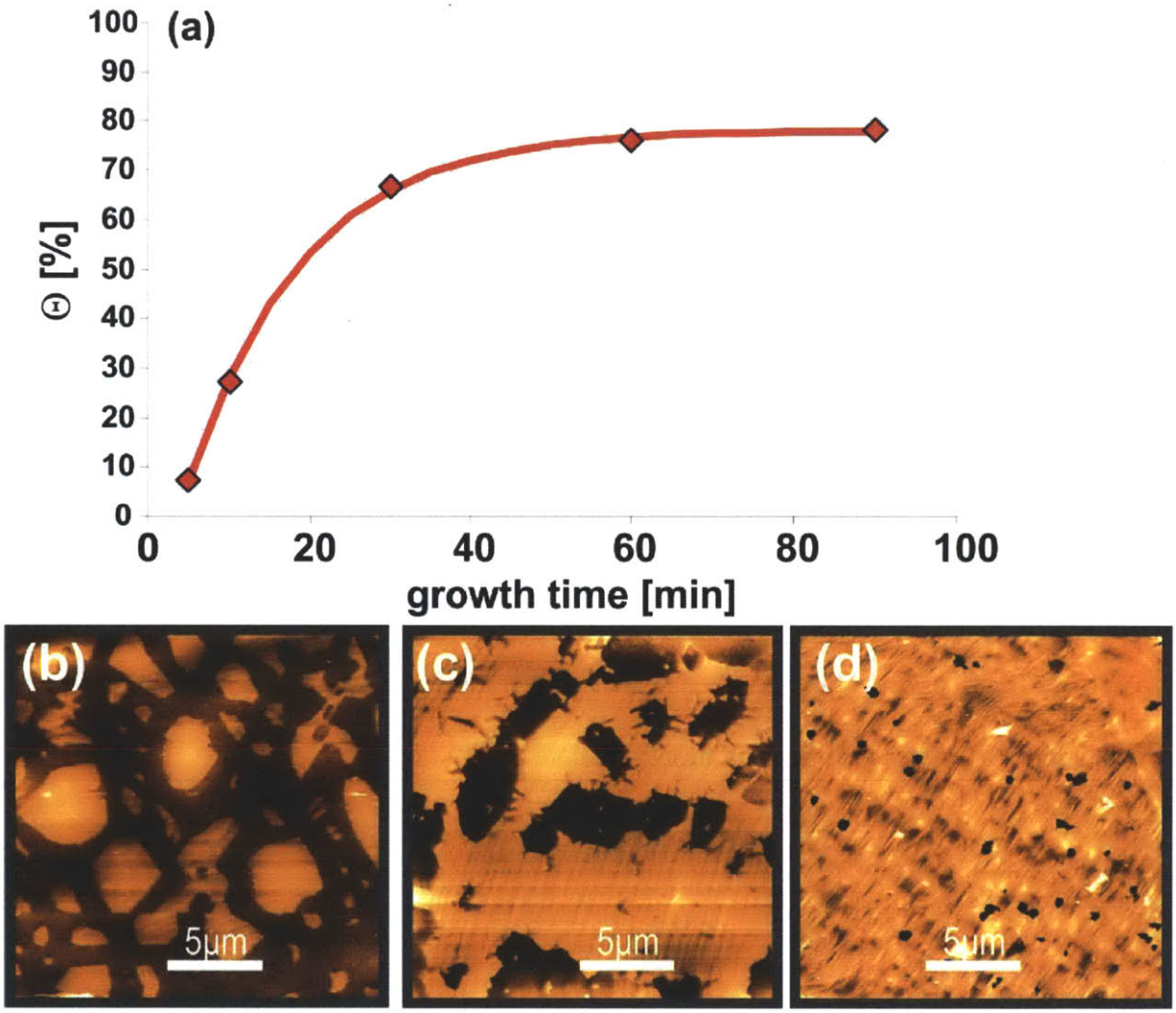

Figure 29 (a) Evolution of θ vs. growth time, (b-d) morphology of samples after 10s etch obtained by AFM (b) after 10mins growth (c) after 90mins growth, (d) for growth under optimized conditions (2Torr, 40minute growth θ=95%)

Figure 29(a) shows the evolution of θ with time. It can be seen that under low pressure conditions θ has an asymptotic behavior, as observed previously by Colombo et al.[57], which indicates that the growth rate of graphene domains decreases during the growth process. This reduction in growth rate can be explained by a lower catalytic activity of

the copper through passivation of reaction sites. This passivation process is caused by the increased surface coverage of graphene and is a phenomenon known in catalysis as "catalyst poisoning" or "coking"[58]: When the copper substrate is almost entirely covered with graphene, no new carbon radicals can be supplied through the catalytic conversion of methane and holes remain in the film. This behavior presents a fundamental limitation of many graphene synthesis methods that are based on catalytically active metal substrates which are covered by a graphene layer during growth (Cu[43], Ir[59]). Other substrates such as Ni do not experience the same limitation since they generate the graphene layer by carbon precipitation from the bulk during cooling[17]. This difference in growth mechanism is linked to the self limiting growth process. In order to enable the robust synthesis of single layer graphene the issue of catalyst deactivation has to be overcome.

A solution for this challenge is the introduction of a promoter. Traditionally, the use of a heated filament in diamond CVD[60] as well as the introduction of a second catalytic material in nanotube growth[61] has resulted in a higher yield of the synthesized material or a higher quality of the growth. Recently, bilayer graphene has been obtained by transport of carbon fragments from one copper substrate to a graphene covered sample that was positioned downstream[62] and thus the first substrate promoted the growth process on the downstream sample.

In this article, we will describe the effect of a promoter on the growth kinetics of graphene. First, the rate limiting step in the graphene growth process is determined. Then, the role of a promoter and its influence on graphene growth is elucidated. Finally, several

promoters are compared in their ability to improve the graphene coverage and growth rate.

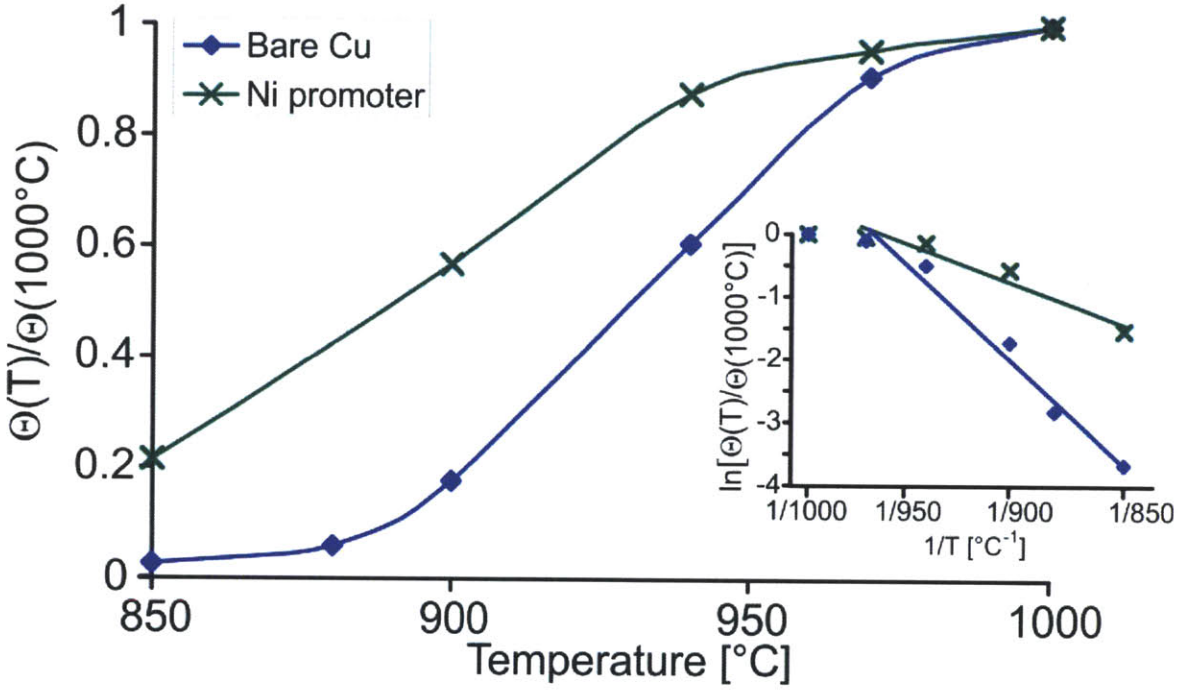

Figure 30 θ normalized to value at 1000°C as a function of temperature with and without Ni promoter (inset) Arrhenius plot

4.3 Graphene growth kinetics

To quantify the kinetics of graphene growth, we analyze θ as a function of growth temperature. For a sufficiently short growth time, the growth rate can be assumed constant and $\theta(T)/\theta(T_0)$ is proportional to the growth rate. Nickel was selected as a promoter because of its ability to catalyze graphene growth [17]: A piece of Ni foil (Alfa 44821) was placed in the reaction zone close to the Cu foil and the growth conditions were optimized at 1000°C growth temperature.

Figure 30 shows the resulting θ after 10 minutes of growth at different temperatures obtained with and without a promoter normalized to the coverage at 1000°C. It can be seen that the use of a promoter increases the surface coverage at a given temperature and shows promise for low temperature graphene growth.

The inset of Figure 30 shows an Arrhenius plot of the same data and a linear slope in this plot indicates a thermally activated process. The deviation of the data points at 1000°C from the linear fit can be explained by the breakdown of the previously made constant growth rate assumption. (For high temperatures the growth duration becomes too long for a constant derivative and the coverage stagnates in time). The activation energy of the rate limiting process step can be extracted from the slope. For bare Copper the activation energy was determined to be 3.7eV while in the case of the Ni promoter a lower activation energy of 1.5eV was found. These energy barriers are close to the theoretically predicted activation energies for the dehydrogenation reaction of methane on copper (3.6eV)[63] and on nickel (1.32eV)[64]. This agreement suggests that at the investigated growth condition the decomposition of methane into carbon radicals has a higher energy barrier than the other growth steps and thus is the rate limiting step in the synthesis of graphene. The difference in energy barrier heights furthermore indicates that the catalytic dehydrogenation of methane on the Ni promoter proceeds more efficiently than on the copper substrate only.

4.4 "Distributed catalysis" model of promoter assisted CVD

In order to reconcile these experimental observations, a model of "distributed catalysis" is proposed: First, carbon radicals are generated by the promoter and then they are incorporated into the graphene lattice by the copper. Thus, the graphene growth process,

which is normally accomplished by the copper substrate alone, in the "distributed catalysis" regime is divided between the two materials.

The details of the mechanism in which the distributed catalysis occurs have to be studied further, i.e. through in-situ mass spectroscopy, but some conclusions can be drawn from theoretical calculations.

Zhang et al. [63] calculated that the formation of carbon on copper is thermodynamically unfavorable. This is indicated by the higher formation energy of atomic carbon on Cu than adsorbed CH_4 which means that the backward reaction will proceed more efficiently and carbon radicals will hydrogenate rather than dehydrogenate further[11]. Thus, all intermediate reaction steps have to be overcome collectively and the reaction speed is determined by the overall energy difference of 3.6eV. Conversely, the dehydrogenation of Nickel has a maximum energy barrier of 1.32eV. We hypothesize that the formation of atomic carbon in the promoter system proceeds by the dehydrogenation of CH_4 into C* radicals on the Ni surface and subsequent diffusion of the material onto the Cu surface. An alternative reaction pathway could be the dehydrogenation of CH_4 into CH* on Ni and the subsequent decomposition into C* on the Cu sample. We cannot rule out this process because the maximum energy barrier for this pathway would be 1.97eV, as opposed to 1.32eV for the first pathway, which is within our measurement errors.

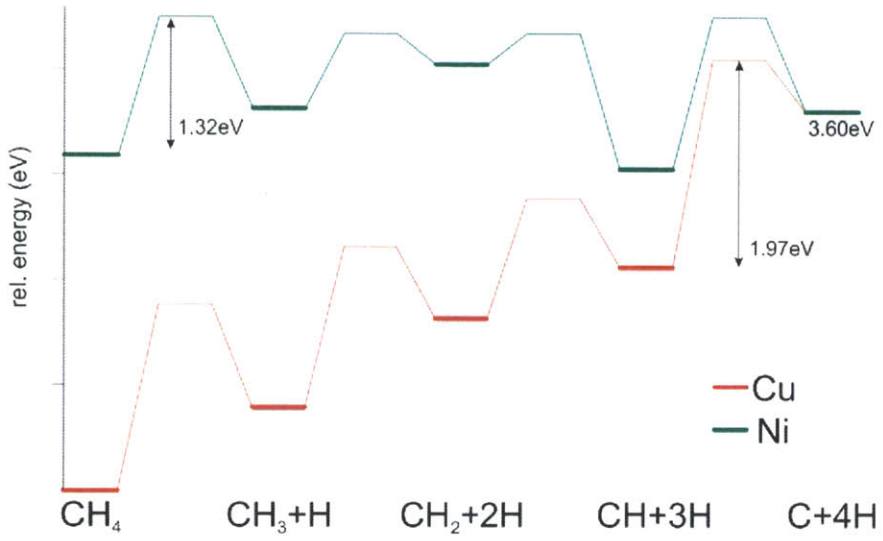

Figure 31 Energetic pathways for the dissociation of methane on Ni and Cu [63, 65]

4.5 Experimental confirmation of model

To confirm the model of distributed catalysis, the influence of the promoter on graphene growth has to be studied. This can be achieved by varying the concentration of carbon species generated by the promoter and correlating it with the resulting change in the graphene coverage on the Cu substrate.

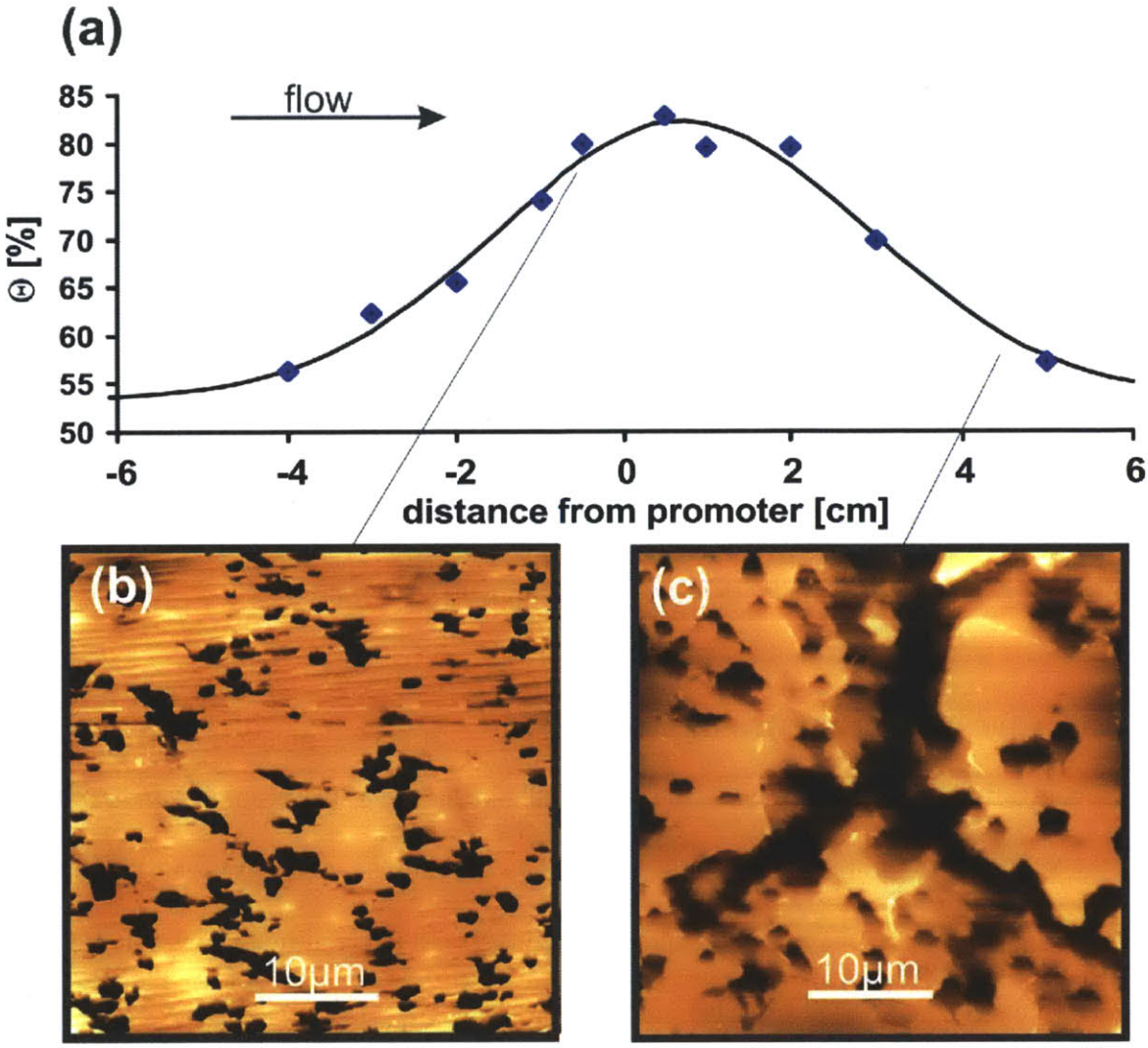

Figure 32 (a) θ vs. distance from Mo promoter (b) and (c) representative AFM images taken at different distances from the Mo promoter as indicated by the arrows

The effect of varying the concentration of carbon radicals can be studied by measuring θ at different distances from the promoter. Since the concentration of the carbon radical species varies spatially with respect to the promoter, as determined by their lifetime and diffusivity[66], the spatial variation of the graphene coverage reveals the effectiveness of the promoter.

To analyze the spatial variation with respect to the promoter, a piece of foil of the promoter material was positioned close to Cu substrates upstream and downstream as indicated in Figure 33. The off-center position of the sample with respect to the heating zone was chosen so that variations in temperature across the reaction zone would vary monotonically across the sample.

In addition to Nickel, Molybdenum was used as another promoter in this set of experiments because of its proven ability to convert methane into higher hydrocarbons[67]. The presence of certain higher hydrocarbons was found to be significant in the growth of carbon nanotubes[68] and a similar mechanism could be envisioned for graphene growth.

Figure 32(a) shows the variation of θ with position relative to a piece of molybdenum foil acting as a promoter. A clear maximum can be found in this plot that coincides with the position of the promoter. A similar behavior was also observed for the Ni promoter. This indicates that the promoter indeed has a beneficial effect on the growth of graphene and increases the coverage of graphene under the same growth conditions.

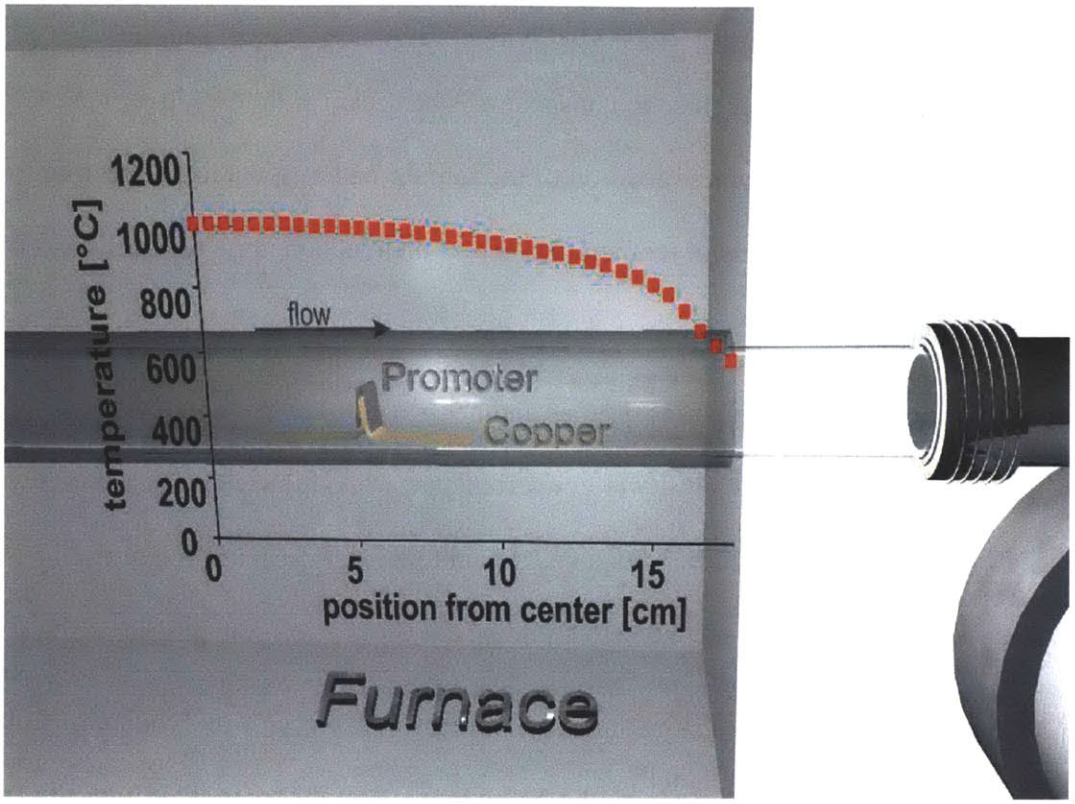

Figure 33 Schematic of the position of the promoter in the CVD setup with measured temperature distribution in the furnace

The described change in surface coverage is illustrated when comparing two representative AFM images (Figure 32(b) and (c)) which show that close to the promoter there are fewer etch pits in the copper foil, indicating that the protecting graphene layer had fewer openings compared to positions further away from the promoter.

This behavior has to be correlated with predictions for the concentration of carbon-radical species within the reactor. Close to the promoter surface the radical concentration is determined by the promoter's catalytic activity. The spatial distribution within the reactor is affected by a number of factors, such as the diffusion of a given radical, its reaction rate to forming other carbon species, temperature induced variations of the diffusivity,

and convective mass transport due to the gas flow. Some of these parameters, however, are expected to have only a small effect on the concentration profile: As shown in Figure 33 the temperature variation over the sample is relatively small and is not expected to be of significant influence. Also, for LPCVD growth, the Sherwood number, which compares convective and diffusive mass transfer coefficients, is small[69]. Therefore, the convective transport (i.e. flow) is expected to be negligible compared to diffusive transport.

Thus, the main factors controlling the carbon radical density are predicted to vary symmetrically around the promoter giving rise to a concentration profile of the form

$$C(x) = C_0 \cdot \exp\left(-x^2 / 2\delta^2\right) + C_1,$$

where C_0 is the concentration of carbon species close to the promoter, x is the distance from the promoter, $\delta = D/k$ is the ratio of the diffusivity of the carbon species D and its reactivity k and C_1 is a constant concentration caused by the catalytic generation of the carbon species by the copper substrate.

The solid line in Figure 32 represents the fitting to this concentration profile and agrees very well with θ thus indicating the importance of the concentration of the carbon species generated by the promoter on the graphene film coverage.

A comparison of the extracted value for d with predictions could corroborate our model.

The extracted value of δ=2.21cm is in the same order of magnitude as the mean free path λ of a carbon radical from the formula $\lambda = \frac{RT}{\sqrt{2}\pi d^2 N_A p} = 1.03cm$. This simple estimation

considers the distance between collisions of gas molecules and cannot provide and lacks several parameters for an accurate description of the system:

- The heterogeneity of the gasses in the reactors is not captured.
- Not every collision of a carbon radical with other molecules will result in a reaction.
- Diffusion and flow effects are not considered.

Thus, a more realistic prediction is attempted by using the CHEMKIN software package from reaction design. This software simulates complex chemical reactions in the gas stream based on empirical values for reaction rates. The experimental setup was approximated with a radial symmetric reactor at 1000°C. Boundary effects were neglected and the plug-flow-approximation was used. The effect of the promoter was simulated by supplying carbon radicals through an inlet at x=0. A reactant ratio of 1/100 of carbon radical and H_2 was introduced with a flow rate of 18sccm and a base pressure of 640mTorr which represents the experimental condition used.

Figure 34 shows the calculated concentration profile in the reactor. This calculation demonstrates that carbon radical species generated at the promoter can indeed diffuse for several centimeters and the experimentally observed length scales are reasonable. It can furthermore be seen that the concentration profile is sensitive on details of the chemical reactions. Figure 34 compares the C* concentration in the reactor for the case that the promoter generates C* radicals with the condition that CH* radicals are produced by the promoter. The larger decay length of the concentration profile for the CH* radical source is caused by the change in reaction pathways. The formation of C* radicals from a CH*

radical source can occur through gas phase reaction at the investigated temperatures. Thus, the concentration profile for the CH* source reflects a production and consumption of C* radicals while only a consumption of C* radicals occurs for the C* source.

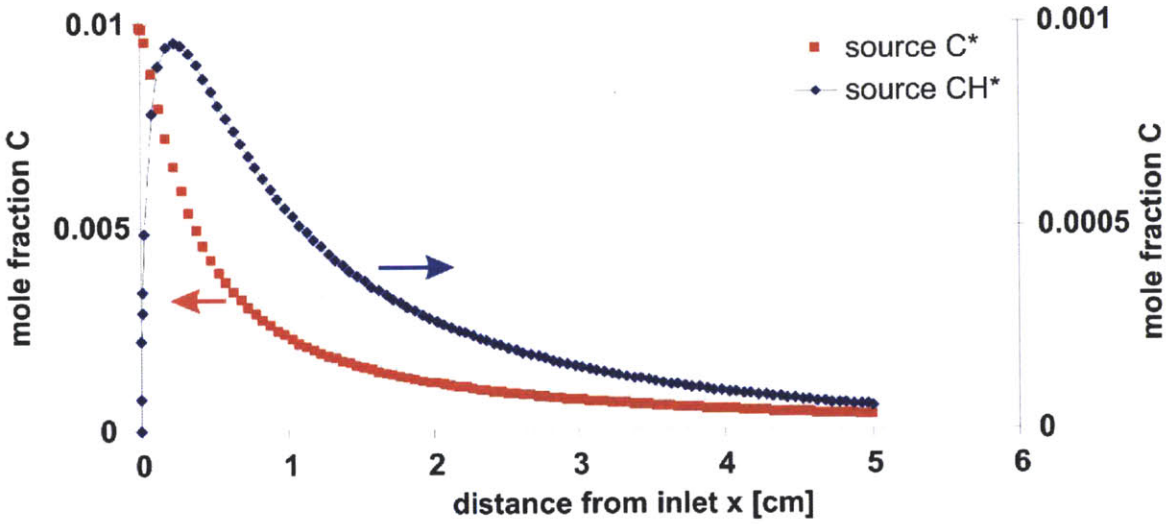

Figure 34 CHEMKIN simulation of C radical concentration profile in reactor for different radical sources

The simulation results emphasize that more information about the details of the surface reaction on the promoter are necessary to have quantitative agreement with our experiments.

The good qualitative agreement between the predicted carbon radical concentration and the continuity of graphene validates the model of "distributed catalysis" where the promoter dehydrogenates methane and the Cu substrate incorporates the radicals into the graphene lattice. Following this model, the list of potential growth substrates can be increased to materials that do not have the ability to decompose methane but still facilitate the formation of the graphene structure.

4.6 Comparison of promoters

Now, the effect of different promoters on the growth of graphene will be studied under optimal growth conditions for each promoter. Since the efficiency of the catalytic decomposition of methane is sensitively dependent on the catalyst used, the ratio of methane and hydrogen partial pressures had to be adjusted. To compare the different growth results, the data in Figure 35(a) was rescaled by the exposure to methane, which is calculated as the methane partial pressure × the exposure time. Figure 35 shows the evolution of θ with methane exposure with and without the use of promoters.

When focusing on the high exposure regions it can be seen that the addition of either Mo and Ni promoters can increase the maximum θ to ~90%. This value is thought to represent full graphene coverage in the presence of surface impurities under our growth conditions. The observed maximum θ was found to be increased by pre-treatment of the copper substrate as described previously.

A high maximum coverage at large exposure is also achieved when reproducing a strategy used by Li et al.[33] that employs a higher pressure CVD step. The success of the high pressure growth can be explained by results obtained by Becker et al.[70] who found that an increase of methane partial pressure at high temperatures will result in an exponential increase in auto-catalytically generated carbon radicals. Thus, methane itself can act as the catalyst instead of the copper substrate.

Several observations can be made when studying the low methane exposure region of Figure 35(a): It is found that, when using molybdenum as a promoter, no graphene growth is observed on the Cu substrate during the initial 25kPasec exposure. This induction period was previously observed for molybdenum promoters in methane

reforming[71] and attributed to the reaction of methane and molybdenum to form catalytically active molybdenum carbide. Indeed, Figure 36 shows a faceting of the Molybdenum promoter occurring for high exposures.

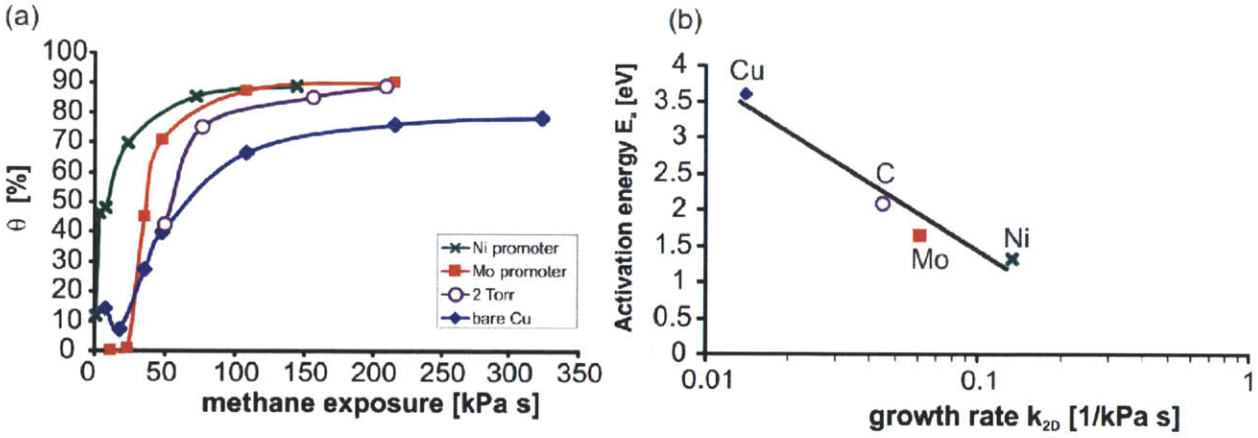

Figure 35 (a) θ vs. methane exposure for bare Copper, Molybdenum, Nickel promoters and higher pressure CVD growth (b) measured growth rate vs. theoretical activation energy barriers for methane dehydrogenation over different catalysts

We furthermore find that the different materials require different exposures to reach the maximum coverage which means that the growth rate of graphene on copper is affected by the choice of promoters. This observation can be understood when considering the details of the distributed catalysis. The formation of graphene is a two-step process. First the dehydrogenation of methane into carbon radicals occurs on the promoter. Then, these radicals are incorporated into the graphene lattice on the Cu substrate. Both steps have different energy barriers that limit their rates. Wu et al. [72] calculated that the graphene formation through addition of carbon atoms on a copper surface has a barrier height of 1.01eV. This barrier is lower than the dehydrogenation of methane on any of the investigated catalysts and thus is not the rate limiting step. Methane decomposition on

Nickel (111) surfaces has the lowest activation energy (1.32eV[64]) and should proceed faster than on Mo (1.64eV[71]). The decomposition on Copper (100) facets is energetically very unfavorable (3.6eV[63]) and graphene growth on bare Cu in the absence of a promoter will thus be the slowest.

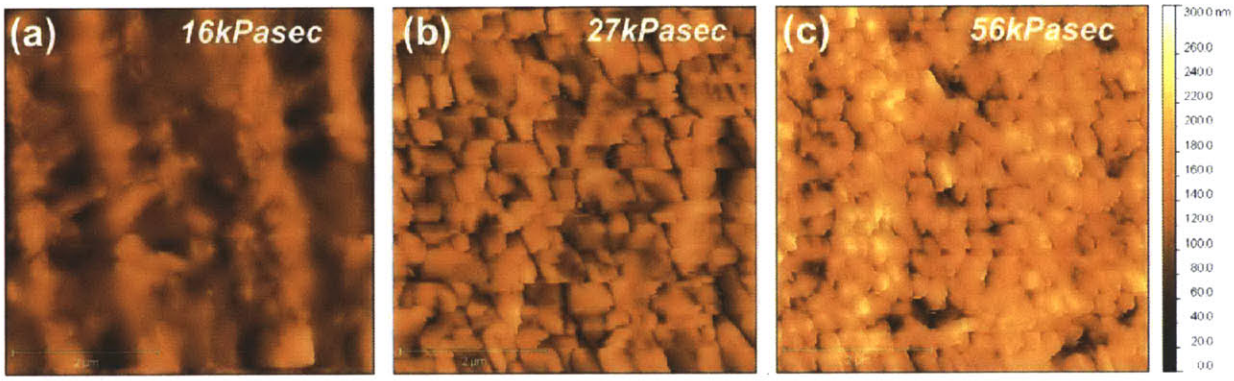

Figure 36 Morphology of the Mo promoter at different methane exposures

To quantify this model, the different activation energy barriers E_a can be related to the growth rate of a two dimensional sheet k_{2D} through an Arrhenius equation

$k_{2D} = Ae^{-E_a/2kT}$, where A is a proportionality constant and T is the growth temperature

The growth rate can be extracted from the data in Figure 35 by fitting $\theta(t)$ to the function

$\theta(t) = \theta_{max}(1 - e^{(-k_{2D}(t-t_0))})$, where θ_{max} is a parameter dependent on the growth substrate and growth process, t_0 is the previously described induction period, and k_{2D} is the growth rate at a certain methane pressure. (For short growth times, this function converges to the previously used constant growth rate $\theta(t) \approx \theta_{max} k_{2D}(t - t_0)$).

In Figure 35(b) the correlation between the measured growth rate and the theoretically predicted activation energies for methane decomposition are plotted on a semi-logarithmic scale. It can be seen that they follow an Arrhenius-type behavior as expected. Thus, a low activation energy for the methane decomposition is desirable for a high growth rate, and many additional promoters could be selected based on this criterion, i.e. Ru (E_a=1.12eV), Pd (E_a=0.79eV) or Pt (E_a=1.2eV)[65].

Interestingly, the growth rate of the two step CVD process over copper agrees well with the predicted energy barrier for methane decomposition using activated carbon as a catalyst[73]. This supports the hypothesis that the autocatalytic conversion of methane into graphene is an alternative to its catalytic decomposition over Cu. Thus, graphene growth on copper would only be self-limited at low methane pressure, when no autocatalytic production of carbon radicals occurs.

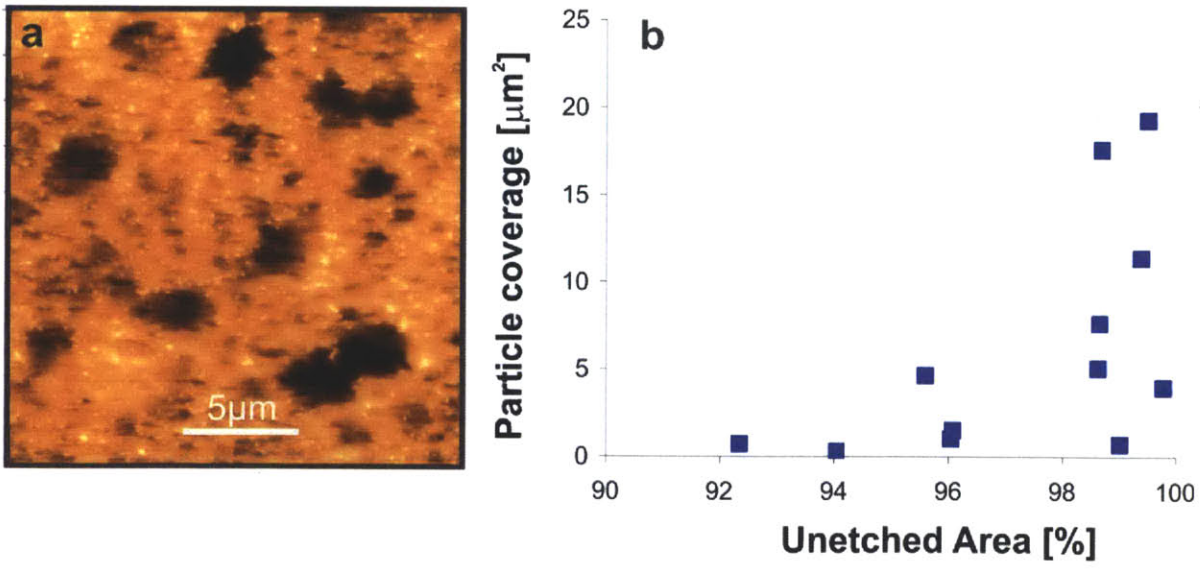

Figure 37 (a) Morphology of graphene on copper for high methane exposure and Mo promoter (bright spots indicate amorphous carbon particles, dark regions are etch pits), (b) correlation between occurrence of etch pits and amorphous carbon particles

At higher methane partial pressure, carbon radicals are being supplied even after complete graphene coverage is achieved. This behavior was observed when using promoters at very high methane exposure which results in the formation of amorphous carbon particles on the graphene film (Figure 37(a)). The correlation between the occurrence of etch pits and amorphous carbon particles in Figure 37(b) indicates that amorphous carbon only occurs for almost continuous graphene sheets and that more particles appear the higher the graphene coverage. This observation suggests that particles are indeed forming when the film is almost complete.

This observation suggests that optimization of the carbon radical concentration could be a viable route to growing multiple graphene layers on Cu and could explain the production of bilayer graphene under higher methane pressure conditions [16].

5. Direct CVD synthesis of patterned graphene via catalyst passivation

There are a variety of novel applications that exploit the extraordinary properties of graphene. Its flexibility, metallic conduction, and high current carrying ability, for example, make it well suited as interconnects[74]. There are already applications, such as touch screens and transparent electrodes[75], that incorporate CVD grown graphene and which are close to commercial realization. The need to pattern graphene, however, is a challenge in the large scale application of graphene in more complex devices, such as memory devices[76] or graphene interconnects in flexible circuits[77], displays[78], etc..

5.1 Prior art

Currently the fabrication of graphene patterns involves processes from three categories[79]:

- A mask can be generated on top of graphene through lithographical patterning of a photoresist that protects certain areas of graphene from a subsequent destructive patterning step.
- Excess graphene can be directly destroyed through direct writing, i.e. with lasers[80] or ion beams[81].
- Graphene can simultaneously be patterned and transferred to a target substrate by transfer printing[82].

These methods suffer from a mixture of disadvantages such as lacking scalability, constraints on the target substrate or fabrication speed.

Additionally, traditional patterning techniques rely on the destructive removal of excess graphene through use of oxygen plasma, UV ozone, RIE, etc. These techniques can decrease the quality of the graphene and leave rough graphene edges[83]. Furthermore, the

material deposition and lift off steps necessary to define graphene patterns have been shown to affect the doping of the graphene film and the graphene-electrode-interface, thus deteriorating the performance of the fabricated devices[84].

An alternative approach to the post-synthesis-patterning is the direct synthesis of patterned graphene by CVD. This method could potentially produce higher quality graphene devices since the patterning step is carried out before the graphene is synthesized and the risk of contaminating the graphene is minimized. Some attempts have been made to obtain patterned graphene by depositing catalytic substrates in the desired shape and then growing graphene on these substrates[17, 85-86]. However, there is a fundamental limitation to the achievable resolution because the patterned catalyst will restructure itself at the necessary high process temperatures to decrease its surface free energy, resulting in smoothed-out corners and merged features. Furthermore, the deposition of patterns through evaporation increases the production cost compared to rolled foils and such depositions can result in lower crystalline quality substrates which correlates with lower quality graphene[87].

We here describe a technique that can generate patterned graphene through area-selective CVD growth. The method relies on the passivation of defined areas of catalyst material and the subsequent selective growth of graphene in the unpassivated regions.

The described technique is demonstrated to have the potential for both the production of high quality samples, large area patterns, and low cost graphene-based devices for a multitude of different applications which could improve the commercial potential of graphene.

5.2 Experimental results

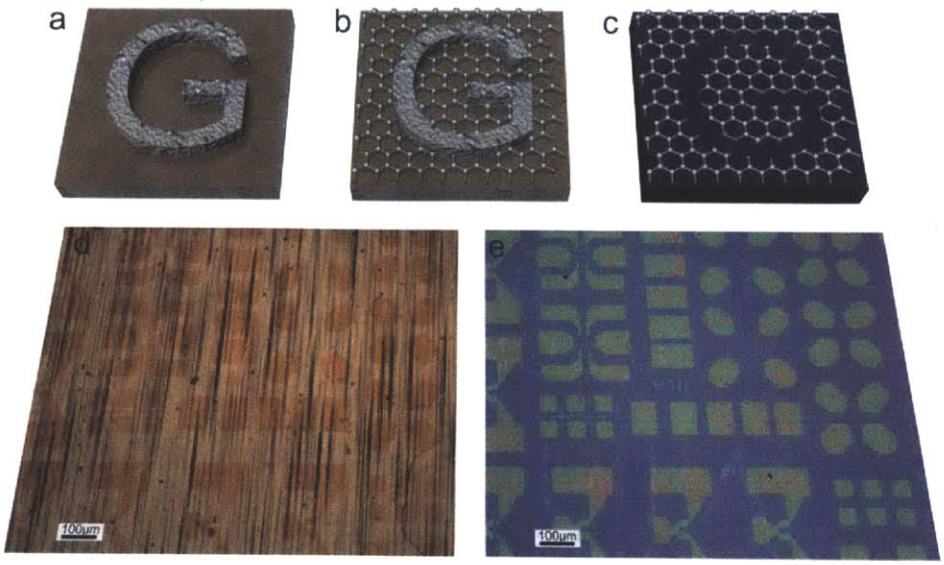

Figure 38 (a-d) Representation of the procedure that results in patterned graphene (a) deposition of passivation layer, (b) area selective growth of graphene, (c) transfer onto target substrate (d) optical micrographs of copper foil after deposition of Al2O3 patterns, (e) patterned graphene on Si/SiO2 target substrate

Figure 1 outlines the process to synthesize graphene patterns: First, a passivation layer is deposited in a negative pattern onto the growth substrate (Fig 1(a)). This material has to prevent the catalytic production of graphene by suppressing the formation of a graphene sheet. The passivation effect will result in the selective synthesis of graphene only in areas where the growth substrate is exposed (Fig 1(b)). After a transfer step of graphene from the copper substrate, the patterned graphene can be placed onto arbitrary substrates (Fig 1(c)). A wet chemical etching step can be included into the transfer step to remove the passivation layer if necessary.

Materials for the passivation layer have to fulfill several requirements, such as immiscibility with the Cu substrate at high temperatures, a high melting point, etc. More restrictive is the constraint that the passivation material has to inhibit the formation of graphene in certain areas while not hindering the graphene growth in neighboring exposed regions.

In this chapter, aluminum oxide (Al_2O_3) was chosen as a passivation layer for graphene growth on Cu substrate because of several desirable properties of Al_2O_3: The refractory nature of alumina prevents it from interacting with the growth substrate and inhibits reshaping of the passivation layer under high temperature. Furthermore, its easy production and low cost make it attractive for large scale industrial applications.

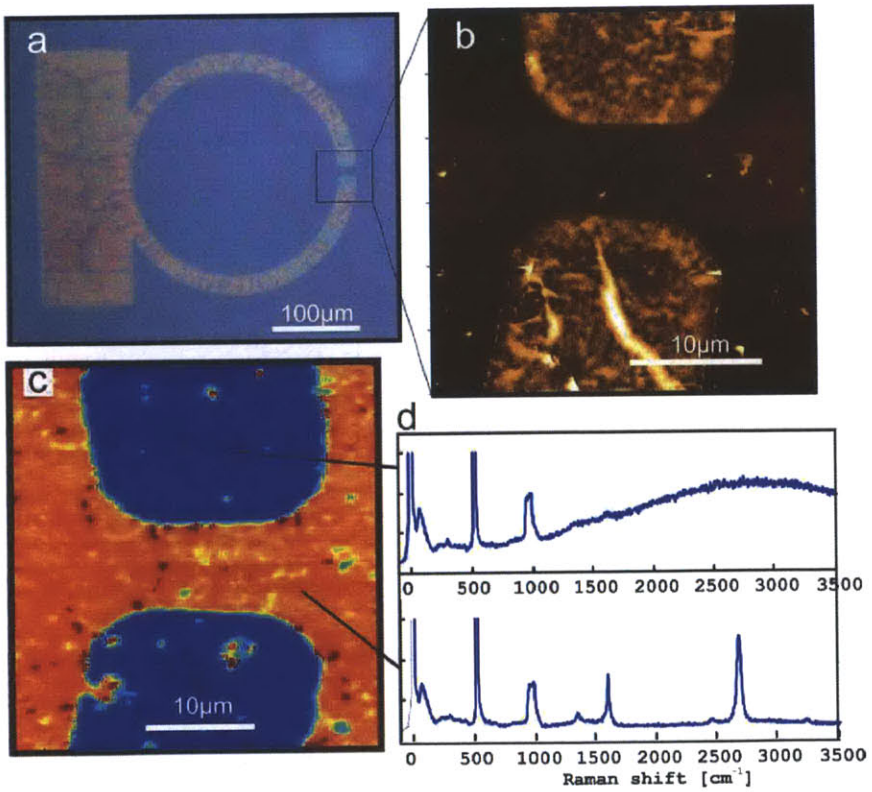

Figure 39 (a) Optical micrograph of patterned graphene after transfer to SiO_2 substrate, b) magnified AFM image of structure, c) Raman map of the G'-band intensity of the same region, d) representative Raman spectra of passivated region (top) and exposed region (bottom)

Based on the above presented process, graphene patterns were generated through lithographical patterning of photoresist on the Cu foil and subsequent deposition of Al_2O_3 via ALD. The chemical properties of the passivation layer were investigated after annealing and Figure 40 shows an XPS spectrum of the Al 2p peak region. The absence of a peak at 73.7eV indicates that no metallic aluminum is present. The good fit of the main feature to one symmetric peak indicates that no undercoordinated Aluminum is in the oxide and that the alumina is indeed Al_2O_3. The small side peak at 77.3eV is identified as the 3p peak of copper oxide originating from the oxidized substrate.

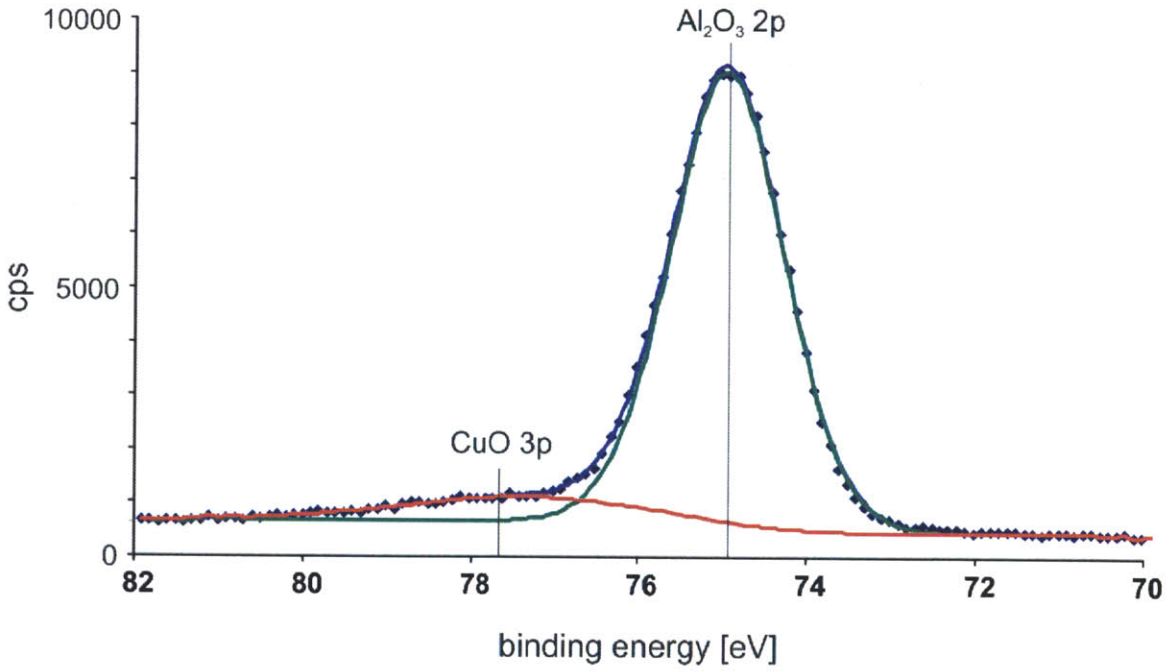

Figure 40 XPS spectrum of the deposited passivation layer after graphene growth with indication of the position of metallic aluminum and identification of the occurring peaks

Wet chemical removal of the alumina passivation layer during transfer proved difficult, which was attributed to the transformation of amorphous Al_2O_3 into crystalline Al_2O_3 under the growth conditions[88]. Variation of the growth process or etching procedure is expected to overcome this issue. The presence of the passivation layer, however, was not

detrimental to the experiments but, in fact, proved useful for alignment of the patterned graphene on the target substrate. The beneficial effect of a crystalline alumina dielectric on graphene device performance has recently been predicted[89] and there are other applications where a thin, high quality dielectric layer could also prove useful, i.e. as spacers in LCDs.

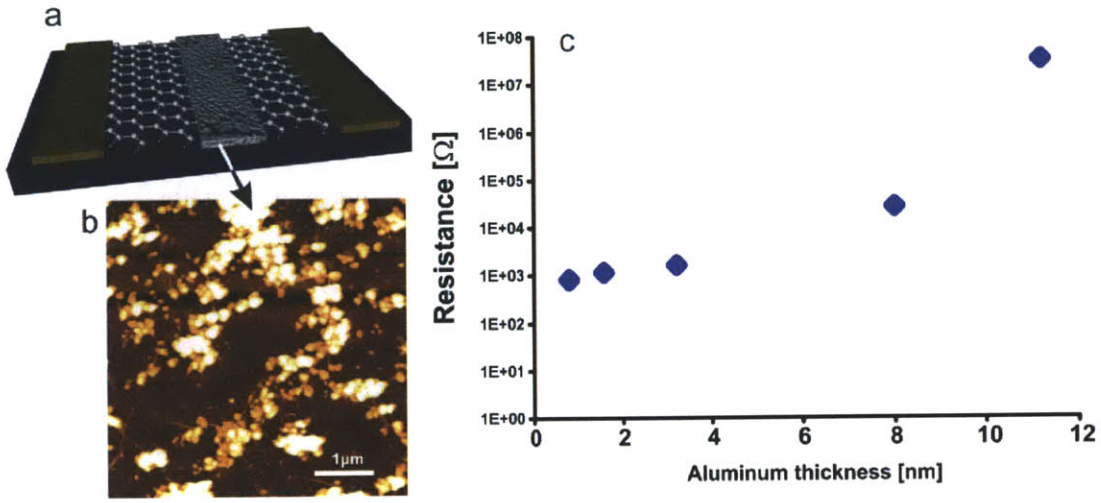

Figure 41 (a) Schematic of a device with an Al_2O_3-constricted graphene channel, (b) AFM image of the channel, (c) Resistance of devices as a function of Al_2O_3 thickness in the graphene channel

5.3 Applications in functional devices

The presence of the passivation material does not necessarily have a detrimental effect on the graphene based device. Figure 41 demonstrates a device where the passivation layer adds functionality to the graphene based device. The graphene channel is constricted by alumina particles formed by atomic layer deposition, as demonstrated in Figure 41(b). The transport of carriers is hindered by this constriction and the resistance of the device is thus sensitively dependent on the amount of alumina in the channel. By carefully tuning the Al_2O_3 thickness through ALD deposition, the resistance of the graphene/Al_2O_3 hybrid

device is tunable over 5 orders of magnitude as demonstrated in Figure 41(c). This behavior can allow the direct integration of resistive elements in graphene circuits during growth.

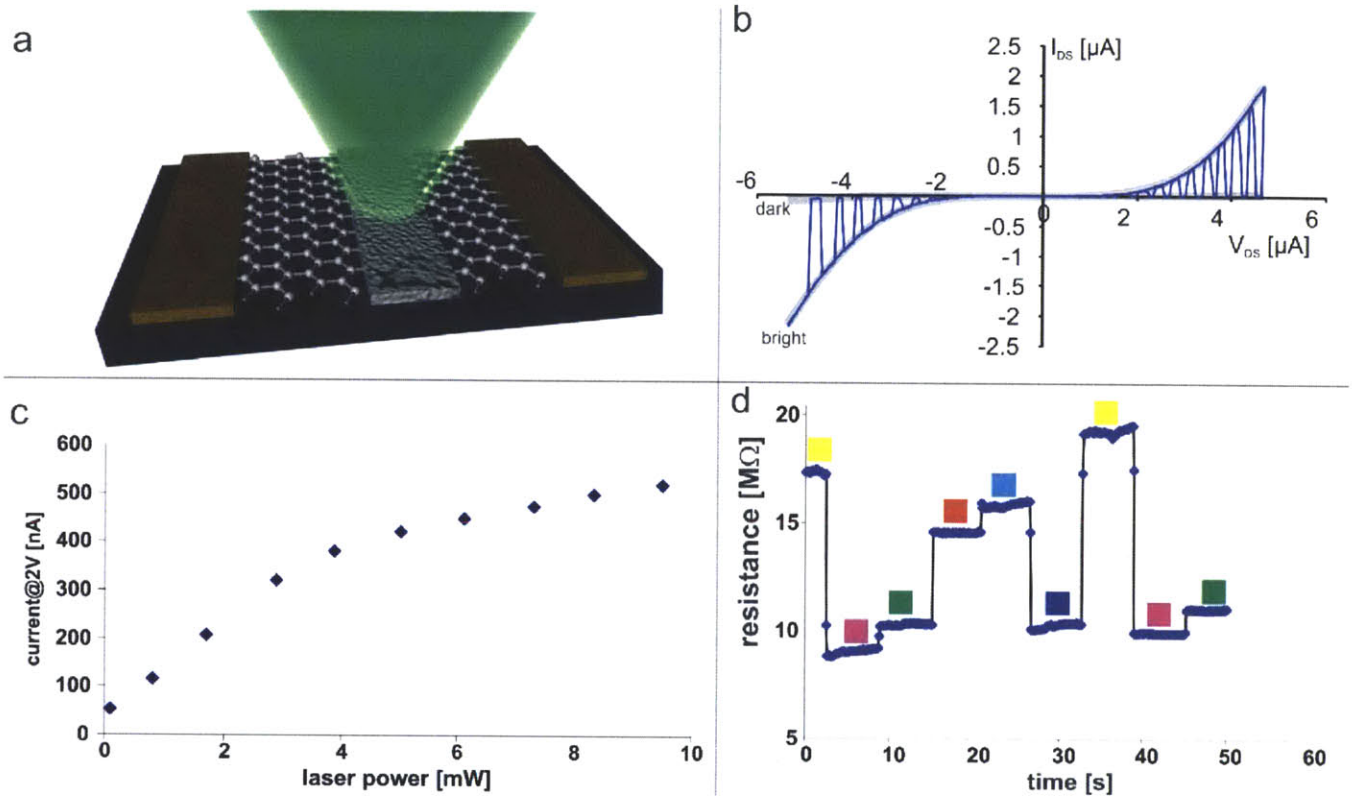

Figure 42 Photosensitive graphene/Al_2O_3 device under laser irradiation, (a) schematic of device, (b) I-V curve under pulsed illumination, (c) current of device under 532nm illumination of varying power, (c) photoresponse of device to LCD screen displaying different colors.

A surprising discovery is the photosensitivity of such a graphene/Al_2O_3 hybrid device as shown in Figure 42. As the hybrid structure was accidentally illuminated, a significantly higher current was observed compared to the dark condition at the same bias (Figure 42(b)). The current was found to be sensitively dependent on the power of the illumination and Figure 42(c) shows the photoresponse for 532nm excitation. This

resistance variation by one order of magnitude cannot be observed when illuminating a pure graphene device. We thus hypothesize that the presence of aluminum oxide creates a photo response by injecting photocarriers into the graphene. The system has shown high photosensitivity and was used to detect colors. Figure 42(d) shows the response of the device to colors displayed on an LCD screen and the reliable distinction between different colors is demonstrated. More detailed studies have to reveal the mechanism of carrier generation in the graphene/Al_2O_3 hybrid structure. Applications as large scale, flexible, cheap, transparent photo sensors, cameras, etc. can be envisioned.

5.4 Analysis of graphene patterns

The patterned graphene was then transferred onto a Si/SiO_2 substrate and an optical micrograph is shown in Figure 39(a). The clear boundaries found by atomic force microscopy in Figure 39(b) indicate the potential for high resolution patterns.

The presence and quality of graphene was analyzed by Raman spectroscopy. A map was obtained by taking one Raman spectrum every 100x100nm and Figure 39(c) shows the spatial variation of the G'-band peak intensity in a region where graphene surrounds a passivated area. The G'-band feature at ~2650$cm^{-1}$is enhanced in graphene because of a double resonance process and can be considered a characteristic feature of graphene[22]. The passivation layer pattern is clearly distinguishable by the absence of a G'-band feature as well as other Raman peaks that would occur for graphitic materials (Figure 39(d)). The background in the Al_2O_3 Raman spectrum is assumed to originate from defect-induced photoluminescence of the material[90], and the weak G-band (~1600cm^{-1}) is attributed to amorphous carbon contamination.

The high quality of the graphene grown in the unpassivated areas can be inferred from the sharp Raman peaks and the low intensity of the defect induced D-band Raman feature. The D-band intensity was found to increase during a transfer-related annealing step and thus does not only reflect the intrinsic defect density.

Hall measurements in the van-der-Pauw geometry were performed to characterize the electronic mobility of the graphene films and a value of 650cm^2/Vs was obtained, that is comparable to other CVD graphene films grown with the same CVD procedure.

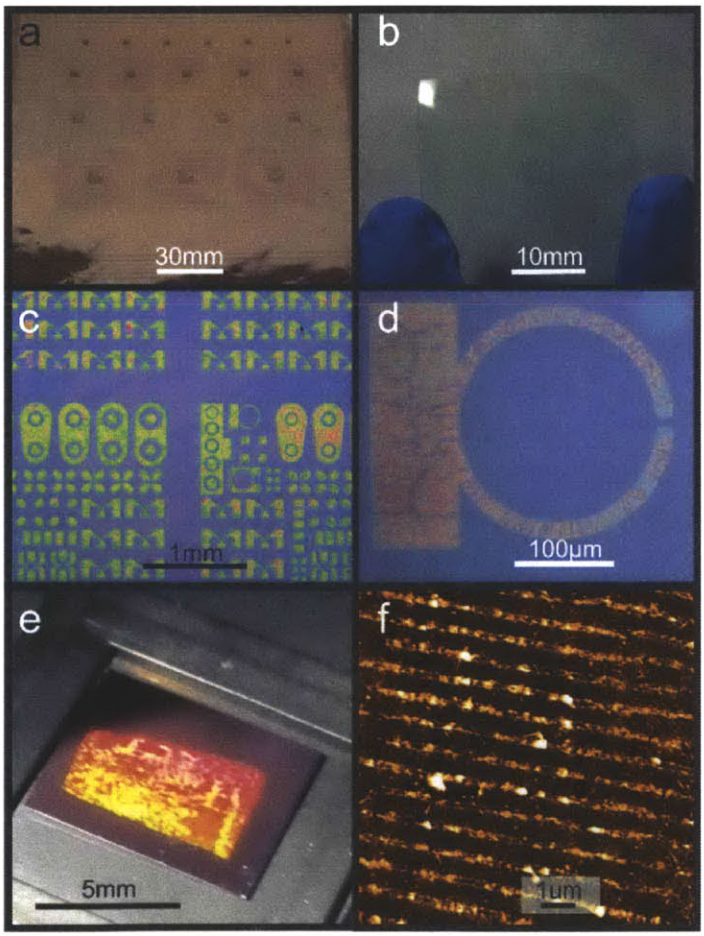

Figure 43 Resulting structures for different deposition techniques (a) photograph of large scale patterns deposited by ink-jet printing on copper foil, (b) patterned graphene film after transfer to plastic substrate, (c) optical micrograph of graphene patterns obtained by photolithographical patterning of the passivation layer, (d) high magnification image of (c), (e) photograph of graphene

sample patterned by micro contact lithographical deposition of a passivation layer, (f) AFM image of the resulting parallel Al_2O_3 lines with a 700nm period

5.5 Deposition methods

Various methods to deposit the passivation layer can be conceived to accommodate various demands of different applications such as high resolution, low cost, scalability, etc. and Figure 43 details several approaches.

Ink jet printing is a technique that has proven the ability to generate large areas of medium resolution patterns at low cost[91]. Figure 43(a) shows a large (150x250mm) piece of Cu foil that has been patterned by an ink-jet deposited $AlCl_3$ precursor. In contact with air, the deposited material will readily oxidize and form the passivation layer. After growth, the graphene was transferred onto a flexible PET substrate (Figure 43(b)) to demonstrate the feasibility of producing flexible, transparent graphene circuits at low cost. This method is envisioned to allow the production of graphene-based recyclable electronics, i.e. for Radio-frequency identification (RFID) tags.

Micrometer and nanometer sized graphene devices have proven their potential for high frequency electronics[92], photodetectors[93], etc. Figure 43(d) shows the result of graphene growth on a high resolution prepatterned sample obtained by photolithography and subsequent atomic layer deposition of aluminum oxide. The feature size seems limited only by the resolution of the lithographical patterns. The transition region between the passivation layer and the graphene was investigated by Raman spectroscopy (Figure 44). It was found that the sharpness of the transition exceeded the resolution of the measurement system and the finite slope observed was caused by the Gaussian beam shape of the micro-Raman tool.

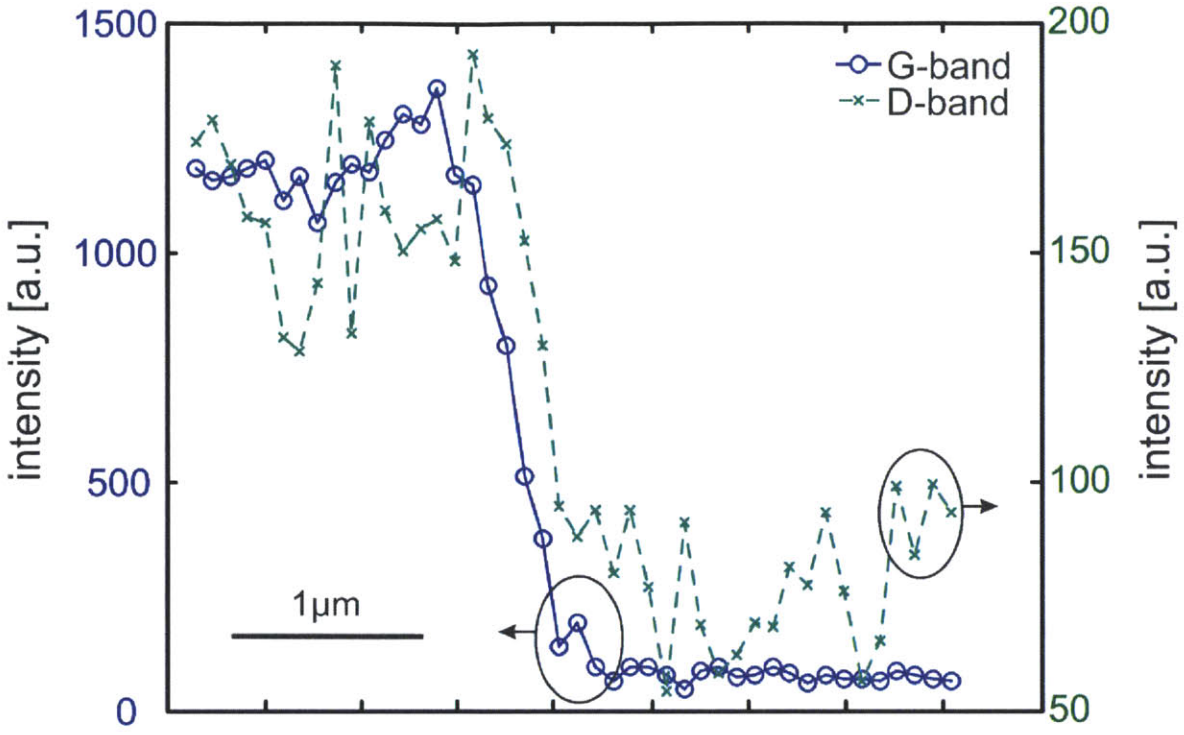

Figure 44 Raman G-band (o) and D-band (x) peak intensities of transition region between graphene (right) and passivation layer (left)

The absence of an increased Raman D-band intensity in the transition region (Figure 44) suggests that higher quality edges are formed compared to those formed with traditional lithographical approaches[94]. This property would be promising for improving the electrical performance of nanoribbon-based devices.

Finally, novel methods of depositing Al_2O_3 over large areas at high resolution are available, and microcontact printing[95] is presented as such a technique in Figure 43(e). A Polydimethylsiloxane (PDMS) replica of a grating with 700nm pitch was inked with a solution of $AlCl_3$ and then pressed onto Cu-foil. This procedure resulted in the fabrication of parallel lines of alumina that were used to grow arrays of graphene ribbons over large areas, as observed by a diffraction effect of the resulting sample (Figure 43(e)). Atomic

force microscopy in Figure 43(f) reveals that these ribbons have a width of approximately 300nm.

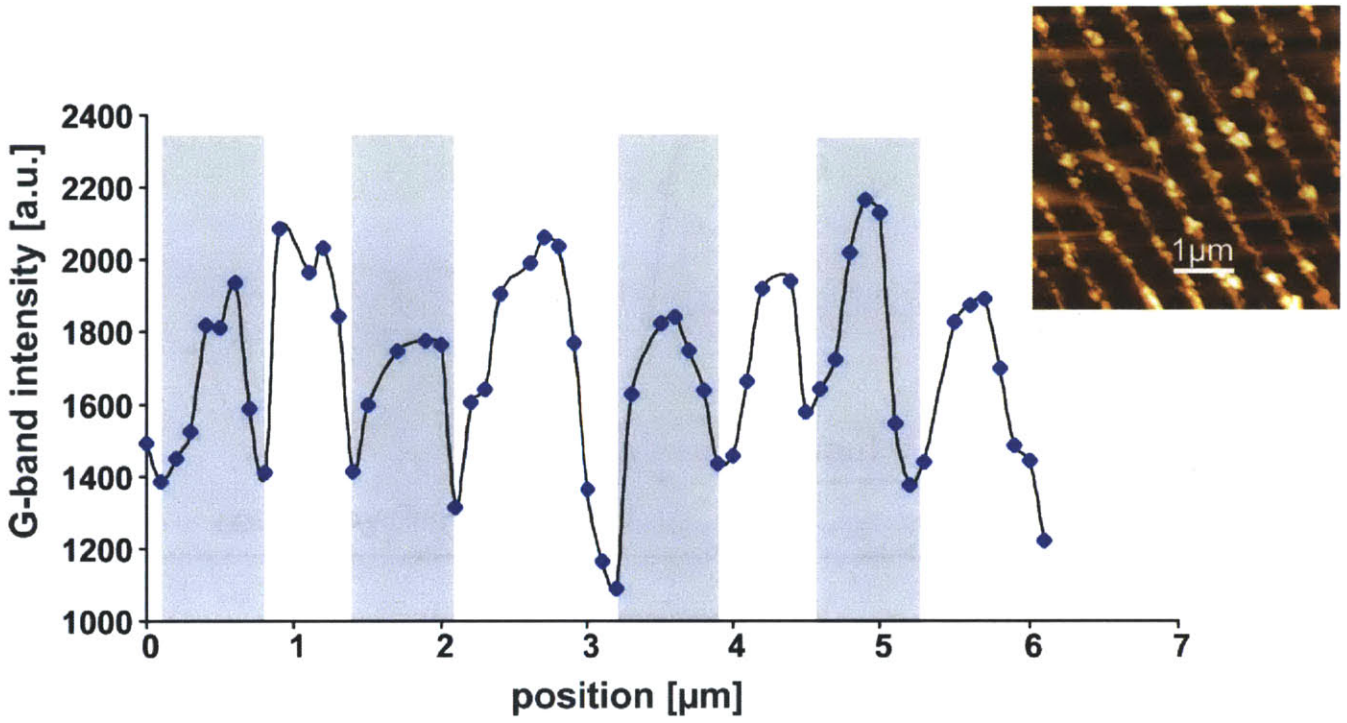

Figure 45 Raman G-band peak intensity varying periodically with 700nm pitch across parallel graphene ribbons prepatterned by micro-contact lithography, (inset) AFM image of the patterned sample

Since the periodicity of the graphene strips is smaller than the spot size of the micro-Raman tool, only undulations on a constant background are expected. Indeed, the spatial variation of the G-band intensity shown in Figure 45 exhibits periodic variations with a periodicity of 700nm. The minima in the intensity thus correspond to the position of the Al_2O_3 strips while the maxima are expected to be in the center of the graphene ribbons. These results suggest the possibility of generating high resolution, large scale graphene electronics for application in novel applications.

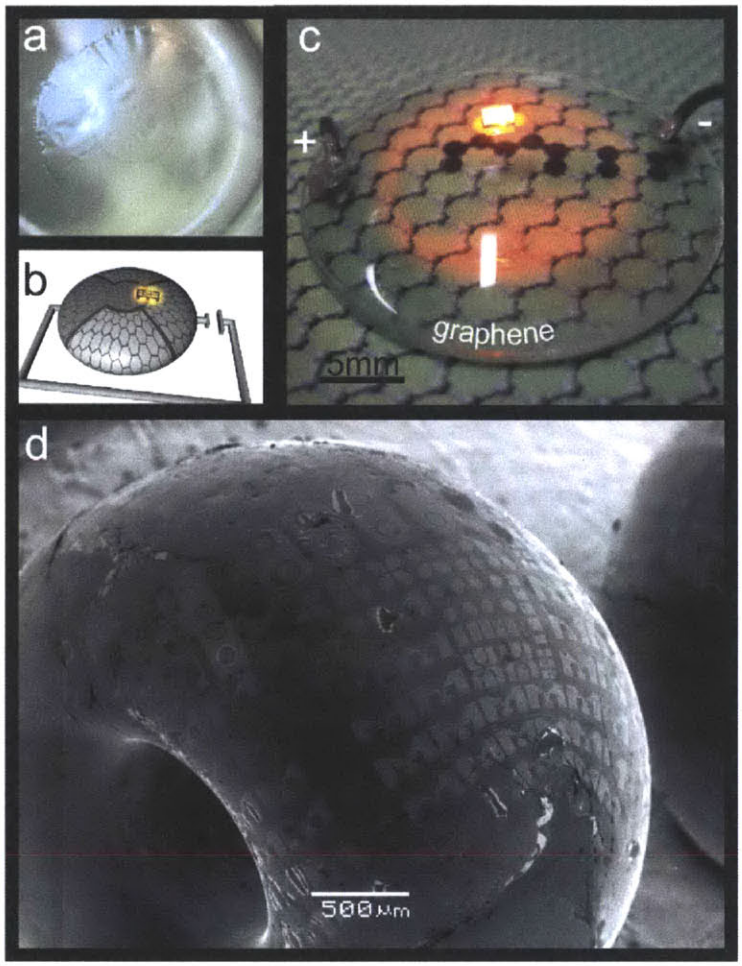

Figure 46 Transfer of patterned graphene onto complex shaped objects. a) photograph of patterned graphene membrane during transfer, b) schematic of graphene electrode structure, c) photograph of patterned graphene electrodes on a lens supplying current to a LED, d) SEM image of lithographically patterned graphene transferred onto a glass bead

5.6 Graphene based devices on complex surfaces

For traditional lithographic techniques there are limitations imposed on the substrate by processing requirements. One of the most fundamental restrictions that conventional photolithography is facing is flatness: Due to a limited depth of focus of the optical exposure units, handling issues, etc., non-planar substrates are not accessible for high resolution lithographical patterning.

Graphene is a suitable material for non-planar devices that could prove useful in fields such as novel detectors[96], implantable devices[97] or displays[77], because of its atomic thickness and its ability to conform perfectly to rough surfaces.

The ability of transferring prepatterned graphene films onto complex surfaces is demonstrated in Figure 4. As a proof of concept a pattern with 4 clover-leaf-shaped electrodes (Fig 4(a)) was fabricated on the Cu-foil. This structure was then grown and transferred onto a glass lens to act as electrodes for a simple electrical circuit (Fig 4(b)). Current is directed through a standard light emitting diode (VISHAY-TLMO1000,1.6x0.8mm) that was attached onto the graphene layer by silver adhesive (Figure 46(c)). This integration of commercially available electronics components into graphene circuits is intended to show their synergy.

As a second example, lithographically prepatterned graphene was transferred onto a 3mm glass bead. In the Scanning Electron Microscope (SEM) image in Figure 46(d), graphene can be identified by transfer-induced tears in the continuous film. The passivation layer thickness was chosen to be small enough (7nm) to also conform to the spherical surface. This ability to produce micron-sized graphene structures and dielectrics on complex surfaces opens up new ways to produce electronics for a variety of applications, such as implantable devices, bio-inspired circuits, etc.

We furthermore present a proof-of-concept lighting system based on graphene. Two graphene sheets grown by CVD act as electrodes for an electroluminescent structure as indicated in Figure 47. This device was fabricated because of its high light emitting efficiency, easy fabrication and mechanical flexibility. The structure emits light when an AC voltage is applied to a sandwich structure as presented in Figure 47(a).

The dielectric layer prevents direct current flow between the electrodes and light is generated by radiative recombination of trapped holes with electrons that were introduced to the phosphor during two different charging cycles. The intimate contact of the layers is important since the amount of current at a given voltage is determined by the capacitance of the structure. Graphene allows the simple fabrication of such a device because of its ability to conform to a surface. To produce the stack economically the graphene transfer process had to be simplified. Instead of transferring a graphene layer, removing the PMMA support membrane and then depositing another polymer layer, the functional layers were incorporated into the transfer process.

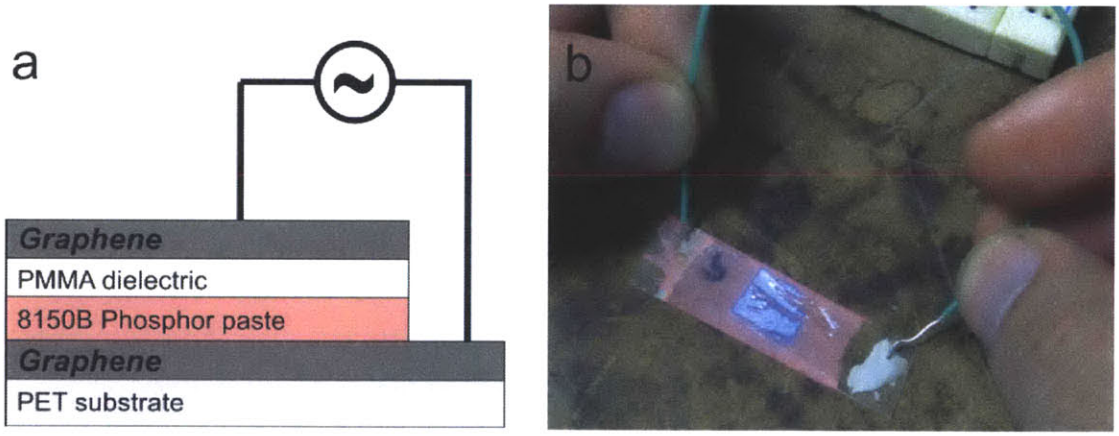

Figure 47 (a) Structure of a electroluminescent device with graphene electrodes, (b) working light emitting device

The electroluminescent phosphor (Dupont Luxprint 8150B) turned out to be stable in aqueous and acidic environments and could thus be exposed to the transfer process. The fabrication procedure was the following:

1. Graphene was grown on Cu foil
2. Dupont Phosphor was spread on the graphene

3. The Cu foil was removed by immersion into CE-100 copper etchant.
4. The sample was transferred onto a piece of plastic foil.
5. PMMA was spin coated onto a second piece of graphene on Cu foil
6. Cu foil of this sample was removed
7. The PMMA/graphene membrane was transferred bottom-up onto the same PET foil
8. Electrical contact to both graphene sheets was made by silver adhesive (EMS 478SS)

Figure 47 (b) demonstrates the emission of the electroluminescent device in the regions where the two graphene electrodes overlap. Delamination of the upper electrode from the stack proved to be challenging and limited the contact area. This problem is expected to be solved by an encapsulation step that is normally included in fabrication of such devices.

More work has to be done to combine the patterned graphene electrodes with the process to generate electroluminescent emitters to demonstrate the use of graphene in flexible matrix-displays.

6. Conclusions

The previous chapters have attempted to advance several aspects of the research on graphene.

First, we have demonstrated the use of graphene passivated etching as a method to reveal the defectiveness of graphene. Etchant cannot attack substrate regions that are protected by graphene and thus the resulting etch pattern allows inference on the density and position of structural defects. The strong correlation between the graphene defectiveness and the maximum mobility emphasizes the importance of controlling these structural defects. The good sensitivity of the new tool to small defects was shown and the easy availability of this technique make it a facile and scalable metrology tool that could be used for graphene synthesis optimization in the future.

The structural defects revealed by this graphene passivated etching technique were then studied in more detail. Through size-selective passivation of the structural defects by atomic layer deposition the size of the defects could be deduced. The nanometer sized openings were found to allow extremely fast permeation speeds in the order of meters per second which makes them promising materials for nanofluidic devices.

The structural defects were found to be caused by nanoparticles on the Cu substrate. Pretreatment of the Cu substrate was shown to result in higher quality graphene.

Finally, we have investigated the growth of graphene by CVD through graphene passivated etching. A decrease in growth rate for partially covered graphene samples was found, which can be explained by the effect of catalyst deactivation. The growth rate was found to be limited by the catalytic dehydrogenation reaction of methane and could be increased through a promoter. This effect was explained by the increased concentration

of carbon radicals generated by the promoter. Due to these advantages the use of a promoter should be considered for future applications.

The knowledge gained from the previous studies was applied and a new approach to generating graphene patterns is presented. By passivating the catalyst, graphene growth could be restricted to certain areas. The achievable high resolution and high quality of the grown graphene are promising for electronic applications. Several approaches to depositing a patterned passivation layer that could be used in complementary applications were demonstrated. Finally, the deposition of prepatterned graphene onto non-planar substrates was shown and the ability to generate high resolution graphene patterns on complex surfaces opens up novel application areas for graphene-based electronic devices.

6.1 Future work

To achieve the ambitious goal of developing new graphene enabled electronic devices the following growth-related issues still have to be overcome:

- The transfer process has to be made more reliable and reproducible. The sample to sample variation introduced by handling the copper substrate and the membrane is currently a large factor in the inability to control the sample quality. Furthermore, more studies have to be carried out to identify changes made to the graphene material during the transfer process in terms of doping, introduction of defects, etc.

- The lowering of the growth temperature could have benefits for the compatibility with other materials and processes and could also decrease the impact of cooling induced wrinkling on the morphology of graphene.
- The growth on dielectric substrates would resolve many problems associated with metallic growth substrates, such as the need for a transfer step, large thermal mismatch between substrate and graphene, etc.
- Better control of both the formation and the extension of additional layers on the graphene through substrate engineering is crucial.

For the application of graphene following the presented work, several approaches could be envisioned.

- More complex circuits on flexible substrates or complex surfaces should be designed. For example, a display could be produced by using commercially available electroluminescent or electrochromic materials in a sandwich structure between graphene layers.
- The resolution limits of the passivated growth technique should be explored to identify whether high quality nanostructures could be synthesized.
- Other passivation materials could be explored for the described area-selective CVD process that can be more easily etched.

6.2 Outlook

A proper ending of this thesis should be the attempt to extrapolate the future of graphene based on its history, the lessons learned from other carbon materials and our hopes and ideas. One issue that graphene has to overcome to be successful is the way in which it is used. Currently, significant effort is invested to make graphene competitive against mature technologies in areas that were specifically designed with those materials in mind.

Applying graphene as transparent conductors in glass based solar cells, for example, is commercially challenging because it is competing with technologies that have similar performance but can be seamlessly integrated into the production process of the glass covers. The implementation of an untested technology because of marginally better performance will be commercially unfeasible.

Instead, its high transparency and conductivity in combination with mechanical strength and flexibility make it well suited for use in wearable electronics. This new market will require investment into research and development and no mature competitor exists.

It is thus strongly desirable to not pit graphene against other materials in existing fields but instead open up new areas that yet have to be conceived.

- Graphene is the ultimately thinnest material and reliable growth of a determined number of layers presents nanotechnology at its limits. This capability could be exploited to finely control spacing and produce channels, gaps or features with atomic precision on a macroscopic scale.
- Folds in graphene present a completely novel structure for electronic devices.

- Despite its thickness, graphene is mechanically very stable and the combination of those properties into nano-electro-mechanical devices could open up new concepts for electronic devices.

The strength of graphene is the appeal to researchers in a wide variety of fields. The research presented in this thesis represents work on only a small selection of topics that graphene research is currently studying and I am curious to see what the future will bring for graphene.

7. References

1. Geim, A. K.; Novoselov, K. S.; Morozov, S. V.; Jiang, D.; Zhang, Y.; Dubonos, S. V.; Grigorieva, I. V.; Firsov, A. A., Electric field effect in atomically thin carbon films. *Science* **2004,** *306* (5696), 666-669.
2. Schafhaeutl, C., Ueber die Verbindungen des Kohlenstoffes mit Silicium, Eisen und anderen Metallen, welche die verschiedenen Gallungen von Roheisen, Stahl und Schmiedeeisen bilden. *Journal für Praktische Chemie* **1840,** *21* (1), 129-157.
3. Brodie, B. C., On the Atomic Weight of Graphite. *Philosophical Transactions of the Royal Society of London* **1859,** *149* (ArticleType: research-article / Full publication date: 1859 / Copyright © 1859 The Royal Society), 249-259.
4. Hummers, W. S.; Offeman, R. E., Preparation of Graphitic Oxide. *J Am Chem Soc* **1958,** *80* (6), 1339-1339.
5. Boehm, H. P.; Clauss, A.; Hofmann, U.; Fischer, G. O., Dunnste Kohlenstoff-Folien. *Z Naturforsch Pt B* **1962,** *B 17* (3), 150-&.
6. Morgan, A. E.; Somorjai, G. A., Low Energy Electron Diffraction Studies of Gas Adsorption on Platinum (100) Single Crystal Surface. *Surf Sci* **1968,** *12* (3), 405-&.
7. Blakely, J. M.; Kim, J. S.; Potter, H. C., Segregation of Carbon to (100) Surface of Nickel. *J Appl Phys* **1970,** *41* (6), 2693-&.
8. Vanbommel, A. J.; Crombeen, J. E.; Vantooren, A., Leed and Auger-Electron Observations of Sic (0001) Surface. *Surf Sci* **1975,** *48* (2), 463-472.
9. Lu, X. K.; Yu, M. F.; Huang, H.; Ruoff, R. S., Tailoring graphite with the goal of achieving single sheets. *Nanotechnology* **1999,** *10* (3), 269-272.
10. Kroto, H. W.; Heath, J. R.; Obrien, S. C.; Curl, R. F.; Smalley, R. E., C-60 - Buckminsterfullerene. *Nature* **1985,** *318* (6042), 162-163.
11. Binnig, G.; Quate, C. F.; Gerber, C., Atomic Force Microscope. *Phys Rev Lett* **1986,** *56* (9), 930-933.
12. Choi, H.; Mody, C. C. M., The Long History of Molecular Electronics: Microelectronics Origins of Nanotechnology. *Soc Stud Sci* **2009,** *39* (1), 11-50.
13. Iijima, S., Helical Microtubules of Graphitic Carbon. *Nature* **1991,** *354* (6348), 56-58.
14. Fanton, M. A.; Robinson, J. A.; Puls, C.; Liu, Y.; Hollander, M. J.; Weiland, B. E.; Labella, M.; Trumbull, K.; Kasarda, R.; Howsare, C.; Stitt, J.; Snyder, D. W., Characterization of Graphene Films and Transistors Grown on Sapphire by Metal-Free Chemical Vapor Deposition. *Acs Nano* **2011.**
15. Li, X. S.; Cai, W. W.; An, J. H.; Kim, S.; Nah, J.; Yang, D. X.; Piner, R.; Velamakanni, A.; Jung, I.; Tutuc, E.; Banerjee, S. K.; Colombo, L.; Ruoff, R. S., Large-Area Synthesis of High-Quality and Uniform Graphene Films on Copper Foils. *Science* **2009,** *324* (5932), 1312-1314.
16. Bhaviripudi, S.; Jia, X. T.; Dresselhaus, M. S.; Kong, J., Role of Kinetic Factors in Chemical Vapor Deposition Synthesis of Uniform Large Area Graphene Using Copper Catalyst. *Nano Letters* **2010,** *10* (10), 4128-4133.

17. Reina, A.; Jia, X. T.; Ho, J.; Nezich, D.; Son, H. B.; Bulovic, V.; Dresselhaus, M. S.; Kong, J., Large Area, Few-Layer Graphene Films on Arbitrary Substrates by Chemical Vapor Deposition. *Nano Letters* **2009,** *9* (1), 30-35.
18. Puurunen, R. L., Surface chemistry of atomic layer deposition: A case study for the trimethylaluminum/water process. *J Appl Phys* **2005,** *97* (12).
19. Elliott, S. D.; Scarel, G.; Wiemer, C.; Fanciulli, M.; Pavia, G., Ozone-based atomic layer deposition of alumina from TMA: Growth, morphology, and reaction mechanism. *Chem Mater* **2006,** *18* (16), 3764-3773.
20. Blake, P.; Hill, E. W.; Neto, A. H. C.; Novoselov, K. S.; Jiang, D.; Yang, R.; Booth, T. J.; Geim, A. K., Making graphene visible. *Appl Phys Lett* **2007,** *91* (6).
21. Heath, J. R.; Xu, K.; Cao, P. G., Graphene Visualizes the First Water Adlayers on Mica at Ambient Conditions. *Science* **2010,** *329* (5996), 1188-1191.
22. Dresselhaus, M. S.; Jorio, A.; Hofmann, M.; Dresselhaus, G.; Saito, R., Perspectives on Carbon Nanotubes and Graphene Raman Spectroscopy. *Nano Letters* **2010,** *10* (3), 751-758.
23. Dresselhaus, M. S.; Saito, R.; Hofmann, M.; Dresselhaus, G.; Jorio, A., Raman spectroscopy of graphene and carbon nanotubes. *Adv Phys* **2011,** *60* (3), 413-550.
24. Ferrari, A. C.; Meyer, J. C.; Scardaci, V.; Casiraghi, C.; Lazzeri, M.; Mauri, F.; Piscanec, S.; Jiang, D.; Novoselov, K. S.; Roth, S.; Geim, A. K., Raman spectrum of graphene and graphene layers. *Physical Review Letters* **2006,** *97* (18).
25. Bunch, J. S.; Verbridge, S. S.; Alden, J. S.; van der Zande, A. M.; Parpia, J. M.; Craighead, H. G.; McEuen, P. L., Impermeable atomic membranes from graphene sheets. *Nano Letters* **2008,** *8* (8), 2458-2462.
26. Chen, J. H.; Cullen, W. G.; Jang, C.; Fuhrer, M. S.; Williams, E. D., Defect Scattering in Graphene. *Physical Review Letters* **2009,** *102* (23), -.
27. Ruiz-Vargas, C. S.; Zhuang, H. L.; Huang, P. Y.; van der Zande, A. M.; Garg, S.; McEuen, P. L.; Muller, D. A.; Hennig, R. G.; Park, J., Softened Elastic Response and Unzipping in Chemical Vapor Deposition Graphene Membranes. *Nano Letters*, null-null.
28. Huang, P. Y.; Ruiz-Vargas, C. S.; van der Zande, A. M.; Whitney, W. S.; Levendorf, M. P.; Kevek, J. W.; Garg, S.; Alden, J. S.; Hustedt, C. J.; Zhu, Y.; Park, J.; McEuen, P. L.; Muller, D. A., Grains and grain boundaries in single-layer graphene atomic patchwork quilts. *Nature 469* (7330), 389-392.
29. Cheng, Z.; Zhou, Q.; Wang, C.; Li, Q.; Wang, C.; Fang, Y., Toward Intrinsic Graphene Surfaces: A Systematic Study on Thermal Annealing and Wet-Chemical Treatment of SiO2-Supported Graphene Devices. *Nano Letters 11* (2), 767-771.
30. Chen, S.; Brown, L.; Levendorf, M.; Cai, W.; Ju, S.-Y.; Edgeworth, J.; Li, X.; Magnuson, C. W.; Velamakanni, A.; Piner, R. D.; Kang, J.; Park, J.; Ruoff, R. S., Oxidation Resistance of Graphene-Coated Cu and Cu/Ni Alloy. *Acs Nano*, null-null.
31. Xie, J. Y.; Ahmad, M. N.; Bai, H. D.; Li, H. Y.; Yang, W. T., Concentration and temperature controlled oxidation and cutting of single-walled carbon nanotubes by ammonium persulfate. *Science China-Chemistry* **2010,** *53* (9), 2026-2032.
32. Ziegler, K. J.; Gu, Z. N.; Shaver, J.; Chen, Z. Y.; Flor, E. L.; Schmidt, D. J.; Chan, C.; Hauge, R. H.; Smalley, R. E., Cutting single-walled carbon nanotubes. *Nanotechnology* **2005,** *16* (7), S539-S544.
33. Li, X. S.; Magnuson, C. W.; Venugopal, A.; An, J. H.; Suk, J. W.; Han, B. Y.; Borysiak, M.; Cai, W. W.; Velamakanni, A.; Zhu, Y. W.; Fu, L. F.; Vogel, E. M.; Voelkl,

E.; Colombo, L.; Ruoff, R. S., Graphene Films with Large Domain Size by a Two-Step Chemical Vapor Deposition Process. *Nano Letters* **2010,** *10* (11), 4328-4334.
34. Young, F. W., Etch Pits at Dislocations in Copper. *Journal of Applied Physics* **1961,** *32* (2), 192-&.
35. Lovell, L. C.; Wernick, J. H., Dislocation Etch Pits and Polygonization in High-Purity Copper. *Journal of Applied Physics* **1959,** *30* (4), 590-592.
36. Ruff, A. W., Dislocations and Chemical Etch Pits in Copper. *Journal of Applied Physics* **1962,** *33* (12), 3392-&.
37. Tracz, A.; Wegner, G.; Rabe, J. P., Scanning tunneling microscopy study of graphite oxidation in ozone-air mixtures. *Langmuir* **2003,** *19* (17), 6807-6812.
38. Alzina, F.; Tao, H.; Moser, J.; Garcia, Y.; Bachtold, A.; Sotomayor-Torres, C. M., Probing the electron-phonon coupling in ozone-doped graphene by Raman spectroscopy. *Physical Review B* **2010,** *82* (7), -.
39. Cancado, L. G.; Jorio, A.; Ferreira, E. H. M.; Stavale, F.; Achete, C. A.; Capaz, R. B.; Moutinho, M. V. O.; Lombardo, A.; Kulmala, T. S.; Ferrari, A. C., Quantifying Defects in Graphene via Raman Spectroscopy at Different Excitation Energies. *Nano Letters*, null-null.
40. Lin, Y.-C.; Jin, C.; Lee, J.-C.; Jen, S.-F.; Suenaga, K.; Chiu, P.-W., Clean Transfer of Graphene for Isolation and Suspension. *Acs Nano*, null-null.
41. Shi, Y. M.; Hamsen, C.; Jia, X. T.; Kim, K. K.; Reina, A.; Hofmann, M.; Hsu, A. L.; Zhang, K.; Li, H. N.; Juang, Z. Y.; Dresselhaus, M. S.; Li, L. J.; Kong, J., Synthesis of Few-Layer Hexagonal Boron Nitride Thin Film by Chemical Vapor Deposition. *Nano Letters* **2010,** *10* (10), 4134-4139.
42. Ci, L.; Song, L.; Jin, C. H.; Jariwala, D.; Wu, D. X.; Li, Y. J.; Srivastava, A.; Wang, Z. F.; Storr, K.; Balicas, L.; Liu, F.; Ajayan, P. M., Atomic layers of hybridized boron nitride and graphene domains. *Nature Materials* **2010,** *9* (5), 430-435.
43. Li, X. S.; Cai, W. W.; Colombo, L.; Ruoff, R. S., Evolution of Graphene Growth on Ni and Cu by Carbon Isotope Labeling. *Nano Letters* **2009,** *9* (12), 4268-4272.
44. Huang, P. Y.; Ruiz-Vargas, C. S.; van der Zande, A. M.; Whitney, W. S.; Levendorf, M. P.; Kevek, J. W.; Garg, S.; Alden, J. S.; Hustedt, C. J.; Zhu, Y.; Park, J.; McEuen, P. L.; Muller, D. A., Grains and grain boundaries in single-layer graphene atomic patchwork quilts. *Nature* **2011,** *469* (7330), 389-92.
45. Regan, W.; Alem, N.; Aleman, B.; Geng, B. S.; Girit, C.; Maserati, L.; Wang, F.; Crommie, M.; Zettl, A., A direct transfer of layer-area graphene. *Applied Physics Letters* **2010,** *96* (11).
46. Dai, H. J.; Wang, X. R.; Tabakman, S. M., Atomic layer deposition of metal oxides on pristine and functionalized graphene. *Journal of the American Chemical Society* **2008,** *130* (26), 8152-+.
47. Kuiken, H. K., A mathematical model for wet-chemical diffusion-controlled mask etching through a circular hole. *Journal of Engineering Mathematics* **2003,** *45* (1), 75-90.
48. Du, X.; Skachko, I.; Barker, A.; Andrei, E. Y., Approaching ballistic transport in suspended graphene. *Nature Nanotechnology* **2008,** *3* (8), 491-495.
49. Suk, M. E.; Aluru, N. R., Water Transport through Ultrathin Graphene. *Journal of Physical Chemistry Letters* **2010,** *1* (10), 1590-1594.

50. Wofford, J. M.; Nie, S.; McCarty, K. F.; Bartelt, N. C.; Dubon, O. D., Graphene Islands on Cu Foils: The Interplay between Shape, Orientation, and Defects. *Nano Letters* **2010,** *10* (12), 4890-4896.
51. Lee, C.; Wei, X. D.; Li, Q. Y.; Carpick, R.; Kysar, J. W.; Hone, J., Elastic and frictional properties of graphene. *Physica Status Solidi B-Basic Solid State Physics* **2009,** *246* (11-12), 2562-2567.
52. Moors, M.; Amara, H.; de Bocarme, T. V.; Bichara, C.; Ducastelle, F.; Kruse, N.; Charlier, J. C., Early Stages in the Nucleation Process of Carbon Nanotubes. *Acs Nano* **2009,** *3* (3), 511-516.
53. Hofmann, S.; Sharma, R.; Ducati, C.; Du, G.; Mattevi, C.; Cepek, C.; Cantoro, M.; Pisana, S.; Parvez, A.; Cervantes-Sodi, F.; Ferrari, A. C.; Dunin-Borkowski, R.; Lizzit, S.; Petaccia, L.; Goldoni, A.; Robertson, J., In situ observations of catalyst dynamics during surface-bound carbon nanotube nucleation. *Nano Letters* **2007,** *7* (3), 602-608.
54. Vlassiouk, I.; Regmi, M.; Fulvio, P.; Dai, S.; Datskos, P.; Eres, G.; Smirnov, S., Role of Hydrogen in Chemical Vapor Deposition Growth of Large Single-Crystal Graphene. *Acs Nano 5* (7), 6069-6076.
55. Militzer, M.; Hofmann, S., Kinetics of Sulfur and Phosphorus Surface Segregation Competition in Copper. *Scripta Metallurgica Et Materialia* **1994,** *31* (11), 1501-1506.
56. Han, G. H.; Gunes, F.; Bae, J. J.; Kim, E. S.; Chae, S. J.; Shin, H. J.; Choi, J. Y.; Pribat, D.; Lee, Y. H., Influence of Copper Morphology in Forming Nucleation Seeds for Graphene Growth. *Nano Lett* **2011**, null-null.
57. Colombo, L.; Li, X.; Han, B.; Magnuson, C.; Cai, W.; Zhu, Y.; Ruoff, R. S., Growth Kinetics and Defects of CVD Graphene on Cu. *ECS Transactions* **2010,** *28* (5), 109-114.
58. Norskov, J. K.; Bligaard, T.; Hvolbaek, B.; Abild-Pedersen, F.; Chorkendorff, I.; Christensen, C. H., The nature of the active site in heterogeneous metal catalysis. *Chemical Society Reviews* **2008,** *37* (10), 2163-2171.
59. Coraux, J.; N'Diaye, A. T.; Engler, M.; Busse, C.; Wall, D.; Buckanie, N.; Heringdorf, F. J. M. Z.; van Gastel, R.; Poelsema, B.; Michely, T., Growth of graphene on Ir(111) *New Journal of Physics* **2009,** *11*.
60. Wahl, E. H.; Owano, T. G.; Kruger, C. H.; Zalicki, P.; Ma, Y.; Zare, R. N., Measurement of absolute CH3 concentration in a hot-filament reactor using cavity ring-down spectroscopy. *Diamond and Related Materials* **1996,** *5* (3-5), 373-377.
61. Su, M.; Zheng, B.; Liu, J., A scalable CVD method for the synthesis of single-walled carbon nanotubes with high catalyst productivity. *Chemical Physics Letters* **2000,** *322* (5), 321-326.
62. Yan, K.; Peng, H.; Zhou, Y.; Li, H.; Liu, Z., Formation of bilayer bernal graphene: layer-by-layer epitaxy via chemical vapor deposition. *Nano Lett* **2011,** *11* (3), 1106-10.
63. Zhang, W. a. W., P. and Li, Z. and Yang, J.,, First-Principles Thermodynamics of Graphene Growth on Cu Surface. *ArXiv e-prints* **2011**, 1101.3851.
64. Watwe, R. M.; Bengaard, H. S.; Rostrup-Nielsen, J. R.; Dumesic, J. A.; Norskov, J. K., Theoretical studies of stability and reactivity of CHx species on Ni(111). *Journal of Catalysis* **2000,** *189* (1), 16-30.

65. An, W.; Zeng, X. C.; Turner, C. H., First-principles study of methane dehydrogenation on a bimetallic Cu/Ni(111) surface. *Journal of Chemical Physics* **2009,** *131* (17), -.
66. Ashfold, M. N. R.; May, P. W.; Petherbridge, J. R.; Rosser, K. N.; Smith, J. A.; Mankelevich, Y. A.; Suetin, N. V., Unravelling aspects of the gas phase chemistry involved in diamond chemical vapour deposition. *Physical Chemistry Chemical Physics* **2001,** *3* (17), 3471-3485.
67. Xu, Y. D.; Bao, X. H.; Lin, L. W., Direct conversion of methane under nonoxidative conditions. *Journal of Catalysis* **2003,** *216* (1-2), 386-395.
68. Zhong, G.; Hofmann, S.; Yan, F.; Telg, H.; Warner, J. H.; Eder, D.; Thomsen, C.; Milne, W. I.; Robertson, J., Acetylene: A Key Growth Precursor for Single-Walled Carbon Nanotube Forests. *Journal of Physical Chemistry C* **2009,** *113* (40), 17321-17325.
69. Vandenbrekel, C. H. J.; Bollen, L. J. M., Low-Pressure Deposition of Polycrystalline Silicon from Silane. *Journal of Crystal Growth* **1981,** *54* (2), 310-322.
70. Becker, A.; Huttinger, K. J., Chemistry and kinetics of chemical vapor deposition of pyrocarbon - IV - Pyrocarbon deposition from methane in the low temperature regime. *Carbon* **1998,** *36* (3), 213-224.
71. Zhou, D. H.; Ma, D.; Wang, Y.; Liu, X. C.; Bao, X. H., Study with density functional theory method C-H bond activation on the MoO2/HZSM-5 on methane active center. *Chemical Physics Letters* **2003,** *373* (1-2), 46-51.
72. Wu, P.; Zhang, W. H.; Li, Z. Y.; Yang, J. L.; Hou, J. G., Communication: Coalescence of carbon atoms on Cu (111) surface: Emergence of a stable bridging-metal structure motif. *Journal of Chemical Physics* **2010,** *133* (7), -.
73. Kim, M. H.; Lee, E. K.; Jun, J. H.; Kong, S. J.; Han, G. Y.; Lee, B. K.; Lee, T. J.; Yoon, K. J., Hydrogen production by catalytic decomposition of methane over activated carbons: kinetic study. *International Journal of Hydrogen Energy* **2004,** *29* (2), 187-193.
74. Avouris, P.; Chen, Z. H.; Perebeinos, V., Carbon-based electronics. *Nature Nanotechnology* **2007,** *2* (10), 605-615.
75. Bae, S.; Kim, H.; Lee, Y.; Xu, X. F.; Park, J. S.; Zheng, Y.; Balakrishnan, J.; Lei, T.; Kim, H. R.; Song, Y. I.; Kim, Y. J.; Kim, K. S.; Ozyilmaz, B.; Ahn, J. H.; Hong, B. H.; Iijima, S., Roll-to-roll production of 30-inch graphene films for transparent electrodes. *Nature Nanotechnology* **2010,** *5* (8), 574-578.
76. Hong, A. J.; Song, E. B.; Yu, H. S.; Allen, M. J.; Kim, J.; Fowler, J. D.; Wassei, J. K.; Park, Y.; Wang, Y.; Zou, J.; Kaner, R. B.; Weiller, B. H.; Wang, K. L., Graphene Flash Memory. *Acs Nano* **2011**, null-null.
77. Kim, R.-H.; Bae, M.-H.; Kim, D. G.; Cheng, H.; Kim, B. H.; Kim, D.-H.; Li, M.; Wu, J.; Du, F.; Kim, H.-S.; Kim, S.; Estrada, D.; Hong, S. W.; Huang, Y.; Pop, E.; Rogers, J. A., Stretchable, Transparent Graphene Interconnects for Arrays of Microscale Inorganic Light Emitting Diodes on Rubber Substrates. *Nano Letters* **2011**, null-null.
78. Wang, Z.-g.; Chen, Y.-f.; Li, P.-j.; Hao, X.; Liu, J.-b.; Huang, R.; Li, Y.-r., Flexible Graphene-Based Electroluminescent Devices. *Acs Nano* **2011**, null-null.
79. Zhou, Y.; Loh, K. P., Making Patterns on Graphene. *Advanced Materials* **2010,** *22* (32), 3615-3620.
80. Chen, Y. S.; Liang, J. J.; Xu, Y. F.; Liu, Z. B.; Zhang, L.; Zhao, X.; Zhang, X. L.; Tian, J. G.; Huang, Y.; Ma, Y. F.; Li, F. F., Toward All-Carbon Electronics: Fabrication

of Graphene-Based Flexible Electronic Circuits and Memory Cards Using Maskless Laser Direct Writing. *Acs Appl Mater Inter* **2010,** *2* (11), 3310-3317.
81. Marcus, C. M.; Lemme, M. C.; Bell, D. C.; Williams, J. R.; Stern, L. A.; Baugher, B. W. H.; Jarillo-Herrero, P., Etching of Graphene Devices with a Helium Ion Beam. *Acs Nano* **2009,** *3* (9), 2674-2676.
82. Chou, S. Y.; Liang, X.; Fu, Z., Graphene transistors fabricated via transfer-printing in device active-areas on large wafer. *Nano Letters* **2007,** *7* (12), 3840-3844.
83. Huang, Y.; Bai, J. W., Fabrication and electrical properties of graphene nanoribbons. *Materials Science & Engineering R-Reports* **2010,** *70* (3-6), 341-353.
84. Hsu, A.; Wang, H.; Kim, K. K.; Kong, J.; Palacios, T., Impact of Graphene Interface Quality on Contact Resistance and RF Device Performance. *Ieee Electron Device Letters* **2011,** *32* (8), 1008-1010.
85. Park, J.; Levendorf, M. P.; Ruiz-Vargas, C. S.; Garg, S., Transfer-Free Batch Fabrication of Single Layer Graphene Transistors. *Nano Letters* **2009,** *9* (12), 4479-4483.
86. Wang, Y. J.; Miao, C. Q.; Huang, B. C.; Zhu, J.; Liu, W.; Park, Y.; Xie, Y. H.; Woo, J. C. S., Scalable Synthesis of Graphene on Patterned Ni and Transfer. *Ieee Transactions on Electron Devices* **2010,** *57* (12), 3472-3476.
87. Hu, B.; Ago, H.; Ito, Y.; Kawahara, K.; Tsuji, M.; Magome, E.; Sumitani, K.; Mizuta, N.; Ikeda, K.-i.; Mizuno, S., Epitaxial growth of large-area single-layer graphene over Cu(1 1 1)/sapphire by atmospheric pressure CVD. *Carbon* **2011,** *In Press, Corrected Proof.*
88. Pflitsch, C.; Muhsin, A.; Bergmann, U.; Atakan, B., Growth of thin aluminium oxide films on stainless steel by MOCVD at ambient pressure and by using a hot-wall CVD-setup. *Surface & Coatings Technology* **2006,** *201* (1-2), 73-81.
89. Huang, B.; Xu, Q.; Wei, S.-H., Theoretical study of corundum as an ideal gate dielectric material for graphene transistors. *Physical Review B* **2011,** *84* (15), 155406.
90. Lakshminarasappa, B. N.; Nagabhushana, K. R.; Rao, K. N.; Singh, F.; Sulania, I., AFM and photoluminescence studies of swift heavy ion induced nanostructured aluminum oxide thin films. *Nuclear Instruments & Methods in Physics Research Section B-Beam Interactions with Materials and Atoms* **2008,** *266* (7), 1049-1054.
91. Sirringhaus, H.; Kawase, T.; Friend, R. H.; Shimoda, T.; Inbasekaran, M.; Wu, W.; Woo, E. P., High-resolution inkjet printing of all-polymer transistor circuits. *Science* **2000,** *290* (5499), 2123-2126.
92. Palacios, T.; Hsu, A.; Wang, H., Applications of Graphene Devices in RF Communications. *Ieee Communications Magazine* **2010,** *48* (6), 122-128.
93. Avouris, P., Graphene: Electronic and Photonic Properties and Devices. *Nano Letters* **2010,** *10* (11), 4285-4294.
94. Ryu, S.; Maultzsch, J.; Han, M. Y.; Kim, P.; Brus, L. E., Raman Spectroscopy of Lithographically Patterned Graphene Nanoribbons. *Acs Nano* **2011,** *5* (5), 4123-4130.
95. Kumar, A.; Whitesides, G. M., Features of Gold Having Micrometer to Centimeter Dimensions Can Be Formed through a Combination of Stamping with an Elastomeric Stamp and an Alkanethiol Ink Followed by Chemical Etching. *Appl Phys Lett* **1993,** *63* (14), 2002-2004.
96. Huang, Y. G.; Jung, I. W.; Xiao, J. L.; Malyarchuk, V.; Lu, C. F.; Li, M.; Liu, Z. J.; Yoon, J.; Rogers, J. A., Dynamically tunable hemispherical electronic eye camera

system with adjustable zoom capability. *Proceedings of the National Academy of Sciences of the United States of America* **2011,** *108* (5), 1788-1793.
97. Rogers, J. A.; Kim, D. H.; Lu, N. S.; Ma, R.; Kim, Y. S.; Kim, R. H.; Wang, S. D.; Wu, J.; Won, S. M.; Tao, H.; Islam, A.; Yu, K. J.; Kim, T. I.; Chowdhury, R.; Ying, M.; Xu, L. Z.; Li, M.; Chung, H. J.; Keum, H.; McCormick, M.; Liu, P.; Zhang, Y. W.; Omenetto, F. G.; Huang, Y. G.; Coleman, T., Epidermal Electronics. *Science* **2011,** *333* (6044), 838-843.